
Spatially resolved electronic and optoelectronic measurements of pentacene thin film transistors

Matthias Fiebig



München 2010

Spatially resolved electronic and optoelectronic measurements of pentacene thin film transistors

Matthias Fiebig

Dissertation
an der Fakultät für Physik
der Ludwig-Maximilians-Universität
München

vorgelegt von
Matthias Fiebig
aus München

München, den 07.09.2010

Erstgutachter: PD Dr. B. Nickel

Zweitgutachter: Prof. Dr. J. P. Kotthaus

Tag der mündlichen Prüfung: 18.10.2010

Contents

Zusammenfassung	xiii
Abstract	xv
1 Introduction	1
2 Basics of field effect devices	5
2.1 Metal-semiconductor-junction	5
2.1.1 Formation of an ideal MS-junction	5
2.1.2 Depletion layer	7
2.1.3 Formation of a surface charge dominated junction	8
2.2 Metal-insulator-semiconductor-junction	11
2.2.1 Formation of MIS-junction	11
2.2.2 Ideal MIS-junction	11
2.2.3 Surface space-charge region	13
2.3 Thin film transistor	16
2.3.1 Principle of a TFT	16
2.3.2 Current-voltage characteristic	19
2.3.3 Characteristic transport parameters	22
3 Organic semiconductors	27
3.1 Overview of organic semiconductors	27
3.2 Molecular orbitals	29
3.2.1 Conjugated electron system	29
3.2.2 Excitation states	30
3.3 Organic crystals	32
3.3.1 Excitons	32
3.3.2 Charge transport	35
3.4 Structure of pentacene	39
4 Fabrication of pentacene TFTs	43
4.1 Dielectric	43
4.1.1 Silicon oxide	43

4.1.2	Polymer buffer layer	45
4.2	Contacts	46
4.3	Pentacene deposition	47
5	Electronic properties of pentacene TFTs	51
5.1	Experimental setup	51
5.2	Basic transport characteristics	52
5.2.1	Conductance measurements	52
5.2.2	Transconductance measurements	53
5.3	Deviations from ideal behavior	56
5.3.1	Hysteresis	56
5.3.2	Threshold voltage shift	58
5.3.3	Nonohmic contact	59
5.4	Simulation of basic electronic circuits	61
6	Electronic thickness dependent in-situ measurements	65
6.1	Principle idea of in-situ measurement	65
6.2	Experimental implementation	66
6.2.1	Measurement setup of in-situ measurements	66
6.2.2	Sample preparation for in-situ measurements	70
6.2.3	Mounting of the sample	71
6.2.4	Measurement procedure	72
6.3	Experimental results	72
6.3.1	Thickness dependent conductance and transconductance	72
6.3.2	Thickness-dependent transport characteristics	74
6.4	Discussion	78
7	Spatially resolved optoelectronic measurements	83
7.1	Principle of laser scanning microscope	83
7.2	Measurement setup	85
7.3	Absorption measurements	91
7.3.1	Absorption spectrum	91
7.3.2	Spatially resolved absorption - Davydov splitting	92
7.4	Photoluminescence and Raman	93
7.4.1	Spatial distribution and yield of photoluminescence	93
7.4.2	Discussion of low photoluminescence signal - Exciton dynamics	97
7.4.3	Photoluminescence spectrum and Raman	99
7.5	Optoelectronic properties of pentacene transistors	101
7.5.1	Electrical response to global illumination	101
7.5.2	Experimental results of spatially resolved photoresponse measurements	104
7.5.3	Discussion of spatially resolved photoresponse measurements	111
8	Conclusion	125

Contents	vii
Acknowledgment	128
Bibliography	131
List of Publications	139
Danksagung	140

List of Figures

1.1	Mobility evolution of organic thin film transistors	2
2.1	Formation of an ideal MS-junction	6
2.2	Energy-diagram of an MS-junction under bias	7
2.3	Depletion width and maximum electric field at MS-junction	9
2.4	Formation of a surface charge dominated MS-junction.	10
2.5	Sketch of a MIS-device	11
2.6	Energy-band diagram of a MIS-junction	12
2.7	Energy-band diagram of an ideal MIS-junction	12
2.8	Energy-band diagram of a MIS-structure at the semiconductor surface	13
2.9	Debye length in dependence on the bulk carrier concentration	15
2.10	Space charge density in the semiconductor	16
2.11	Sketch of TFT designs	17
2.12	Spatially dependence of band bending in a TFT	18
2.13	Conductance of a TFT	22
2.14	Determination of characteristic transport parameters in a TFT	23
3.1	Structures of selected semiconductors	28
3.2	Chemical structures of polyacenes	30
3.3	Excitations scheme of an organic molecule	31
3.4	Davydov splitting in an anthracene crystal	34
3.5	Energy-diagram of polaron states	37
3.6	Temperature dependence of the mobility	39
3.7	AFM micrographs of a pentacene thin film	40
3.8	Herringbone structure of pentacene	41
4.1	Design of the bottom-contact thin film transistors	44
4.2	Chemical structure of cyclic olefin copolymer and polystyrene	45
4.3	UHV pentacene evaporation chamber.	47
4.4	Screenshot of Labview program for pentacene evaporation	48
5.1	Setup for the electronic measurements	52
5.2	Conductance curves of a pentacene TFT	53
5.3	Transconductance curves of a pentacene TFT.	54

5.4	Subthreshold slope of a pentacene TFT	55
5.5	Hysteresis of a pentacene TFT	57
5.6	Threshold shift of a pentacene TFT	59
5.7	Contact resistance of a pentacene TFT	60
5.8	Measured and simulated conductance curves of a pentacene TFT	62
5.9	Simulation of the voltage transfer characteristic of organic inverter circuit	63
5.10	Simulation of three-stage ring oscillator	64
6.1	Concept of electronic in-situ measurements of pentacene TFTs	66
6.2	Photograph of evaporation chamber	67
6.3	Schematic overview of the in-situ measurement chamber	68
6.4	Photograph of the sample stage	69
6.5	Photograph of the sample holder	70
6.6	Design of the samples for in-situ measurements	71
6.7	Scheme of the in-situ measurements	73
6.8	Conductance curves for selected pentacene thicknesses	74
6.9	Transconductance curves for selected pentacene thicknesses	75
6.10	Thickness dependence of transport characteristics with polystyrene coating	76
6.11	AFM micrograph of pentacene film at percolation threshold thickness	77
6.12	Thickness dependence of transport characteristics with topas coating	78
6.13	Model of surface trap states	81
7.1	Principle of the laser scanning microscope.	84
7.2	Photographs of the optical setup	85
7.3	Optical measurement setup	86
7.4	Circuitry of the optoelectrical setup.	88
7.5	Calibration of the laser scanning microscope.	90
7.6	Principle of the brightfield microscope.	91
7.7	Absorption spectrum of a pentacene thin film	92
7.8	Reflection maps of a pentacene thin film	94
7.9	Spatial extension of photoluminescence.	96
7.10	Photoluminescence dependence on light intensity.	97
7.11	Transient pump and probe measurements	98
7.12	Spectral response of a photoexcited pentacene film.	100
7.13	Transconductance curves in dark and with global illumination.	102
7.14	Time dependence of source-drain current under global illumination.	103
7.15	Reflection and photoresponse maps of a broad part of the pentacene transistor channel.	105
7.16	Photoresponse maps of a pentacene TFT in the linear and the saturation regime.	106
7.17	Photoresponse of a pentacene TFT in dependence on the position of illumination and on the gate voltage.	108
7.18	Photoresponse of a pentacene TFT for different chopper frequencies.	110

7.19 Schematic survey of the photoresponse.	112
7.20 Gate voltage dependence of slow photoresponse component.	114
7.21 Schematic of hole trap filling.	114
7.22 Schematic of the mechanism of the slow photoresponse component.	115
7.23 Spatial dependence of the photoresponse for various source-drain voltages.	117
7.24 Photoresponse maps for different polarizations of the incident light.	118
7.25 Potential profiles measured by Kelvin probe force microscopy.	120
7.26 Comparison of the width of the laser spot with the photoresponse.	122

Zusammenfassung

Organische Halbleiter gewinnen zur Zeit als elektronische und optoelektronische Bauelemente zunehmend an Bedeutung. Während organische Leuchtdioden, die oft auf Polymeren basieren, bereits Marktreife erreicht haben, sind organische Transistoren noch im Forschungsstatus. Für organische Transistoren verwendet man üblicherweise geordnete dünne Schichtstrukturen aus kleinen organischen Molekülen wie Pentacen, da hier im Vergleich zu den ungeordneten Polymeren höhere Ladungsträgerbeweglichkeiten erzielt werden können. Trotz intensiver Forschung sind die elektronischen Transportmechanismen und optischen Eigenschaften in solchen Systemen nicht völlig verstanden.

Der Ansatz der vorliegenden Arbeit besteht darin, die elektronischen und optoelektronischen Eigenschaften von Pentacen-Dünnschichttransistoren ortsaufgelöst zu untersuchen. Die dadurch erhaltenen Messdaten ermöglichen es, verschiedene Einflüsse auf das Transportverhalten in Pentacen aufzuschlüsseln und den verschiedenen Bereichen innerhalb des Transistors zuzuordnen.

Es wurden zwei verschiedene Versuchsaufbauten realisiert. Um Abhängigkeiten des Transports von der Pentacenschichtdicke zu untersuchen, wurden elektronische in-situ Messungen während des Aufdampfprozesses durchgeführt. Laterale Ortsauflösung wurde hingegen durch einen optischen Aufbau, mit dem kleine Bereiche des Transistorkanals beleuchtet wurden, umgesetzt.

Bei den elektronischen in-situ Messungen wurden kontinuierlich während des Aufdampfens von Pentacen die charakteristischen Kenngrößen der Transistoren bestimmt. Neben der Lochbeweglichkeit untersuchten wir im Speziellen die Verschiebung der Schwellwertspannung und die Hysterese der Transistoren, da diese durch lokale Fallenzustände ausgelösten Phänomene eine besonders wichtige Rolle bei den Transporteigenschaften organischer Halbleiter spielen. Das Verhalten der Hysterese konnte durch ein Modell, das lokale Fallenzustände an der Oberfläche der Pentacenschicht berücksichtigt, erklärt werden. Die Entwicklung der Schwellwertspannung sowie der Hysterese während des Aufdampfens erlaubten es desweiteren, die Debye-Länge in Pentacen zu bestimmen.

Der zweite Aufbau ermöglichte es, einerseits optische Eigenschaften wie Photolumineszenz und Reflektionsvermögen und andererseits optoelektronische Eigenschaften, insbesondere die Photoantwort, d.h. die lichtinduzierte Veränderung des Transistorstromes, in Abhängigkeit des Ortes der Beleuchtung zu untersuchen. Mit Hilfe der Reflektionsmessungen gelang es, unterschiedliche Absorption einzelner Pentacenkörner aufzulösen. Dies konnte auf eine Davydov-Aufspaltung zurückgeführt werden.

Die Photoantwort unserer Transistoren besteht aus einer langsamen Komponente, die unabhängig vom Beleuchtungsort auftrat, sowie einer schnellen Komponenten, die nur durch Einstrahlung an den Kontakten ausgelöst wurde. Aufgrund der Zeitskala und der Gatespannungsabhängigkeit wurde die langsame Komponente als bolometrischer Effekt interpretiert. Wärme, die durch Absorption in der Probe erzeugt und in den Halbleiterfilm transportiert wird, befreit Löcher aus Fallenzuständen, wodurch die Konzentration der freien Ladungsträger und damit der Gesamtstrom im Transistor erhöht wird. Die schnelle Photostromkomponente wird durch einen elektronischen Prozess, der auf einer Exzitonen-trennung durch das hohe elektrische Feld am Kontakt beruht, erklärt. Die große Ausdehnung des Signals wurde auf eine hohe Interkombinationsrate von Singulett-Exzitonen zu Triplett-Exzitonen, die aufgrund ihrer langen Lebensdauer große Diffusionslängen besitzen, zurückgeführt. Diese hohe Interkombinationsrate wurde durch die sehr schwache Photolumineszenzausbeute bestätigt.

Abstract

Organic semiconductors become increasingly significant as electronic and optoelectronic devices. In contrast to polymer based organic light emitting diodes, organic transistors have not gained marketability. For organic transistors, ordered thin film structures consisting of small organic molecules such as pentacene are usually used, since they exhibit higher charge carrier mobilities than disordered polymers. The electronic transport mechanisms and optical properties of these materials are not fully understood, although they are studied intensively.

This thesis approached to investigate the electronic and optoelectronic properties of pentacene thin film transistors spatially resolved. The obtained results enabled the disentanglement of varying influences on the transport behavior in pentacene and their allocation to different parts of the transistors.

Two different measurement setups were implemented. Electronic in-situ measurements were conducted to investigate the dependencies of the transport on the pentacene layer thickness during the evaporation. A lateral spatial resolution was obtained by an optical setup, which was designed to illuminate small areas of the transistor channel.

At the electronic in-situ measurements, the characteristic parameters of the transistors were recorded during the evaporation of pentacene. Besides the hole mobility, we investigated the threshold voltage shift and the hysteresis in particular. These phenomena, that are caused by trap states, play a crucial role for the transport properties of organic semiconductors. The behavior of the hysteresis could be explained by a model, that included trap states located on the surface of the pentacene layer. Furthermore, the evolution of the threshold voltage and the hysteresis during evaporation enabled the determination of the Debye length of pentacene.

The second setup was used to investigate both, the optical properties such as the photoluminescence or the reflection and the optoelectronic properties, in particular the photoresponse, i.e. the light induced change of the source-drain current, in dependence on the position of the illumination spot. Measuring the reflection, the different absorption of single pentacene grains could be resolved. This could be ascribed to Davydov-splitting. The photoresponse of our transistors consisted of a slow component, that existed throughout the whole device, as well as of a fast component, which was only triggered by an illumination at the contact edges. The slow component was interpreted to be a bolometric effect due to its time scale and gate voltage dependence. Heat that is produced in the sample by absorption and subsequently transferred into the pentacene layer, releases holes from

trap states. Therefore, the free charge carrier density and thus the source-drain current is increased. The fast photoresponse component is explained by an electronic process, which is due to the high electric field at the contact edges. The large extension of the signal was interpreted to arise from a high intersystem crossing rate from singlet excitons to triplet excitons, which possess a large diffusion length due to their long lifetime. This high intersystem crossing rate is confirmed by the very low photoluminescence yield.

Chapter 1

Introduction

The first publications that mention semiconducting properties of organic materials date back to 1948, when Elay reported on semiconducting behavior of phthalocyanines [1]. Shortly afterwards in 1950, Akamuta et. al. presented electrical conductivity of various organic compounds [2]. In the middle of the 1950s, lots of organic semiconducting molecules were known [3], but little was understood about the transport mechanisms in these new class of materials. The authors of these publications agreed upon that the π -electrons are essential for the observed transport properties, but an exact transport model could not be provided at this early stage. This rapidly changed in the early 1960s. At this time, the quality of organic single crystals increased significantly, allowing for more precise measurements. Particularly, the measurement of space charge limited currents supplied a detailed picture of the transport mechanism [4–6]. A sophisticated analysis allowed for a deeper insight into basic material properties, such as the distribution of the electronic states. Additional experiments investigating the photoconductivity also contributed to a thorough understanding of optical and electronic behavior. In 1963, Pope et. al. observed electroluminescence from an organic crystal for the first time [7], which was confirmed shortly later by Helfrich et. al. [8]. In this period, these experiments were only conducted to further understand fundamental physical processes, like the recombination mechanism of charge carriers, in these materials. Applications were not in the scope, since their inorganic counterparts showed superior transport properties. Therefore, research on organic semiconductors was decelerated for about two decades, before in a very short period of time, the first photovoltaic cell [9], the first organic light emitting diode (OLED) [10] and the first organic field effect transistor (OFET) [11] could be realized in the years of 1986 and 1987. These implementations triggered a dramatic increase in the effort on research in the field of organic semiconductor devices. How much the research has exploded in this field since then can be estimated, if one looks at the amount of publications that are delivered by the scientific search engine “ISI Web of Knowledge”. A simple quest on the topic “organic semiconductors” on September 6th 2010 provides an overwhelming 6708 publications, but only 232 were released before the year of 1987. In the case of OLEDs, this intensified efforts have already lead to the first applications on displays in the beginning of the 21st century. Unlike OLEDs, where research transformed more into development in the

recent years, processes of charge transport in organic field effect transistors (OFETs) are still not understood in detail, especially in less ordered thin films. Nevertheless, the first applications are soon to expect, as the mobility of some thin films with organic molecules, such as pentacene, have reached the value of amorphous silicon by the end of the 1990s (see Figure 1.1).

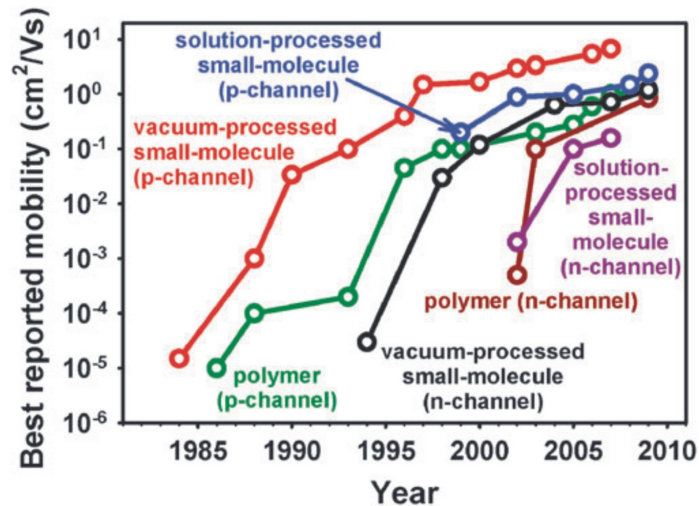


Figure 1.1: Semilogarithmic plot of the mobility evolution of thin film transistors. Adapted from [12].

In contrast to polymer based OLEDs, organic transistors usually contain small organic molecules, since they exhibit the highest charge carrier mobilities for organic thin films. This is due to their ordered structure, that can be achieved, if the film is grown under controlled conditions. Pentacene is a small molecule, that can form polycrystalline layers, if it is evaporated in vacuum using adjusted process parameters. Its thin films show one of the highest hole mobilities among all organic films, though their electron mobility is very low. Therefore, pentacene can be used as model molecule to fabricate unipolar field effect transistors.

Within the scope of this thesis, the electronic and optoelectronic properties of pentacene thin film transistors (TFTs) are investigated. Besides standard electronic characterization of the transistors, the dissertation approached the disentanglement of various influences on the transport properties in pentacene by using spatially resolved measurements. Therefore, we implemented two different measurement setups. First, an electronic in-situ measurement setup was developed in order to determine the transport parameters during the evaporation of pentacene. Second, a spatially resolved optical setup was realized, that allowed for the investigation of the transistor response upon local illumination. In the following, a short outline of this thesis is provided.

In chapter 2, the general electronic properties of thin film transistors are explained and

important equations for its characteristic transport parameters are derived. Since a TFT involves a metal-insulator-semiconductor junction and metal-semiconductor junctions, these interfaces are discussed with special emphasis on their spatial dimensions. The electronic and optical properties of organic semiconductors are introduced in chapter 3. The charge transport in organic semiconductor differs from their inorganic counterparts due to their molecular structure. It is described including the polaron model. In contrast to inorganic semiconductors, the optical properties of organic materials are not dominated by the interactions within the crystal structure but by the properties of the single organic molecule. Finally, the structure of the pentacene thin film is presented. Chapter 4 describes the fabrication of our pentacene TFTs. The electronic properties of these transistors are presented in Chapter 5. Especially the trap states, that cause hysteresis and threshold voltage shifts, are studied comprehensively. The main results of this dissertation are given in Chapter 6 and 7, where the spatially resolved measurements are presented and discussed. Chapter 6 first introduces the setup of the electronic in-situ measurements, that was intended to determine the transport parameters during pentacene evaporation with a thickness resolution as high as possible. Then, the evolution during deposition of the mobility, the threshold voltage and the hysteresis is presented. We modeled the evolution of the hysteresis by a trap model, which furthermore allowed a determination of the Debye length of pentacene. Chapter 7 presents the optoelectrical spatially resolved measurements. First, the optical setup with its homemade laser scanning microscope is described. Then, the spatially resolved reflection, photoluminescence and photoresponse measurements are presented and discussed. The main results of this PhD-thesis are summarized in Chapter 8 and some ideas for future experiments are finally provided.

Chapter 2

Basics of field effect devices

In this chapter, the basic transport properties of thin film transistors (TFTs) are explained. A TFT consists of a metal-insulator-semiconductor-junction (MIS-junction) in combination with metal-semiconductor-junctions (MS-junctions), therefore these interfaces will be discussed first. Special emphasis is given to the spatial dimensions of charge accumulation regions and potential distributions. This chapter is mainly based on the textbooks of S. M. Sze [13] and G. Hadziioannou and P. F. Hutton [14]. In this dissertation, only hole conducting behavior was observed experimentally, hence this chapter will focus on p-type semiconductors.

2.1 Metal-semiconductor-junction

Charge carriers in a TFT have to be injected from a metal electrode, which is called source, into the semiconductor, and extracted back from the semiconductor into a second metal contact, which is called drain. These metal-semiconductor-junctions play a crucial role in the electronic performance of a TFT and shall be considered in more detail first.

2.1.1 Formation of an ideal MS-junction

Once a metal and a semiconductor get into contact, a barrier for charge transfer across this interface is formed. The formation of an ideal MS-junction, which is assumed to be surface state free, will be explained in the following and is depicted in Figure 2.1.

As long as a metal and a semiconductor are not connected, the Fermi energies E_F of both materials are not aligned. In the metal, the Fermi level is equal to $q\phi_m$, where q is the elementary charge and ϕ_m the work function of the metal. In the semiconductor, E_F is situated between the conduction band energy E_L , which lies at $q\chi_S$ from the vacuum energy (ionization energy), and the valence band energy E_V . In the case of a p-type semiconductor, E_F of the semiconductor is closer to E_V than to E_L . If the two materials are connected, the different Fermi levels equalize under thermal equilibrium conditions. This equilibration occurs via charge transfer. If we consider the case that E_F of the metal is above E_F of

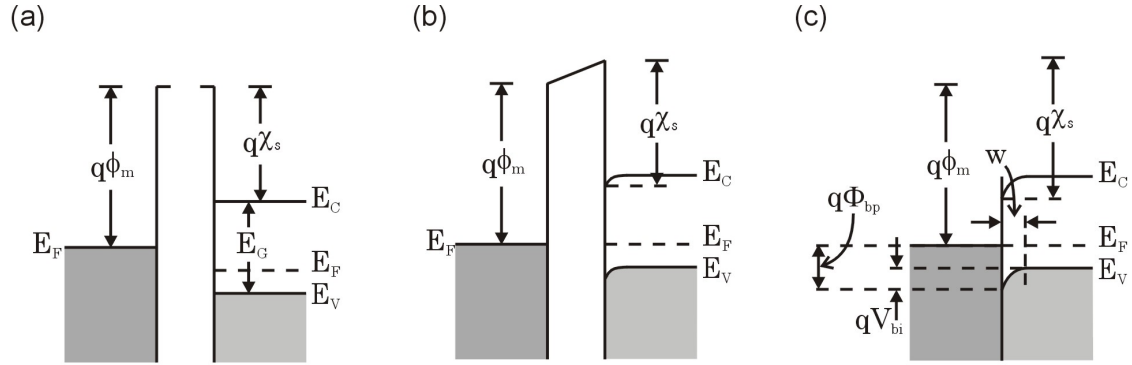


Figure 2.1: Formation of an ideal MS-junction. In (a) the two materials are not connected, in (b) metal and semiconductor are electrically connected but spatially separated while in (c) they are in full contact.

the semiconductor, electrons flow from the metal into the semiconductor. Due to the high carrier density, the charge at the metal is concentrated within the Thomas-Fermi length ($\approx 0.5 \text{ \AA}$). This is a subatomic distance, therefore the charge can be considered to be at the metal surface. However, as the carrier concentration is much lower in the semiconductor, the charge is extended much further there. The charge causes an electric field orientated perpendicular to the metal-semiconductor interface. This implies a downward band bending in the semiconductor adjacent to the metal. This region is called depletion layer with its characteristic thickness w . If the Schottky effect is neglected, the barrier height for holes $q\phi_{bp}$ at such a junction is given by

$$q\phi_{bp} = E_g - q(\phi_m - \chi_s). \quad (2.1)$$

It is important to notice that in the case of an ideal MS-junction the energy barrier is dependent on the work function of the metal. Thus, choosing an appropriate metal with a work function closely situated to the valence band of the p-type semiconductor can minimize the energy barrier at the junction. In Table 2.1 work functions of selected metals are listed. In some metals the exact work function depends on the orientation of the crystal surface. Please notice that these values are only valid for very clean surfaces. Little contaminations, e.g. arising from air exposure, can significantly change the work function.

metal	Ca	Al	Ti	Ag	Au	Pt
work function	2.87	4.06 – 4.26	4.33	4.52 – 4.74	5.1 – 5.47	5.12 – 5.93

Table 2.1: Work functions of selected metals in clean vacuum conditions. Values are taken from [15].

2.1.2 Depletion layer

In order to calculate the potential ψ of an MS-junction without an applied external bias one has to solve the Poisson equation

$$\frac{d^2\psi}{dx^2} = -\frac{\rho(x)}{\epsilon_s} \quad (2.2)$$

where ϵ_s is the dielectric permittivity of the semiconductor and $\rho(x)$ is the charge density in dependence of the distance x to the interface, which in the case of a p-type semiconductor is given by

$$\rho = q(p - n - N_a). \quad (2.3)$$

Here, N_a is the density of acceptor dopants, while p and n are the concentrations of holes and electrons, respectively. In order to calculate the potential $\psi(x)$, it is sufficient to use the Schottky approximation, i.e. the effective density of charge is assumed to be $-qN_a$ within the depletion region and zero outside of this region. Double integration of equation (2.2) then gives

$$\psi(x) = -\frac{qN_a}{2\epsilon_s}(w-x)^2 \quad (2.4)$$

where w is the width of the depletion layer (see also Figure 2.1). With V_{bi} being the built-in potential at the interface ($x = 0$), the depletion width is equal to

$$w = \sqrt{-\frac{2\epsilon_s V_{bi}}{qN_a}}. \quad (2.5)$$

So far, the MS-junction has been described without external bias. If one applies a voltage V across the MS-junction, the band bending is affected accordingly to Figure 2.2.

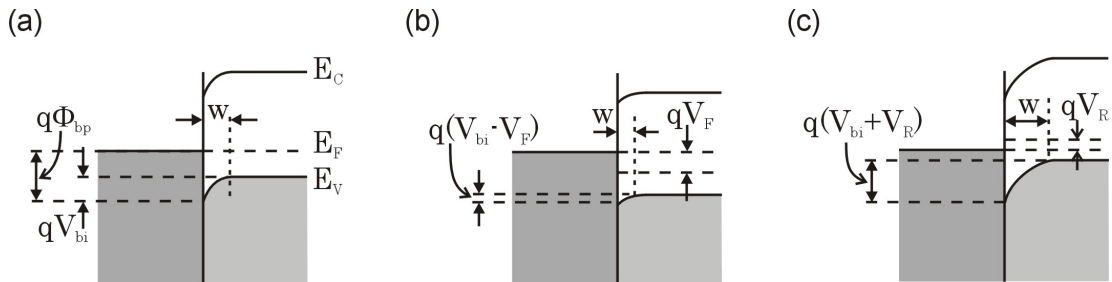


Figure 2.2: Energy-band diagram of an MS-junction with a p-type semiconductor. (a) No bias is applied, (b) a forward bias is applied and (c) a reverse bias is applied.

If one applies a negative voltage at the p-type semiconductor with respect to the metal, the band bending is lowered and the associated electric field across the junction is thus decreased. In this case, charge transport is facilitated. Therefore, this is called forward biasing. In contrast, if one applies a voltage with opposite sign, the band bending and the

electric field increase. Under these conditions charge transfer is blocked, the junction was thus reversely biased. It is possible to show that the current density j across the junction can be described to be

$$j = j_s \left[\exp\left(\frac{qV}{kT}\right) - 1 \right] \quad (2.6)$$

where j_s is the saturation current density under reverse bias.

Considering the depletion thickness, one also has to include the applied voltage V in equation (2.5) leading to

$$w = \sqrt{-\frac{2\epsilon_s (V_{bi} - V)}{qN_a}}. \quad (2.7)$$

Furthermore, one can obtain the electric field F for $x < w$ at an MS-junction by differentiating equation (2.4) with respect to the position x , resulting in

$$F(x) = -\frac{\partial\psi(x)}{\partial x} = \frac{qN_a}{\epsilon_s}(w - x). \quad (2.8)$$

The maximum electric field F_{max} is therefore situated at $x = 0$, given by

$$F_{max} = F(x = 0) = \sqrt{-\frac{2qN_a (V_{bi} - V)}{\epsilon_s}} = \frac{2(V_{bi} - V)}{w}. \quad (2.9)$$

Hence, both, the depletion width w as well as the maximum electric field F_{max} of an MS-junction increase proportionally with the square root of the bias $V_{bi} - V$, that falls across the junction. Unlike this, the dependencies on the carrier concentration and the relative permittivity are different for the depletion width and the maximum electric field. Here, $w \propto (\epsilon_s/N_a)^{1/2}$ while $F_{max} \propto (N_a/\epsilon_s)^{1/2}$. In Figure 2.3 the voltage dependence of the depletion width and of the electric field is depicted for different doping concentration and for two different permittivities, namely for $\epsilon_s = 11.9\epsilon_0$, and for $\epsilon_s = 3\epsilon_0$, which correspond to silicon and to a typical value of an organic semiconductor, respectively.

It is interesting, that for a low permittivity like $\epsilon_s = 3\epsilon_0$ the depletion width is in the range of 100 nm or even less, while the maximum electric field at the interface reaches extremely high values of $(10^5 - 10^6) V/cm$.

2.1.3 Formation of a surface charge dominated junction

So far, we have discussed an ideal MS-junction, which assumes that the density of states at the semiconductor surface is equal to its bulk density. However, in reality, semiconductors have additional localized states at the surface with energies within the bandgap. These states have different origins. First, they simple arise from the broken symmetry at the surface, which leads to a perturbation of the polarization energy, resulting in an energy shift. Second, the localized states are due to a high defect density at the surface, which is already caused by small contaminations.

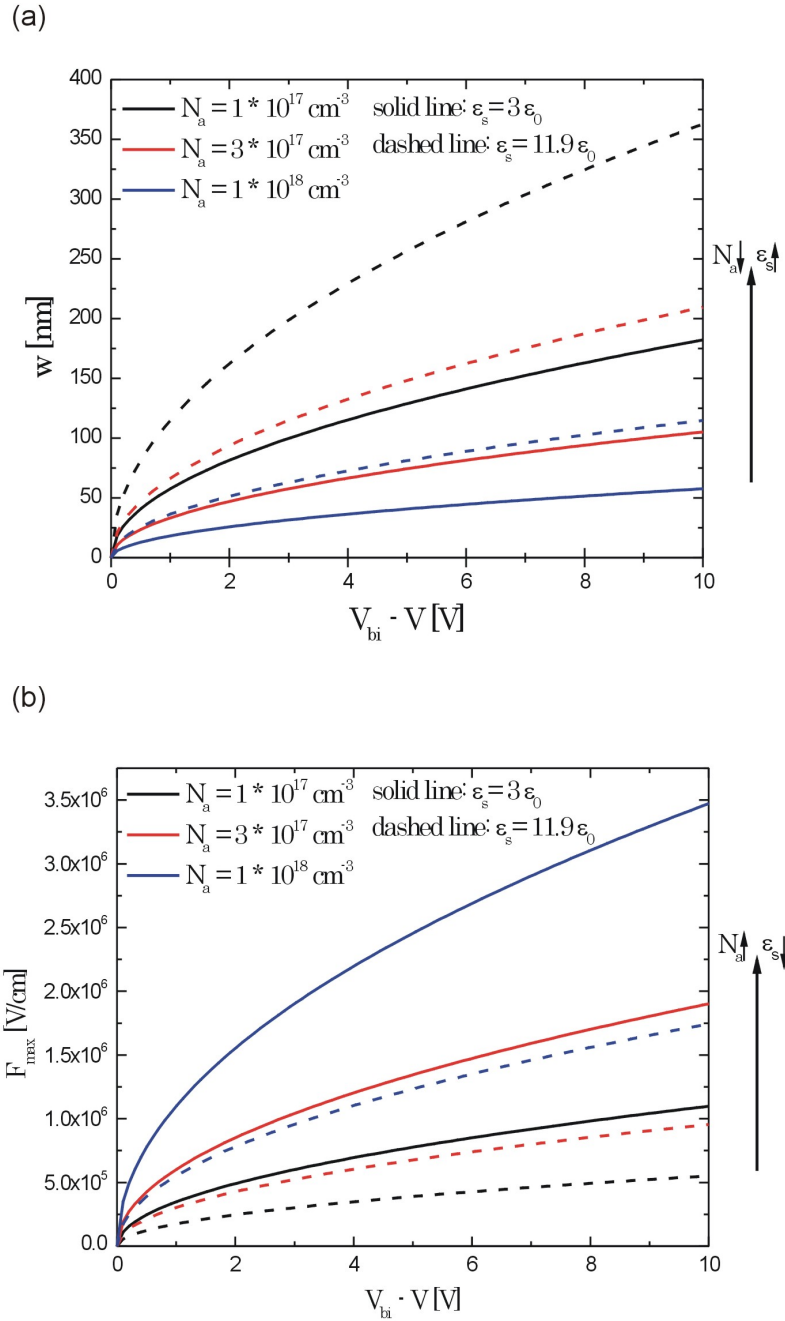


Figure 2.3: Depletion width (a) and maximum electric field (b) in dependence on the voltage for different doping concentration. Graphs are shown for silicon with $\epsilon_s = 11.9 \epsilon_0$ and for $\epsilon_s = 3 \epsilon_0$, which is a typical value for organic semiconductors.

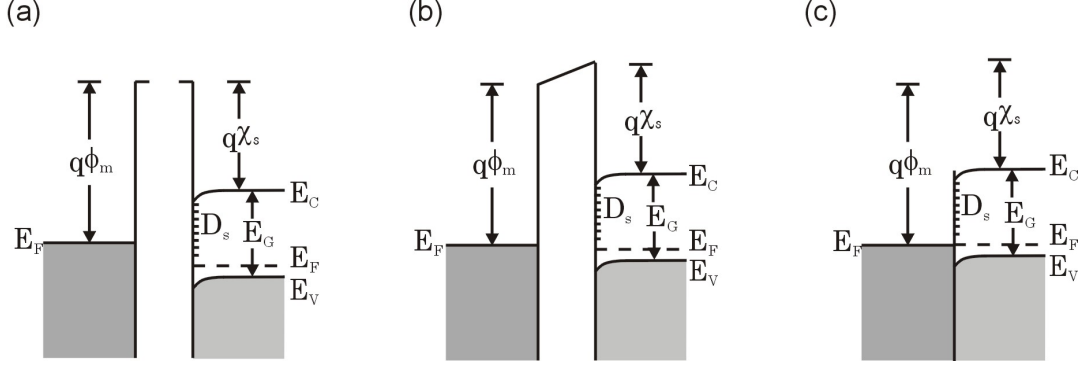


Figure 2.4: Formation of a surface charge dominated MS-junction. In (a) the two materials are not connected, but surface and bulk states are in equilibrium in the semiconductor. In (b) metal and semiconductor are electrically connected but spatially separated while in (c) they are in full contact. The charge flow due to the difference of the Fermi levels is completely accommodated by the surface states.

Unlike in Figure 2.1, let us now consider the formation of an MS-junction with a very high density of surface states D_s at the semiconductor surface. If the semiconductor is not connected with a metal, the surface states in the bandgap are filled with electrons up to the Fermi energy E_F . As we consider p-type semiconductors, one could also say, that above E_F the surface states are full of holes. In thermal equilibrium between surface states and bulk states, these filled hole states cause a downward band bending, as it is depicted in Figure 2.4 (a). When the semiconductor is connected with a metal, the Fermi levels of both materials will align and charge is flowing. If the surface charge density is large enough to accommodate all the additional surface charge without significantly altering the Fermi level, the space charge density will remain unaffected. Hence, the band bending and the barrier height ϕ_{bp} will also not change. Consequently, the barrier for holes of such an MS-junction is only determined by the surface states of the semiconductor and not by the work function difference between the metal and the semiconductor, as it is given by equation (2.1) in the case of an ideal MS-junction.

In reality, MS-junctions are often neither ideal nor independent of the work function difference, but a mixture of these two limiting cases. Hence, the hole barrier height can be written to be

$$\phi_{bp} = c_1\phi_m + c_2 \quad (2.10)$$

where c_1 and c_2 account for the work function difference dependent part of the barrier and the barrier pinning due to the surface states, respectively. For $D_s \rightarrow \infty$, $c_1 \rightarrow 0$, so that the barrier is only determined by the surface states, as depicted in Figure 2.4. For $D_s \rightarrow 0$, $c_1 \rightarrow 1$ and an ideal MS-junction is formed, as it is shown in Figure 2.1.

2.2 Metal-insulator-semiconductor-junction

2.2.1 Formation of MIS-junction

In a metal-insulator-semiconductor-junction (MIS-junction), the MS-junction is extended by an insulating layer, which is sandwiched between the metal and the semiconductor (see Figure 2.5). Therefore, direct charge transport from the metal into the semiconductor is prohibited. Nevertheless, it is still possible to accumulate charge via a field effect across the insulator by biasing the metal, which is explained in the following.

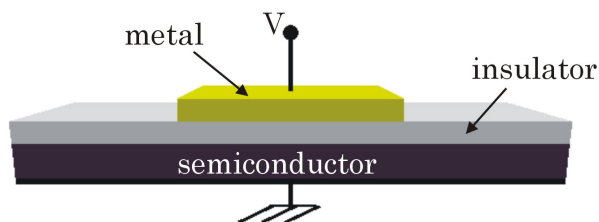


Figure 2.5: Sketch of a MIS-junction device.

2.2.2 Ideal MIS-junction

An ideal MIS-junction must meet the following three conditions:

1. the work functions of the metal and the semiconductor are equal
2. the only charges that exist are, under any bias situation, in the semiconductor and with an equal amount but different sign in the metal
3. charge transport through the insulator is prohibited, i.e. the resistivity of the insulator can be assumed to be infinity

The last condition can mostly be realized by choosing an insulator with a sufficient thickness. However, matching the first two conditions is very challenging, because fixed charges often exist on the insulator surface and the work functions of the materials are very sensitive to contamination or the orientation of the surfaces (see also Table 2.1). Nevertheless, if these three conditions are fulfilled, the energy-band diagram looks as it is depicted in Figure 2.6 (a). The work function difference ϕ_{ms} between the metal and the semiconductor can be described by

$$\phi_{ms} = \phi_m - \left(\chi + \frac{E_G}{2q} - \psi_B \right) \quad (2.11)$$

where ϕ_m is the work function of the metal, χ is the semiconductor electron affinity, E_G the bandgap of the semiconductor and ψ_B the difference between the Fermi level of the semiconductor E_F and the intrinsic Fermi level of the semiconductor E_i , which is defined

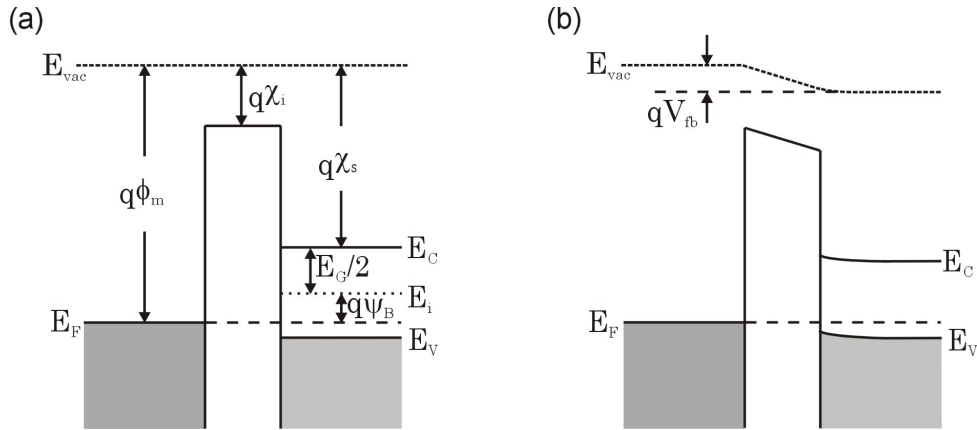


Figure 2.6: Energy-band diagram of a MIS-junction with a p-type semiconductor. (a) An ideal MIS-junction and (b) a real MIS-junction with a band curvature.

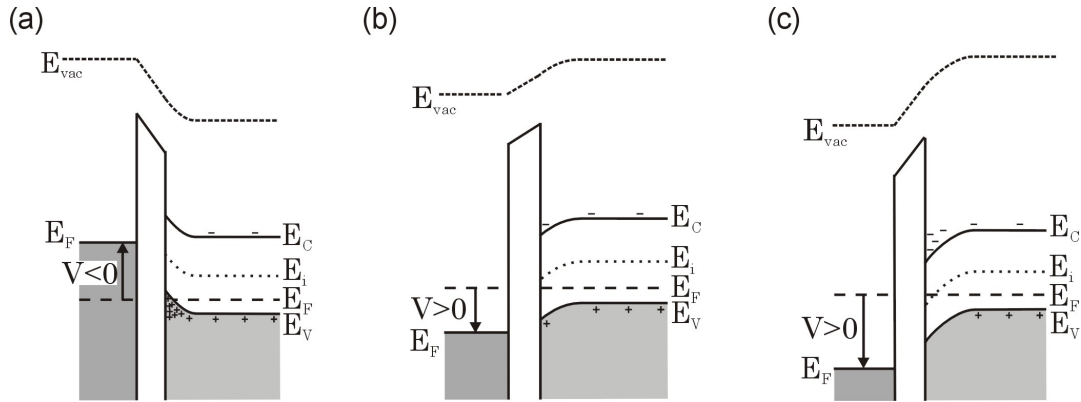


Figure 2.7: Energy-band diagram of an ideal MIS-junction with a p-type semiconductor for (a) accumulation, (b) depletion and (c) inversion.

to be exactly in the middle of the bandgap. If ϕ_{ms} is zero, an ideal MIS-junction is formed. However, if condition 1 or 2 is not fulfilled, this difference is not zero. Hence, the bands of the semiconductor will have a curvature even if no bias across the junction is applied (see Figure 2.6 (b)).

The band curvature that exist in most MIS-junctions in thermal equilibrium can be compensated by an appropriate voltage, the so-called flat-band voltage V_{fb} . Therefore it is sufficient to consider the ideal MIS-junction as a foundation to understand real devices.

When an ideal MIS-junction is biased, three different cases at the semiconductor-insulator interface can be distinguished if a p-type semiconductor is used, as it is shown in Figure 2.7.

First, applying a negative voltage at the electrode leads to an upward bending of the valence band. This reduces the distance of the valence band edge to the Fermi energy of the semiconductor at the interface. For large voltages the valence band edge can even cross the Fermi energy. Therefore, as the hole concentration is proportional to $\exp(E_V - E_F)$,

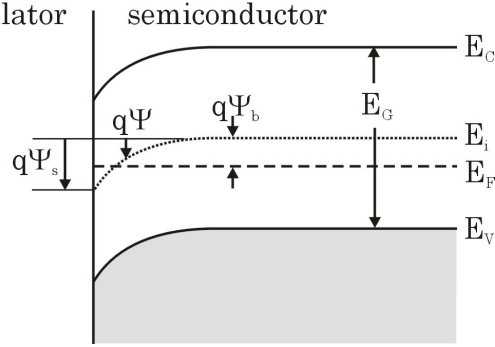


Figure 2.8: Energy-band diagram of a MIS-structure at the insulator-(p-type) semiconductor interface. The potential ψ is defined to be zero in the semiconductor bulk and is measured with respect to the intrinsic Fermi level E_i .

holes are accumulated at the interface. Second, if a small positive voltage is applied, the valence band bends downward and the hole concentration decreases towards the interface. A depletion layer is formed. Third, if the positive voltage increases, the intrinsic Fermi level E_i will cross the Fermi level E_F at a certain value. Then the conduction band is closer to the Fermi level than the valence band, which leads to an inversion layer at the interface because the concentration of the electrons exceed the concentration of the holes.

2.2.3 Surface space-charge region

In Figure 2.8 a more detailed band diagram at the insulator-semiconductor interface is depicted. Similar to an MS-junction, there is a band bending at the interface due to work function differences and applied biases across the junction. This band bending can be expressed as a potential ψ , which is defined with respect to the intrinsic Fermi level E_i and is set to be zero within the semiconductor bulk.

In a semiconductor the electron concentration n and hole concentration p as a function of ψ are given by

$$n = n_0 e^{\frac{q\psi}{kT}} \quad (2.12)$$

$$p = p_0 e^{-\frac{q\psi}{kT}} \quad (2.13)$$

where k is the Boltzman constant, T is the temperature and n_0 and p_0 are the thermal equilibrium densities of electrons and holes in the bulk, respectively. At the surface of a p-type semiconductor, the surface potential ψ_s can be distinguished to be in the following regions:

- $\psi_s < 0 \Rightarrow$ bands bend upward \Rightarrow holes are accumulated at the interface
- $\psi_s = 0 \Rightarrow$ bands are flat \Rightarrow carrier concentrations are n_0 and p_0 at the interface

- $\psi_b > \psi_s > 0 \Rightarrow$ bands bend downward \Rightarrow holes are depleted at the interface
- $\psi_s = \psi_b \Rightarrow$ both bands have the same energy distance to $E_F \Rightarrow$ hole and electron concentration are equal at the interface
- $\psi_s > \psi_b \Rightarrow$ the conduction band is closer to E_F than the valence band \Rightarrow inversion, i.e. electron concentration exceeds hole concentration at the interface

In order to calculate the surface potential ψ_s at the semiconductor-insulator interface, one has to solve the Poisson equation (2.2) using

$$\rho = q(N_D - N_A + p - n) \quad (2.14)$$

for the carrier concentration ρ , where N_D and N_A are the donor and acceptor concentrations, respectively. Inserting equation (2.14) in (2.2) gives

$$\frac{d^2\psi}{dx^2} = -\frac{q}{\epsilon_s} [p_0 (e^{-\beta\psi} - 1) - n_0 (e^{\beta\psi} - 1)] \quad (2.15)$$

where $\beta = q/kT$.

The spatial distribution of $\psi(x)$ in accumulation can be calculated using the approximation that the concentration of the minority carriers in the bulk is zero. Hence, one can expand the Taylor series of the exponential term to the first order, giving

$$\frac{d^2\psi(x)}{dx^2} = \frac{q\beta p_0}{\epsilon_s} \psi(x). \quad (2.16)$$

Inserting the Ansatz

$$\psi(x) = \psi_0 e^{-x/\lambda_D} \quad (2.17)$$

into equation (2.16) finally gives

$$\frac{1}{\lambda_D^2} = \frac{q\beta p_0}{\epsilon_s} \Rightarrow \lambda_D = \sqrt{\frac{\epsilon_s}{qp_0\beta}}. \quad (2.18)$$

Hence, the potential within the semiconductor decays exponentially, with its characteristic length λ_D , which is called the Debye length. It depends on the relative permittivity of the semiconductor, which is a material property, the temperature and the equilibrium density of the majority carriers, which in classical semiconductors is mainly given by the doping concentration. In Figure 2.9 the Debye length at room temperature is plotted in dependence on the bulk carrier concentration for the permittivity of silicon and the permittivity of $3\epsilon_0$, which is typical for organic semiconductors. It can be seen that the Debye length decreases from a few tens of nanometers for low carrier concentrations ($10^{15} \text{cm}^{-3} - 10^{16} \text{cm}^{-3}$) to only few nanometers or even less for high concentrations ($10^{18} \text{cm}^{-3} - 10^{20} \text{cm}^{-3}$). Therefore applying a bias across a MIS-junction leads to a band bending, that extends nanometers

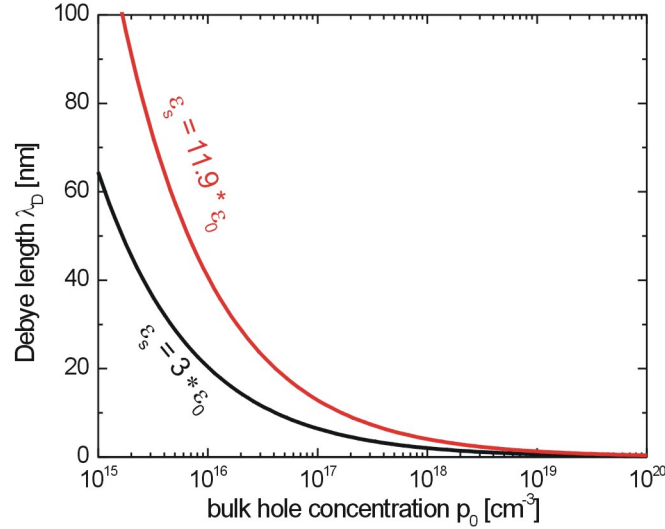


Figure 2.9: Debye length in dependence on the bulk carrier concentration for the relative permittivity of silicon and the relative permittivity of $3\epsilon_0$, which is typical for organic semiconductors.

into the semiconductor. Beyond the Debye length the applied bias gets screened and the potential of the bands and thus the carrier concentrations remain unaffected.

In order to calculate the surface charge density Q_s , the electric field F_s at the semiconductor surface in dependence of the surface potential ψ_s has to be determined. As we want to consider accumulation, depletion and inversion, minority carriers can not be neglected any more. Integrating equation (2.15) from the bulk towards the semiconductor surface

$$\int_0^{d\psi/dx} \left(\frac{d\psi}{dx} \right) d \left(\frac{d\psi}{dx} \right) = -\frac{q}{\epsilon_s} \int_0^\psi [p_0 (e^{-\beta\psi} - 1) - n_0 (e^{\beta\psi} - 1)] d\psi \quad (2.19)$$

and using the relationship $F = -d\psi/dx$ finally gives for the electric field at the surface F_s

$$F_s = \pm \frac{\sqrt{2kT}}{q\lambda_D} \left[(e^{-\beta\psi_s} + \beta\psi_s - 1) + \frac{n_0}{p_0} (e^{\beta\psi_s} - \beta\psi_s - 1) \right]^{1/2}. \quad (2.20)$$

with positive sign for $\psi > 0$ and negative sign for $\psi < 0$.

Finally one obtains the surface charge density Q_s by using Gauss's law

$$Q_s = -\epsilon_s F_s = \pm \epsilon \frac{\sqrt{2kT}}{q\lambda_D} \left[(e^{-\beta\psi_s} + \beta\psi_s - 1) + \frac{n_0}{p_0} (e^{\beta\psi_s} - \beta\psi_s - 1) \right]^{1/2} \quad (2.21)$$

In Figure 2.10, equation (2.21) is plotted as a function of the surface potential ψ_s . In the accumulation regime, the charge density Q_s increases exponentially with the absolute value

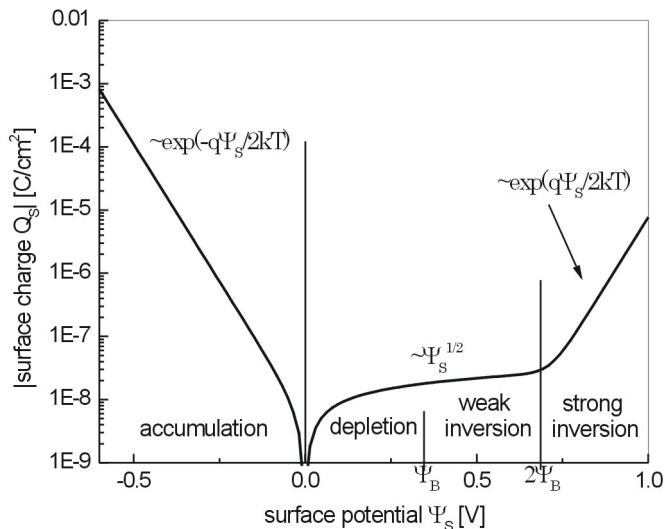


Figure 2.10: Space charge density in a p-type semiconductor of a MIS-junction in dependence on the applied voltage.

of ψ . This is the regime which thin film transistors operate at, as we will see in section 2.3. In the depletion and weak inversion regime, Q_s increases slowly with the square root of ψ while for strong inversion the charge goes up exponentially as in accumulation but this time the charge is carried by the minority carriers (electrons in the case of a p-type semiconductor). A popular device working in this regime is the MOSFET (= metal oxide semiconductor field effect transistor).

2.3 Thin film transistor

2.3.1 Principle of a TFT

The design of a thin film transistor (TFT) is depicted in Figure 2.11. It is a three terminal device with charge flowing from source to drain. The third contact, which is called gate, modulates the conductance of the semiconductor between source and drain and thus can turn the transistor on and off.

Mainly two different versions of TFTs are realized. The first one is called bottom-contact TFT, which is shown on the left. The gate electrode is first placed on the substrate. Alternatively, the substrate is conducting itself and serves already as gate contact. An insulating layer is then placed above the gate. Metallic source and drain electrodes are located on top of the insulating layer, before the final semiconducting layer finishes the

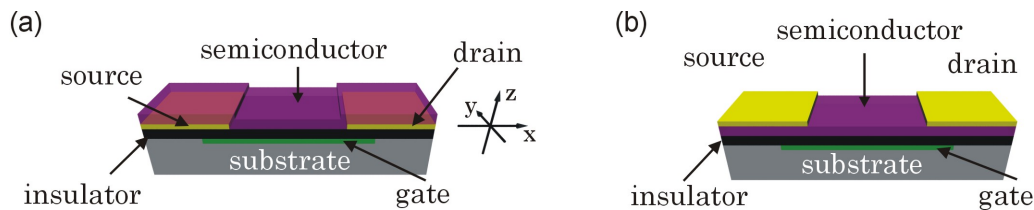


Figure 2.11: Sketch of a (a) bottom-contact TFT and (b) top-contact TFT.

TFT-structure. The region between source and drain is called channel with its characteristic channel length, which is the distance from source to drain, and the channel width, which is the expansion of the source or the drain contact edge. The alternative structure is shown on the right and is called top-contact TFT. The only difference to its bottom-contact counterpart is that the semiconducting layer is situated not on top of source and drain but below these contacts. An advantage of the bottom-contact transistor geometry is the possibility to produce these devices in large quantity as all contacts can be prepared using optical lithography. In case of top-contact geometry this is difficult as optical lithography easily destroys the semiconducting layer due to solvents that have to be used.

A TFT can be regarded as a combination of a MIS-junction (see section 2.2) and two MS-junctions (see section 2.1). The MIS-junction is realized along z -direction (compare Figure 2.11) from gate to the semiconductor, while the MS-junctions exist along x -direction, one between source and the semiconductor, and one between drain and the semiconductor. As it was shown in section 2.2 in case of a p-type semiconductor, a negative voltage leads to an accumulation of holes, while a positive voltage depletes the majority carriers at the insulator-semiconductor interface. Hence, in a TFT, holes are accumulated for a negative voltage, while a positive gate voltage depletes the transistor channel. If source and drain are shorted, this accumulation or depletion only depends of the applied gate voltage and is spatially uniform within the transistor channel, as it is in a MIS-junction.

However, as soon as a bias is applied between source and drain, the symmetry in the device is broken, because the potential within the channel is not constant anymore. In a TFT, the standard biasing is depicted in Figure 2.12(a). The source contact is grounded and two biases are applied, one between source and gate, which is called gate voltage V_G , and one between source and drain, which is called source-drain voltage V_{SD} . Let us assume that negative voltages are applied at both contacts, gate and drain, with $|V_{SD}| > |V_G|$. To further simplify, let us also assume that the flat-band voltage (see section 2.2) and the contact resistances are zero in the TFT. Hence, the potential difference between the semiconductor channel in vicinity of source and gate is close to V_G . As $V_G < 0$ and $V_{fb} = 0$, holes are accumulated at the semiconductor-insulator interface (see Figure 2.7(a)). As $V_{SD} < 0$, both, the potential in the semiconductor and the potential difference between semiconductor and gate decrease towards drain (see Figure 2.12(a)), leading to a reduction of the surface potential $|\psi_s|$ of the semiconductor (see Figure 2.12(b)). Thus, according to Figure 2.10, the space-charge density in the semiconductor gets smaller. At a certain

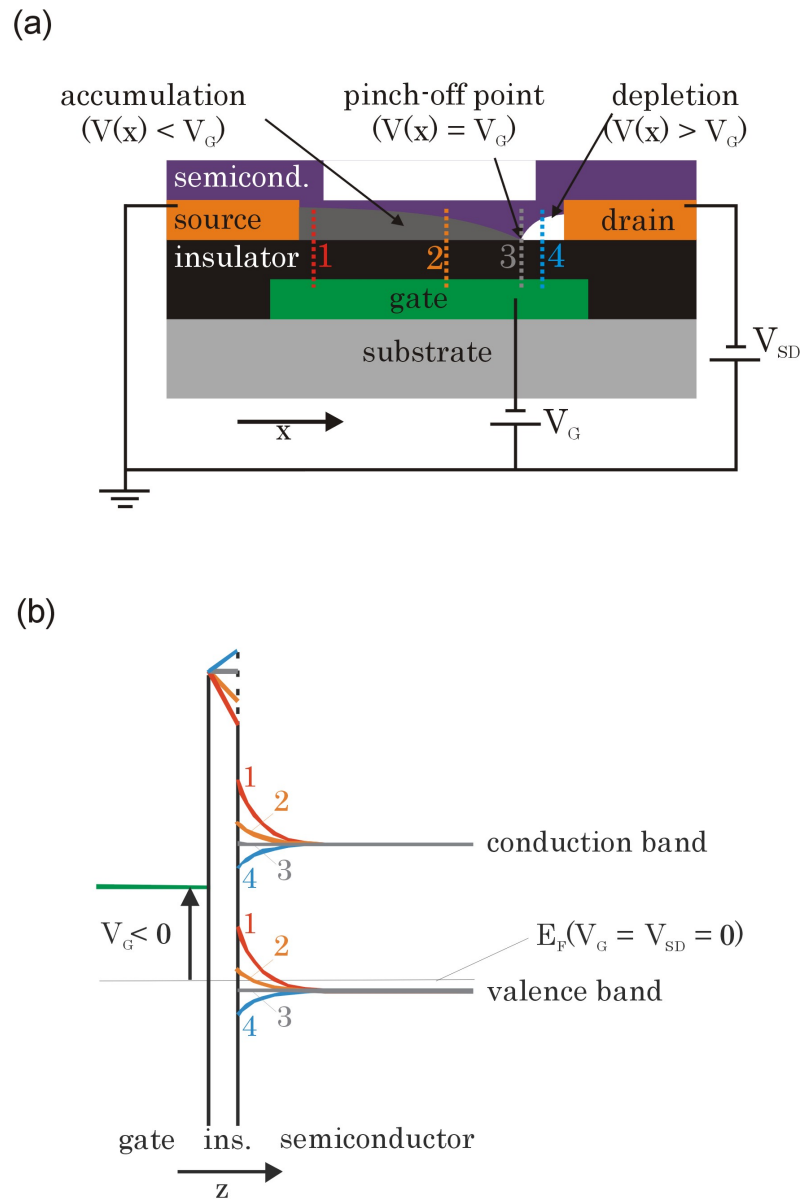


Figure 2.12: Spatially dependence of the band bending in a TFT. (a) Schematic view of the potential drop between source and drain for $V_{SD} < V_G < 0$. The spatially dependent potential difference between the semiconductor-insulator interface and gate is sketched within the channel (b) Energy-band diagram of the TFT under the same biasing for different spatial positions. The rising numbers correspond to the cuts shown in (a), and approach drain. Section 1 and 2 show decreasing accumulation towards drain, section 3 the pinch-off point with flat-band condition, and section 4 depletion.

position in the semiconductor, which is called pinch-off point, the potential difference between the semiconductor and gate is zero. Beyond this point, the transistor is not in accumulation any more, but in depletion. Theoretically, it is possible to get an inversion layer with an accumulation of minority carriers in the vicinity of the drain contact. But contact materials are usually chosen to minimize the difference between the valence band of the p-type semiconductor and the work function of the contacts in order to avoid large injection barriers for holes (see section 2.1.1). Therefore contact resistance is minimized for holes, but as bandgaps of semiconductors are in the range of $1\text{ eV} - 3\text{ eV}$, the difference between the conduction band of the semiconductor and the metal work function of the contact is too large to inject electrons. Therefore, the upward band bending is limited because the needed charge to induce the change of the potential can not be accommodated by electrons. Hence, TFTs usually operate not in inversion but in accumulation.

Generally, TFTs with a p-type semiconductor are in the off-state, i.e. no current flows between source and drain, when a positive gate voltage is applied, because the whole transistor channel is depleted of holes. For a positive gate voltage, the TFT is in its on-state. Two different regimes can be distinguished in the on-state. First, for $|V_{SD}| < |V_G|$, holes are accumulated at the semiconductor-insulator interface throughout the whole channel region. If the source-drain voltage is much smaller than the gate voltage, one can even assume a constant charge-carrier density throughout the channel. This operating state is called linear regime. Second, for $|V_{SD}| > |V_G|$ holes are accumulated close to source but beyond a certain point, which is called pinch-off point, the transistor channel is depleted. The TFT is in the so called saturation regime. The quantitative treatment in the next section will show, where these terms (linear and saturation) originate from.

2.3.2 Current-voltage characteristic

Linear regime

As described qualitatively in the last section, if only a small source-drain voltage is applied, the transistor can be described similar to a MIS-junction. The only condition that must be fulfilled is, that the insulator thickness must be much smaller than the channel length. Consequently, we can use the gradual channel approximation

$$\left| \frac{\partial F_x}{\partial x} \right| \ll \left| \frac{\partial F_y}{\partial y} \right| \quad (2.22)$$

which assumes that the charge density induced by the electric field parallel to the channel is much smaller than that by the electric field across the channel. Accordingly, we can assume that the charge, that is accumulated at a certain distance x from the source at the insulator-semiconductor interface, can be calculated as for a MIS-junction. The only difference is, that the surface potential $\psi_s(x)$ is not just induced by the gate voltage, but also by the potential $V(x)$, which is caused by the source-drain voltage with $V(x = \text{source}) = 0$ and $V(x = \text{drain}) = V_{SD}$. The potential drop across the semiconductor due to the gate voltage is given by

$$\psi_s(x) = V_G - V_{fb} - V_i \quad (2.23)$$

where V_{fb} is the flat-band voltage (see section 2.2.1) and V_i is the voltage drop across the insulator. At the semiconductor-insulator interface, the continuity of the electric field implies

$$\epsilon_s F_s = \epsilon_i F_i \quad (2.24)$$

where ϵ_s , ϵ_i , F_s and F_i are the permittivities and the electric fields of the semiconductor and the insulator, respectively. Using the insulator capacitance per unit area $C_i = \epsilon_i/d_i$ and inserting equation (2.24) into equation (2.23) finally leads to

$$V_G = -V_{fb} + \psi_s(x) + \frac{\epsilon_s F_s}{C_i}. \quad (2.25)$$

If we assume that $\psi_s > kT$, which is only about 25 meV at room temperature, the equation (2.20) for the electric field in a MIS-junction gets reduced to

$$F_s \approx \sqrt{\frac{2kTn_0}{\epsilon_s}} \exp\left(\frac{\beta\psi_s}{2}\right). \quad (2.26)$$

Therefore, the linear term of ψ_s in equation (2.25), which represents the potential drop across the semiconductor, is much smaller than the potential drop of the insulator, which is proportional to $\exp(\psi_s)$. Hence, most of the gate voltage already drops at the insulator and the potential in the semiconductor is mainly given by the potential $V(x)$, caused by V_{SD} . Consequently, the spatially depending space charge per unit area can be assumed to be

$$Q(x) = -C_i [V_G - V_{fb} - V(x)]. \quad (2.27)$$

Since the resistance is not constant along the channel, we use the differential form of Ohm's law

$$dV = I_{SD} dR. \quad (2.28)$$

where I_{SD} is the source-drain current. Besides the accumulated charge density $Q(x)$, we also have to take into account the bulk charge carrier density $Q_0 = qp_0 d_s$, where p_0 is the bulk hole density and d_s is the semiconductor thickness.

Using the Drude model with

$$\sigma(x) = qp(x)\mu \quad (2.29)$$

where $\sigma(x)$ is the channel conductance, $p(x)$ is hole concentration, q the elementary charge and μ the constant mobility of the semiconductor, we finally get

$$dV = \frac{I_{SD} dx}{W\mu (|Q(x) + Q_0|)}. \quad (2.30)$$

Inserting equation (2.27) and integrating equation (2.30) from source ($x = 0, V = 0$) to drain ($x = L, V = V_{SD}$) leads to

$$I_{SD} = \frac{W}{L} \mu C_i \left[(V_G - V_T) V_{SD} - \frac{V_{SD}^2}{2} \right] \quad (2.31)$$

with the threshold voltage V_T defined as

$$V_T = \frac{ep_0 d_s}{C_i} + V_{fb}. \quad (2.32)$$

If $|V_{SD}| \ll |V_G - V_T|$ then equation can be simplified to

$$I_{SD}^{lin} = \frac{W}{L} \mu C_i (V_G - V_T) V_{SD}. \quad (2.33)$$

As the source-drain current increases linearly with the applied source-drain voltage, this is called the linear regime. Please note, that $I_{SD} \neq 0$ for $V_G = 0$ due to the threshold voltage, which arises from the flat-band voltage as well as from the bulk conductance.

Saturation regime

In the linear regime, there is a complete accumulation channel from source to drain. This changes if $|V_{SD}| > |V_G - V_T|$. Under such a biasing, there is only an accumulation channel from source up to the pinch-off-point. Beyond this point the channel is depleted as shown in Figure 2.12. According to Brown et. al. [16] and Horowitz et. al. [17] the source-drain current in this regime can be calculated by the sum of two integrals

$$I_{SD} = \frac{W}{L} \mu C_i \int_0^{V_G} (V_G - V_T - V) dV + \frac{W}{L} \mu ep_0 \int_{V_G}^{V_{SD,sat}} (d_s - w) dV \quad (2.34)$$

where the first integral accounts for the accumulation channel up to the pinch-off point, where $V(x) = V_G$, while the second integral corresponds to the depletion layer beyond it. With

$$w(x) = \frac{\epsilon_s}{C_i} \left[\sqrt{1 + \frac{2C_i^2 (V_G - V_{fb} - V(x))}{eN\epsilon_s}} - 1 \right] \quad (2.35)$$

for the depletion width, equation (2.34) can be simplified to

$$I_{SD,sat} = \frac{W}{2L} \mu C_i (V_G - V_T)^2 \quad (2.36)$$

with V_T given by equation (2.32). The result shows that I_{SD} does not increase with V_{SD} in this regime. Therefore, it is called saturation regime. Taking both, the linear and the saturation regimes, into account, the conductance curves of a p-type TFT should behave as depicted in Figure 2.13.

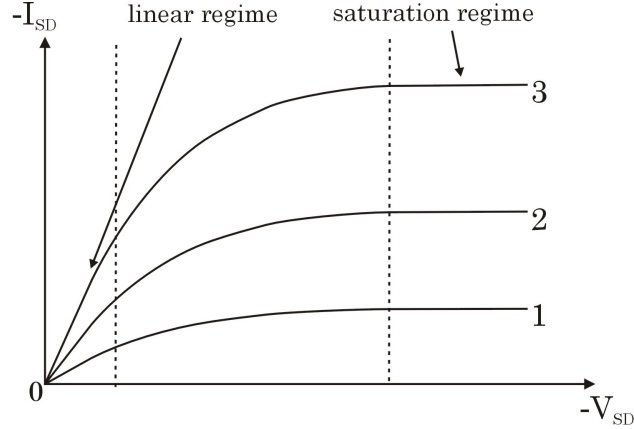


Figure 2.13: Schematic view of conductance curves for different gate voltages with $|V_G(1)| < |V_G(2)| < |V_G(3)|$.

2.3.3 Characteristic transport parameters

Mobility

The mobility μ is most generally defined as the relationship between the drift velocity of the charge carriers v_d and the electric field F , given by

$$v_d = \mu F. \quad (2.37)$$

The mobility is of special importance since it is independent of geometrical factors (e.g. channel length, channel width or insulator thickness) and determines the amount of current flowing in the transistor under a given biasing. The mobility of a TFT can be derived either from the linear regime or from the saturation regime (see section 2.3.2). In the linear regime, differentiating the source-drain current with respect to the gate voltage gives

$$\frac{\partial I_{SD,lin}}{\partial V_G} = \frac{W}{L} \mu_{lin} C_i V_{SD} \quad (2.38)$$

which can be solved for the linear mobility μ_{lin}

$$\mu_{lin} = \frac{L}{WC_i} \frac{1}{V_{SD}} \frac{\partial I_{SD,lin}}{\partial V_G} = \frac{W}{L} \mu_{lin} C_i V_{SD}. \quad (2.39)$$

Therefore, the mobility can be calculated from the slope $m_{lin} = \frac{\Delta I_{SD}}{\Delta V_G}$ of the transconductance curve, which is a plot of the source-drain current against the gatevoltage, in the linear regime, i. e. for $|V_{SD}| \ll |V_G - V_T|$ (see Figure 2.14 (a)).

It is also possible to determine the mobility using the saturation regime. Therefore, we have to use the square root of equation (2.36)

$$\sqrt{I_{SD,sat}} = \sqrt{\frac{W}{2L} \mu_{sat} C_i (V_G - V_T)}. \quad (2.40)$$

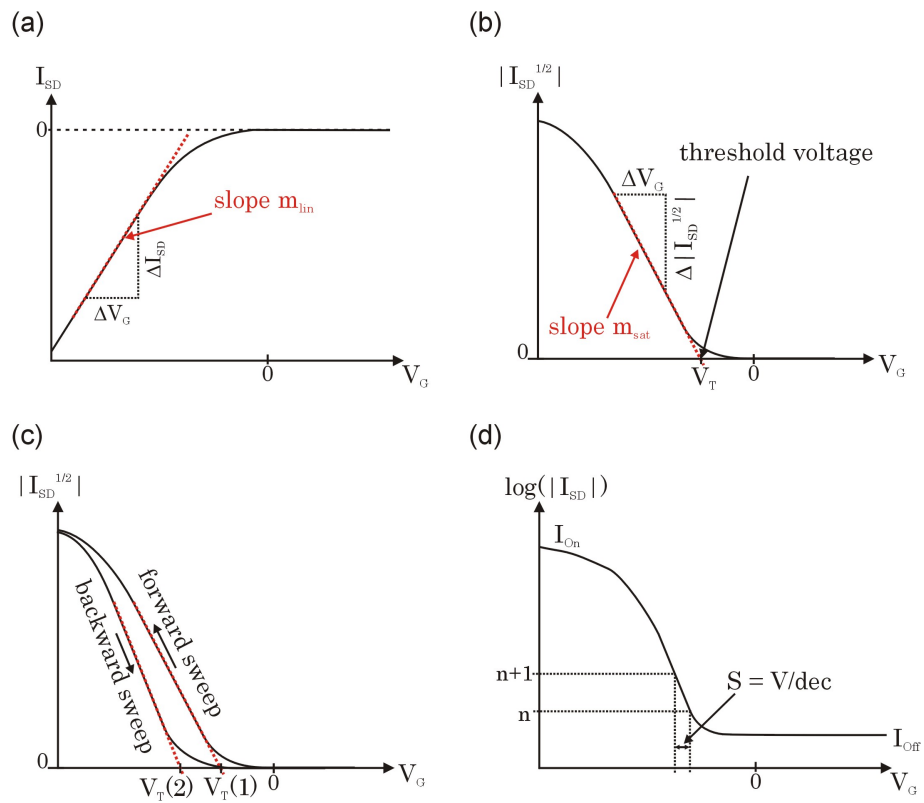


Figure 2.14: Determination of the transport parameters of a TFT. (a) Plot of I_{SD} vs. V_G in order to determine the linear mobility. (b) Plot of $\sqrt{I_{SD}}$ vs. V_G in order to determine the saturation mobility and the threshold voltage. (c) Semilogarithmic Plot of I_{SD} vs. V_G in order to determine the on-off ratio as well as the subthreshold swing. (d) Plot of $\sqrt{I_{SD}}$ vs. V_G for both gate voltage sweep directions in order to determine hysteresis.

Differentiating this equation with respect to V_G finally gives for the saturation mobility μ_{sat} the following expression

$$\mu_{sat} = \frac{2L}{WC_i} m_{sat}^2 \quad (2.41)$$

where $m_{sat} = \frac{\Delta\sqrt{I_{SD,sat}}}{\Delta V_G}$. The slope m_{sat} can be evaluated by making a linear fit of a plot of the square root of the source-drain current against the gate voltage for $|V_{SD}| \gg |V_G - V_T|$, as it is shown in Figure 2.14 (b).

The mobility is defined as a material constant of the semiconductor. Therefore, the mobility should not depend whether it is taken from the linear regime or from the saturation regime, i.e. $\mu_{lin} = \mu_{sat}$. Nevertheless, this is scarcely true. Mainly, there are two reasons for this deviation of ideal behavior. First, one has not to forget, that we are only able to measure an extrinsic mobility, which includes contact resistances at source and drain. Second, the semiconductor itself is not a perfect homogeneous single crystal. Mostly, it consists of grains with grain boundaries of low mobility and lots of structural defects leading to localized electronic states in the bandgap. This can cause mobility dependencies on the electric field, the temperature or the source-drain voltage.

Threshold voltage and onset voltage

It is desirable that the TFT can be switched between the on-state and the off-state at a gate voltage which is as close to zero as possible in order to use little voltages for circuit application. Two commonly used parameters that account for this are the threshold voltage and the onset voltage. The threshold voltage V_T can be evaluated using equation (2.40). For $V_G = V_T$ the source-drain current vanishes. Thus, determining the crossing point of the linear fit, that is used to determine the saturation mobility, with $I_{SD} = 0$ supplies us with the threshold voltage, as it is depicted in Figure 2.14 (b).

Alternatively, one can use the onset voltage V_{on} as parameter for the switching position. It is defined as the minimum gate voltage, which is needed for a measurable field-effect-induced source-drain current. To determine it with the highest possible precision, one should plot the source-drain current logarithmically against the gate voltage. The deviations from zero are caused by the flat-band-voltage (see section 2.2.3) as well as interface-dipoles at the insulator-semiconductor interface.

Subthreshold swing

If in a p-type TFT the gate voltage is only slightly more negative than the threshold voltage, the source-drain current increases exponentially before it passes into the saturation regime, where it is given by equation (2.36). This regime is called subthreshold regime. If I_{SD} is plotted logarithmically against V_G , it is possible to determine the subthreshold swing, which is defined as the amount of gate voltage which is needed to increase I_{SD} by a factor of one order of magnitude (see Figure 2.14 (c)). It is desirable to achieve as small swings as possible in order to switch the transistor as fast as possible. Please note, that

the subthreshold swing is proportional to the capacitance of the insulator. This has to be taken into account if one wants to compare TFTs with different insulator thicknesses.

On-off ratio

The on-off ratio of the transistor is the ratio between the current in the off-state and in the on-state, which is determined using a semilogarithmic plot of I_{SD} vs. V_G (see Figure 2.14 (c)). This parameter should always be given with the according gate voltages which were used to determine the ratio. Ideally this ratio should be infinity, meaning that the transistor closes perfectly. But as currents through the bulk are difficult to avoid completely, on-off-ratios which exceed 10^6 can be regarded as very good for TFTs. Another origin of off-currents are leakage currents through the insulator, which can be minimized by increasing the insulator thickness.

Hysteresis

In an ideal device, the source-drain current should only depend on V_{SD} and V_G , but not on the bias history of the device. In reality however, TFTs often have a hysteresis, which is defined as the difference between the threshold voltages of two subsequently performed sweeps, one sweeping from the off-state to the on-state and the other one sweeping from the on-state to the off-state (see Figure 2.14 (d)). For stable operation, one wants to have a hysteresis which is as small as possible. Hysteresis always exists if the transistor does not immediately get into an equilibrium state. Similar to the field dependence of the mobility, this can be caused by localized states within the semiconductor bandgap that e.g. can arise from crystal imperfection. Depending on their energies, these states can be filled with charges at different time scales, thus charging the semiconductor film with immobile carriers. This changes the amount of free carriers and hence the source-drain current.

Chapter 3

Organic semiconductors

This chapter begins with a short overview of organic semiconductors. Subsequently, it will be shown, how structural, electronic and optical properties are correlated in such materials. Special emphasis is given to differences of organic materials in comparison to classical inorganic semiconductors such as silicon or germanium. Finally, a brief introduction of the structure of pentacene thin films is presented. The contents of this chapter is mainly based on the very elaborated reference book of Pope and Swenberg [18] and the more concise work of Schworer and Wolf [19].

3.1 Overview of organic semiconductors

In the last two decades, chemists have synthesized a huge amount of new organic semiconducting molecules. The chemical structures of some established materials are depicted in Figure 3.1.

The variety of organic molecules is one of the major advantages compared to inorganic semiconductors, as important parameters, such as the bandgap, can be tuned over a wide range. For example, in the case of OLEDs, using an appropriate mixture of organic compounds leads to white light emitting diodes.

Organic semiconductors can be roughly distinguished into two material classes, namely polymers and small molecules. Polymers are predominantly used in organic LEDs. The main advantage of these molecules is their solubility in lots of standard solvents, like propanole or acetone, which enables inexpensive production on a large scale using standard fabrication techniques, such as spin coating or printing. Moreover, they are usually chemical very stable, which is crucial for applications, where long time operation should be a mandatory quality. On the downside, these materials have typical mobilities of about $10^{-5} \text{ cm}^2/(\text{Vs})$, which is very low in comparison to amorphous silicon. This low conductance arises from their low structural order. Usually, the large and complex chemical structure of these molecules form amorphous films, where charge transport is impeded by the low degree of order. For OLEDs, this very low mobility is sufficient, as the charge carriers have to bridge only very small distances, typically in the order of 100 nm . In the

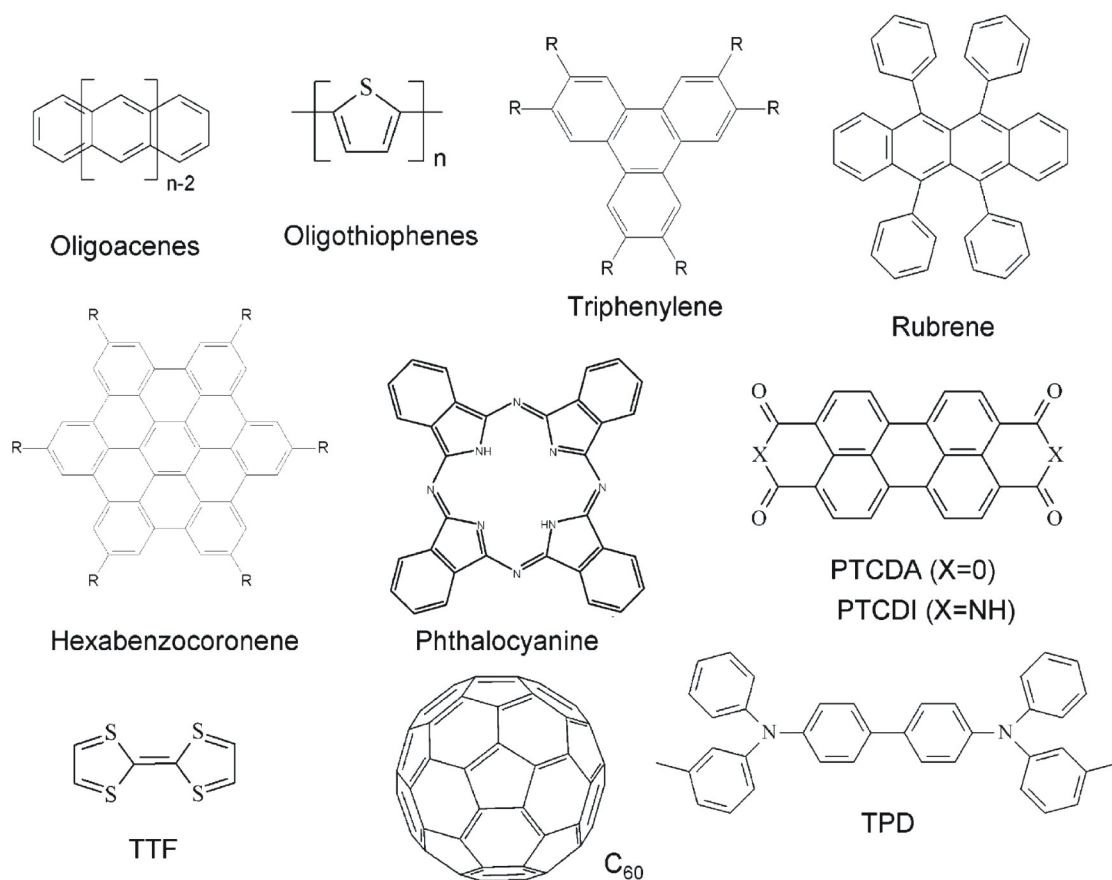


Figure 3.1: Chemical structures of some of the most studied semiconductors. Adapted from [20].

case of organic thin film transistors (OTFT), typical distances between the contacts are larger. Therefore, a mobility comparable to amorphous silicon is necessary to enable even low speed operation in an electronic circuit. This is why small molecules are considered as the most promising candidates. Their mobilities have reached values in the order of $1\text{ cm}^2/(\text{Vs})$, which is regarded as the benchmark for applications. This relatively high mobility can be achieved, since these crystals can form layers with a much higher order compared to polymers.

Whether polymers or small organic molecules, all organic semiconductors share one common property, namely the alternating double and single bonds in their chemical structure. This leads to a π -conjugated electron system, which determines the electronic and optical behavior in these materials, as it will be shown in the following sections.

3.2 Molecular orbitals

3.2.1 Conjugated electron system

The chemical structure of organic semiconductors have one common characteristic: alternating single and double bonds between the carbon atoms. Therefore, the carbon atoms are sp^2 -hybridized, which leads to a planar structure of the molecule. The sp^2 -orbitals between two adjacent atoms overlap and form strong σ -bonds. The electrons within these orbitals are localized between the atoms. Decisive for the optical and electronic behavior of organic molecules are the so-called π -bonds, that arise from the overlap of the remaining p-orbitals of the carbon atoms, which are oriented perpendicularly to the molecular plane. The overlap of these p-orbitals create molecular orbitals, which are filled by the π -electrons. The π -electrons are, in contrast to σ -electrons, delocalized over the whole molecule. As their binding energy is much lower than those of σ -electrons, the π -orbitals are the highest-energy filled orbitals. The lowest-energy vacant orbitals are also π -orbitals, therefore these delocalized orbitals determine the optical and electronic properties of organic materials while σ -orbitals can be neglected.

In order to estimate the energy of the π -orbitals, the easiest assumption is to regard the molecule as a potential well with infinite high potential walls at the edges of the molecule and a constant potential in between. In this perimeter free electron orbital (PFEO) theory, all electron-electron and electron-nuclei interactions are neglected. A semi quantum-mechanical calculation with these assumptions leads to the following expression for the energy states E_q of the molecular orbitals

$$E_q = \frac{1.21 \cdot 10^6}{l^2} q^2 \quad (3.1)$$

where l is the perimeter of the molecule measured in Å and q represents the orbital angular momentum, which is quantized ($q = 0, 1, 2, \dots$) (see p. 8 at [18]).

In a system of condensed benzene rings, there are $2(2n+1)$ π -electrons, where n is the number of benzene rings. These molecules are called polyacenes, alternatively they are often called to belong to the anthracene family. The particular names are benzene, naphthalene, anthracene, tetracene and pentacene for $n = 1, 2, 3, 4,$ and 5 respectively (see Figure 3.2). Each orbital includes two electron states due to the spin of electrons, therefore q equals n for the highest occupied molecular orbital, which is called HOMO, and q equals $n + 1$ for the lowest unoccupied molecular orbital, which is called LUMO. Therefore, one can estimate the lowest energy transition with equation (3.1), calculating the energy difference between the HOMO and the LUMO. Although these assumptions are pretty puristic, the comparison of the calculated transitions with the optically determined transitions show, that it can be used for a reasonable estimate (see Table 3.1).

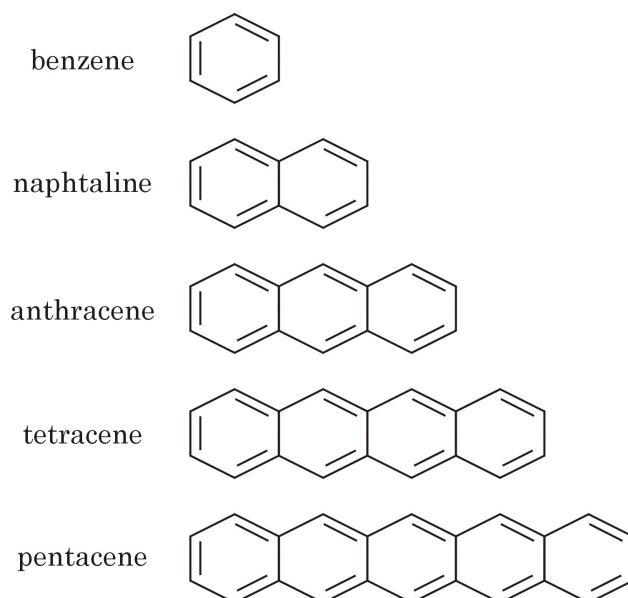


Figure 3.2: Chemical structures of the first five polyacene molecules.

molecule	Estimated HOMO-LUMO transition energies in eV using equation (3.1)	observed transition energies in eV
benzene	6.3	5.9
naphthalene	3.8	4.3
anthracene	2.7	3.3
tetracene	2.1	2.6
pentacene	1.7	2.1

Table 3.1: Comparison of observed single-state excitation energies measured by optical absorption with estimates using PFEO theory.

3.2.2 Excitation states

So far, we have considered transitions between the highest occupied electronic state and the lowest unoccupied electronic state of a single organic molecule by using a theory, that exclusively takes the electron orbitals into account. In order to describe energy states in such a molecule more precisely, one has to include higher unoccupied electronic states, vibronic levels and last but not least the spin of the electrons. A schematic view of the energy states in a molecule, considering these levels, is depicted in Figure 3.3.

In the ground state, all orbitals are filled with two electrons up to the HOMO. Due to Pauli's rule, the electrons are oriented antiparallel in each orbital, and the spin of the molecule is zero. The ground state is always a singlet state of the molecule and is called S_0 , since the number of π -electrons is even. This ground state has vibrational sub levels, but the internal conversion (IC) in these molecules, which is the nonradiative decay of

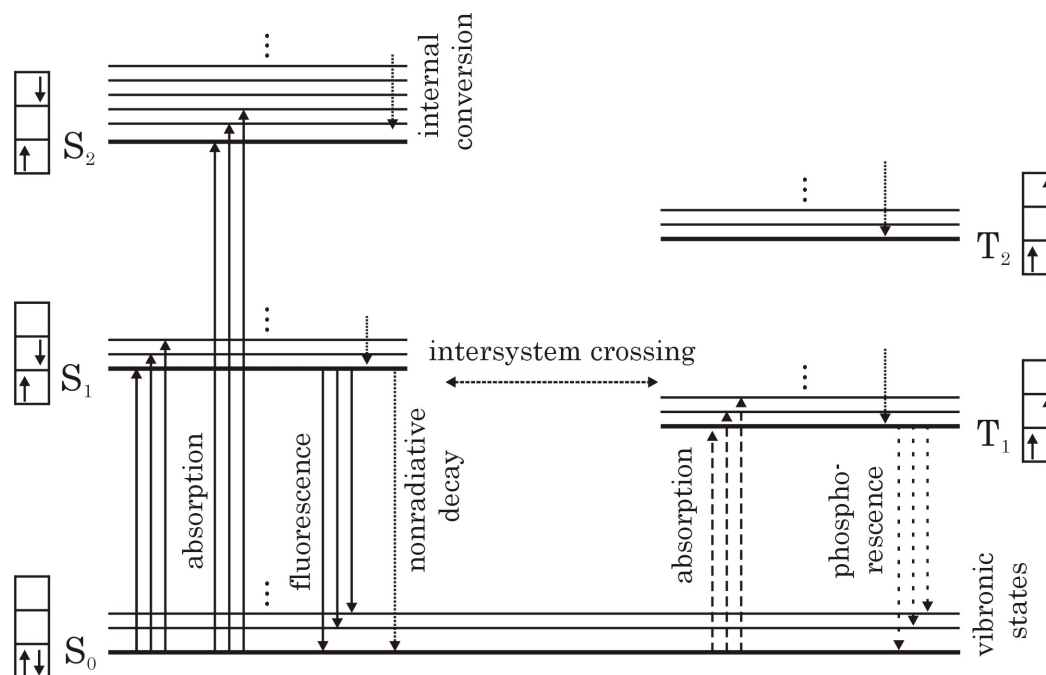


Figure 3.3: Excitations scheme of an organic molecule. Only the first two singlet and triplet excitations and few vibronic sub levels for each electronic state are depicted. The symbols next to the excitation levels represent the orbital and spins of the electrons.

vibronic excitations, is very fast in the order of picoseconds. If an electron is excited into the lowest unoccupied molecular level, there are two orbitals, which are filled by only one electron. These two electrons can have an antiparallel or a parallel orientation. In the case of antiparallel orientation, the state is called S_1 , as it is the first excited singlet state. If the electrons have parallel orientation, the state is called T_1 , as it is the first excited triplet state, which has a spin of $S = 1$. Furthermore, there are higher excitation states for singlet states S_2, S_3, \dots and triplet states T_2, T_3, \dots , as electrons fill higher unoccupied molecular orbitals. All electronic states also have additional vibronic excitation levels, which possess very short decay times.

If one illuminates such molecules with an appropriate wavelength, it is possible to excite the molecule by the absorption of a photon. Usually, the electron gets excited into a vibronic sublevel, but due to the very fast internal conversion, it decays into the vibronic ground level within picoseconds. Excited singlet states can be generated with a higher efficiency than triplet states, which leads to very different absorption coefficients. For the singlet transition $S_1 \leftarrow S_0$, the absorption coefficient is about 10^5 cm^{-1} for typical organic molecules, and thus an order of magnitude larger than the absorption coefficient for triplet excitations $T_1 \leftarrow S_0$, which is 10^{-4} cm^{-1} for anthracene, for example. The reason for these different excitation efficiencies is, that the dipole transition moment does not interact with the spin of the electrons, i.e. the selection rule is $\Delta S = 0$. Consequently, the intersystem crossing rate between an excited singlet state and a triplet state is usually very small,

because the spin of the molecule must be conserved. In turn, the optical excited singlet states usually decay predominantly to the electronic ground state, with a typical lifetime between 10^{-9} s and 10^{-6} s. The radiative part of this transition is called fluorescence. Triplet excitations typically have much longer lifetimes (up to a few seconds), because the decay channel from the triplet state to the ground state is, due to the selection rule, also not allowed. Therefore, the phosphorescence, which is the radiative part of the transition from the triplet state to the ground state, is much weaker than the fluorescence. The only way to excite the T_1 state efficiently and to harvest the phosphorescence with a high efficiency, is to dope the organic molecules with heavy atoms. These atoms increase the spin-orbit coupling, that softens the selection rule. Hence, both, the intersystem crossing and the singlet-triplet transitions are allowed in such systems.

3.3 Organic crystals

3.3.1 Excitons

The excitation states in organic crystals are called excitons. Their excitation spectrum in organic crystals is dominated by the molecular orbitals of single molecules, which were described in section 3.2. This is due to the strong delocalization of the π -conjugated electron system. The weak intermolecular van der Waals interactions in organic crystals only correct the energy spectrum. The van der Waals interactions usually decrease the energy eigenstates of the organic crystal compared to the energies of the corresponding molecular orbitals. Excited states, i.e. excitons, do also possess an additional binding energy E_B . Although for an exact description, one has to consider the excitons as delocalized excitations of the organic crystal, which can be described using Bloch waves (see for example p.122 ff. of [19]), the binding energy can be easily explained, if the exciton is considered to be a particle. It consists of an electron in the previously unoccupied molecular orbital and a vacancy in the previously completely filled molecular orbital. This vacancy is usually called hole and can be regarded as a quasi-particle with a positive charge. Thus, an exciton can be described as an electron-hole pair. In order to separate the electron from the hole, one has to overcome the attractive coulomb energy between the two charges of the exciton, which is given by

$$E_B = \frac{q^2}{4\pi\epsilon r^2} \quad (3.2)$$

where r is the distance between the hole and the electron.

Different types of excitons

Excitons can be distinguished depending on the spatial separation r of the hole and the electron. In inorganic semiconductors like silicon or germanium, the distance of the electron and hole is usually one order of magnitude larger than the lattice parameters in the

crystal. Such an exciton is called Wannier exciton. The energy eigenstates are similar to the eigenstates of the hydrogen atom. Due to the reduced delocalization in organic crystals, such excitons have never been observed in organic crystals. In contrast, Frenkel excitons exhibit an r which is smaller than the distance between adjacent lattice sites. In the case of an organic crystal, this means, that hole and electron are located on the same molecule. These excitons, that have usually very high binding energies due to equation (3.2), can typically be excited with the highest efficiencies in most organic semiconductors. Another exciton, that exists in organic crystals, is the so called charge transfer (CT) exciton, where the electron and hole are located at adjacent molecules. In the case of unpolar organic crystals, these CT-states have higher excitation energies than Frenkel excitons, because the distance r is larger leading to a reduced binding energy.

Davydov splitting

In 1962, Davydov showed that exciton levels split, if more than one translationally invariant molecule exists in the unit cell of the organic crystal. This can be explained, if one describes the excitons as wave functions. Let the ground state functions of two uncoupled molecules be ϕ_1 and ϕ_2 with their corresponding energies $E_1 = E_2 = E_0$. Then, the wave function of both molecules, which is called dimer, is $\phi_G = \phi_1\phi_2$ with the energy $E_G = 2E_0$. If one of these molecules is excited to ϕ_1^* or ϕ_2^* with energy $E_1^* = E_2^* = E^*$, the wave function of the dimer becomes

$$\phi_{\pm}^* = \frac{1}{\sqrt{2}} (\phi_1\phi_2^* \pm \phi_1^*\phi_2). \quad (3.3)$$

Here, the energy of the excited dimer is $E_{\pm}^* = E_{\pm}^* = E_0 + E^*$. If there is an interaction V_{12} between the two adjacent molecules, it can be shown, that the degeneracy of the eigenstates is lifted with the following energies

$$E_{\pm}^* = E^* + E_0 \pm I_{12} \quad (3.4)$$

where I_{12} is the resonance interaction energy, given by

$$I_{12} = \langle \phi_1^*\phi_2 | V_{12} | \phi_1\phi_2^* \rangle. \quad (3.5)$$

This model can be expanded to organic crystals, if one assumes, that the resonance interaction is of short range character and thus dominated by next neighbor interactions. Hence, the energy splitting of $2I_{12}$ for a dimer has only to be multiplied with the number of next neighbors of the two translationally invariant molecules. In the case of anthracene, there are 4 next neighbors, leading to an energy splitting of $8I_{12}$, which is called Davydov splitting and is depicted in Figure 3.4.

If one wants to generate excitons optically, it is important to know the polarization of the transitions, which is determined by the transition dipole moments of the dimers

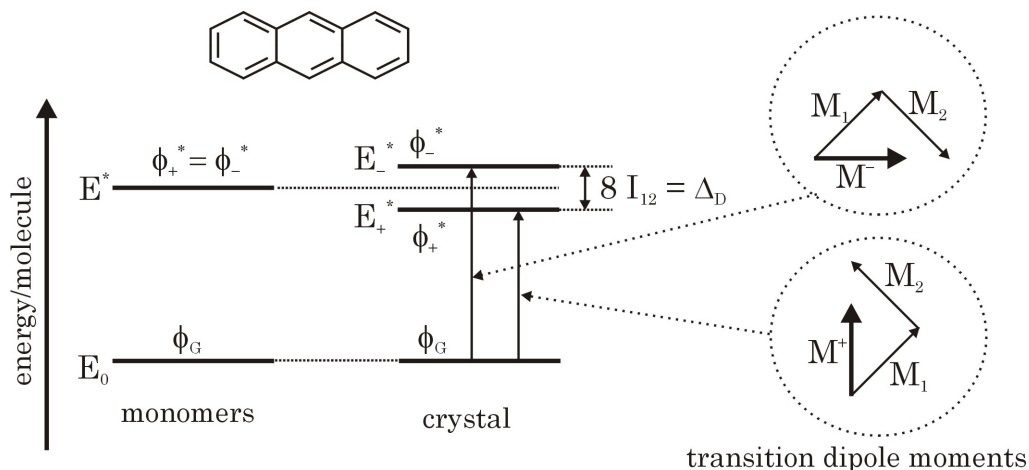


Figure 3.4: Energy-diagram of the Davydov-splitting with two translationally invariant molecules in a monoclinic unit, as in the case of anthracene, for example. The energy shifts due to van der Waals and Coulomb interactions are neglected. On the right, two perpendicularly oriented transition dipole moments are sketched (see text).

$$\mathbf{M}_{S_1 \leftarrow S_0}^{\pm} = \langle \phi_G | q\mathbf{r} | \phi_{\pm}^* \rangle = \frac{1}{\sqrt{2}} (\mathbf{M}^2 \pm \mathbf{M}^1) \quad (3.6)$$

where \mathbf{M}^1 and \mathbf{M}^2 are the transition dipole moments of the molecules 1 and 2, respectively. If the two identical molecules are not parallel or antiparallel orientated, there are two differently orientated transition dipole moments \mathbf{M}^+ and \mathbf{M}^- . In a crystal, the symmetry of the structure determines the relative orientation of the transition dipole moments. For example, in the case of anthracene, the structure is monoclinic. This means, that the absorption in anthracene and similar crystals is polarization dependent. In particular, absorption of light with energy E^+ and E^- is maximal for perpendicular orientation (see Figure 3.4).

Diffusion

When excitons are created in an organic material, they can move within the crystal. As excitons are polarized, but not charged, their motion is nearly unaffected by electric fields and hence, dominated by diffusion. The diffusion constant D and the mobility μ are related via the Einstein relation

$$D = \mu k_B T \quad (3.7)$$

where k_B is the Boltzmann constant and T is the temperature. For most organic crystals the diffusion constant is in the range of $10^{-3} \text{ cm}^2 \text{ s}^{-1}$ – $10^{-5} \text{ cm}^2 \text{ s}^{-1}$ at room temperature, at which excitons move incoherently. As excitons are of Frenkel type or charge transfer type, diffusion can be seen as a statistical hopping process from crystal site to crystal site

with a typical single step hopping time of 10^{-13} s. The diffusion length L of the excitons can be calculated by

$$L = \sqrt{Z \cdot D \cdot \tau} \quad (3.8)$$

where τ is the exciton lifetime and Z is 2, 4 and 6 for one-, two- and three-dimensional diffusion, respectively. The dislocation σ_D in each direction is given by

$$\sigma_D = \sqrt{D \cdot \tau}. \quad (3.9)$$

As it was explained in section 3.2.2, singlet excitons have usually lifetimes of less than a microsecond. Therefore, the diffusion length of singlet excitons is in the range of nanometers. However, for triplet excitons, the diffusion length can be in the micrometer scale, as the lifetime is much longer. Therefore, such excitations can transport their energy over substantial distances, for example out of a diffraction limited illumination spot, which is less than a micrometer.

3.3.2 Charge transport

Charge carriers

Similar to neutral excitations, that were described in the previous section, the properties of excess charge carriers are of interest, too. They also can be described by a model of molecular orbitals, which are altered by the relatively weak van der Waals interactions between adjacent molecules. However, a charge carrier, which is located at a specific molecule, is in contrast to an exciton not neutral. If an extra electron is in the LUMO of a specific molecule, it is a negative ion. Otherwise, if an electron is missing in the HOMO level of a specific molecule, or in the semiconductor language, an extra positively charged hole is in the HOMO, it leads to a positive ion. In both cases, the charged molecule polarizes its environment. This polarization is much faster than the transfer time of a charge carrier from site to site. Therefore, the polarization follows the moving charge carrier instantaneously. These charge carriers together with their adjacent polarization are called polarons.

The energy levels of the electron polarons E_e and hole polarons E_h correspond to states in the conduction band and in the valence band, respectively. Due to the polarization, the energies E_e and E_h are different in organic crystals and single molecules. The electronic polarization energy of holes P_h leads to the difference of the ionization energies of the molecule in the gas phase $I_G = E_h(\text{molecule})$ and the crystal $I_C = E_h(\text{crystal})$, and can thus be expressed as

$$P_h = I_G - I_C. \quad (3.10)$$

Accordingly, the electron polarization energy is given by

$$P_e = A_C - A_G. \quad (3.11)$$

where $A_C = E_e(\text{crystal})$ and $A_G = E_e(\text{molecule})$ are the electron affinities of the organic crystal and a single organic molecule, respectively. If quadrupole moments are neglected, the polarization energy is given by a summation of the interactions P_{id} of the charge with its induced dipole moments

$$P_e = P_h = \sum_{k=1}^{N-1} \frac{e^2 \bar{\alpha}}{2r_k^4} \quad (3.12)$$

where N is the number of all molecules in the crystal, $\bar{\alpha}$ is the average isotropic polarizability and r_k is the distance of the molecule k to the center of the charge. It is important to notice, that in organic crystal the polarizability is very high due to the weak van der Waals interaction. This can be seen in their low values of their dielectric constant ϵ , which is typically about $3\epsilon_0$ in organic semiconductors, while it is $11.9\epsilon_0$ for silicon, for example (see also section 2.1).

Ideally, in a perfect crystal at zero temperature, the polarization energies and hence the polaron energies would be discrete. However, in a real crystal at finite temperature, the distances r_k are significantly altered, as organic crystals are soft materials arising from the weak intermolecular forces. According to equation (3.12), compressed crystal regions lead to an increase of the polarization energy and hence, to polaron states within the bandgap. In contrast, stretched crystal regions lead to a decrease of the polarization energy, which generates polaron states outside of the bandgap. Therefore, the polaron states are statistically distributed, as it is depicted in Figure 3.5. Usually, it is assumed, that the states show a Gaussian energy distribution $G(E)$, which for hole polarons is given by

$$G(E) = \frac{N_h}{\sqrt{2\pi}\sigma_h} \exp\left[-(E - E_h)^2 / 2\sigma_h^2\right] \quad (3.13)$$

where N_h is the density of hole polarons and σ_h is the standard width of the hole distribution [4]. Accordingly, electron polaron states are Gaussian distributed as well, but centered at E_e . Usually, these distributed states are divided into two groups. Polarons with energies closely located at the center of the distribution, which means that $E - E_h \ll k_b T$ for hole polaron states and $E - E_e \ll k_b T$ for electron polaron states, can be regarded as states, which are available for transport, hence they can be filled with free carriers. These states form the valence band and the conduction band for holes and electrons, respectively. In contrast, states with energies further away from the distribution center are often called tail states of the bands and can be distinguished between those, that lie within the bandgap and those outside of the bandgap. States within the bandgap are attractive for charge carriers, but when a charge carrier is once located at such a state, it can not move further without gaining extra energy. Therefore, these states are called trap states. If these trap states are located close to the conduction or valence band, charge carriers can be thermally detrapped. These states are called shallow traps. States, that are further away from the band edges cannot be released easily and are called deep traps. States outside of the

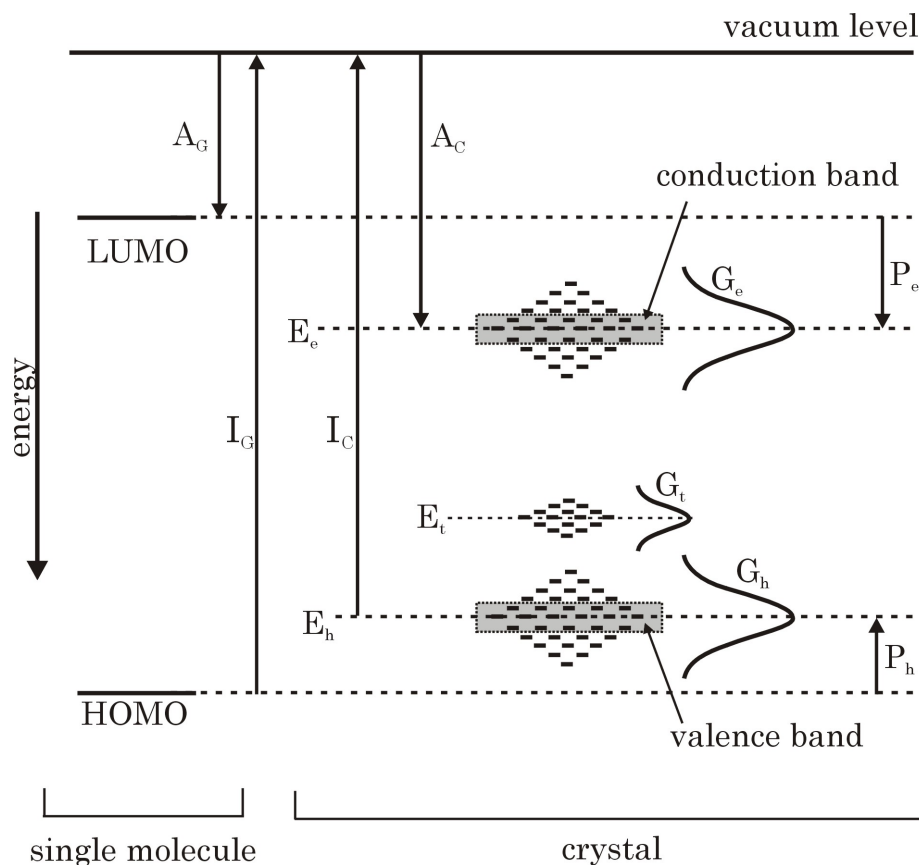


Figure 3.5: Energy-diagram of polaron states. On the left, the molecular orbital states of a single molecule are shown. On the right, the polaron states for organic crystals, that are altered by the polarization energies, are sketched. The electron polaron states and the hole polaron states are both Gaussian distributed, as are additional trap states within the bandgap. Here, as an example, one discrete trap level, which can arise from crystal imperfections, is depicted close to the valence band.

bandgap are not attractive for the charge carriers as it costs energy to fill them. Hence, these states can be regarded as repelling centers, where free carriers get scattered.

So far, the model has not included imperfections in the organic crystal. These imperfections can be structural defects, impurity atoms, grain boundaries in polycrystalline films or generally the surface of the crystal. All these imperfections change the polarization environment. Usually, these states show also a Gaussian distribution. They do not have to be centered at the bands, but can also occur deep within the bandgap. If these trap states are located close to the valence band, they are normally considered to be of hole trap character, while those in the vicinity of the conduction band can be regarded as electron traps. Altogether, there are four different kind of traps. Electron traps that are positively charged in its empty states and neutral, if filled with one electron, electron traps that are neutral if empty and negatively charged if filled, hole traps that are negatively charged

if empty and neutral if filled, and finally hole trap states that are neutral if empty and positively charged if filled. It should never be forgotten, that holes are missing electrons, so filling a trap with a hole is physically the same as emptying a trap by an electron release. Nevertheless, traps in the vicinity of the valence band predominantly interact with charges in the valence band, which are holes, and thus can be best described by holes. The same account for trap states in the vicinity of the conduction band, which are usually treated as electron traps.

Charge transport mechanism

In inorganic semiconductor crystals, the electrons in the conduction band move in delocalized states and can be described by plane waves ψ_k [13]

$$\psi_{k\mathbf{r}} = e^{i\mathbf{k}\mathbf{r}} \quad (3.14)$$

where \mathbf{k} is the wave vector and \mathbf{r} is the position in the crystal. The charge transport is limited by scattering processes. Phonon scattering is the main contribution in highly purified inorganic crystals. Thus, the mobility for high temperatures normally decreases with increasing temperature T and is given by [21]

$$\mu \propto T^{-n} \quad (3.15)$$

where n is positive. For scattering with acoustic phonons, n is approximately 1.5.

Whether there is band transport in organic crystals depends on the average scattering time of the charge carriers. If the scattering time is small compared \hbar/W , where \hbar is the Planck constant and W is the band width, the charge carrier does not have a defined wave vector any more. Therefore, the concept of energy bands collapses. For typical bandwidths of $0.1\text{ eV} - 0.5\text{ eV}$, this implies that the scattering time must exceed about 10^{-15} s . Furthermore, the mean free path of a charge carrier must be large compared to the lattice constant to enable band transport. Otherwise the charge carriers can not be described as delocalized states. If these two conditions are not fulfilled, transport is modeled as a local hopping from charge carriers from one molecule to the next molecule. This is often described as a thermally activated process, which is given by

$$\mu = \mu_0 \exp\left(-\frac{E_A}{k_b T}\right). \quad (3.16)$$

Here, μ_0 is the intrinsic mobility at $T = 0$ and E_A is the average activation energy needed to move the charge carrier from one localized state to the next site.

It is very difficult to estimate, if the conditions for band transport are matched for organic materials. The increase of the mobility with decreasing temperature has been found mainly in highly purified organic crystals so far. Band transport is only possible, if the trap density is very low in the organic crystal. This is illustrated in Figure 3.6. Here, Karl et. al. showed, that a trap density of 0.17% leads to thermally activated transport at

room temperature. In polycrystalline organic films, the defect concentration is usually too high to allow for band transport. Therefore, the transport can be often described by the hopping-like transport equation (3.16).

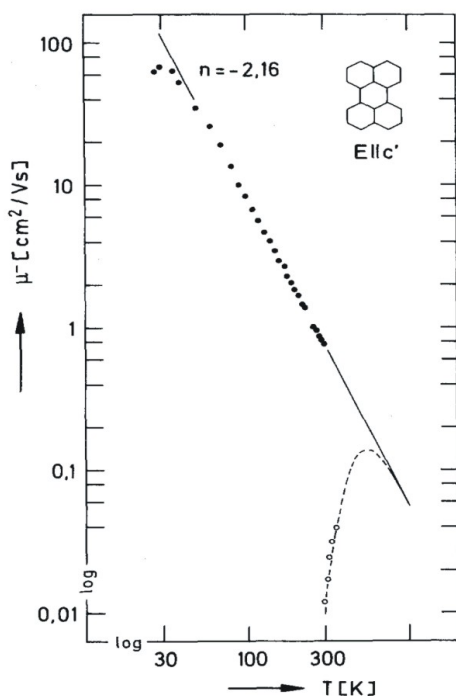


Figure 3.6: Temperature dependence of the electron mobility in a perylene crystal. In the case of a highly purified crystal (filled circles), the mobility increases with decreasing temperature, which is indicative of band transport. In the case of a crystal with a trap density of 0.17%, the mobility decreases with decreasing temperature, which can be explained by a thermally activated hopping transport. Adapted from [22].

3.4 Structure of pentacene

In this PhD-thesis, pentacene was exclusively used as organic semiconductor. The pentacene molecule consists of five fused benzene rings, therefore it belongs to the group of polyacenes, which has already been introduced in section 3.2.1 (see Figure 3.2). It is one of the most investigated organic compounds, since it provides transistors with mobilities, which are among the highest of all organic thin films [23–25]. In the following, some basic structural properties of pentacene thin films are presented.

Organic semiconductors can be either grown in the form of single crystals or in the form of amorphous or polycrystalline thin films. As the growth of pentacene single crystals turned out to be very challenging, crystalline pentacene was used only in a few studies to investigate basic properties of organic crystals [26,27]. Moreover, these crystals are outperformed by other organic single crystals, such as rubrene [28]. Hence, the vast majority of the investigations were conducted on polycrystalline pentacene films. Although thin films have usually lower mobilities than single crystals [24], they are of special interest, since semiconductor applications require mass production techniques, which is impossible using single crystals.

Pentacene thin films can be deposited on a substrate by thermal evaporation in high vacuum (for a more elaborate description see section 4.3). Depending on the substrate, pentacene thin films show varying growth mechanisms. On insulating substrates, they usually grow in ordered layers while on metallic surfaces, the growth is often very rugged. AFM micrographs of an evaporated pentacene thin film with a film thickness of 50 nm , that we have grown, are shown in Figure 3.7.

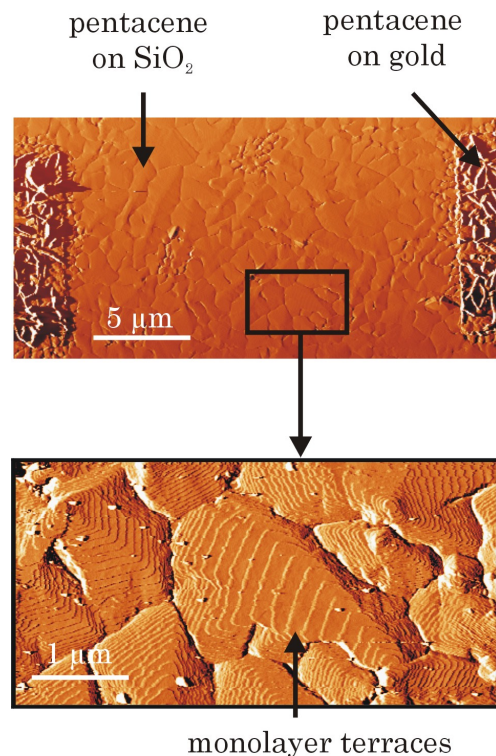


Figure 3.7: AFM amplitude micrographs of a pentacene thin film. On top, the difference between the structure of pentacene on silicon oxide and on gold can be seen. On silicon oxide, pentacene grows in an ordered structure with single grain sizes of up to $3\text{ }\mu\text{m}$. Nevertheless, the grain sizes close to the gold already decreased. On gold, pentacene grows very rugged and less ordered. Below, a separate AFM image of the same pentacene film with a higher resolution is depicted. The terraces of the monolayers of the thin film phase are nicely resolved.

We are able to grow pentacene films with grain sizes of several micrometers. This is especially important for the optical measurements, as the grain size is significantly larger than the diffraction limited size of our illumination spot (see also Figure 7.6). Therefore, the grains can be optically resolved. The grain size strongly depends on the deposition rate, substrate temperature and the vacuum conditions [29]. The initial growth of pentacene on insulators can be described by the diffusion limited aggregation (DLA) model [30]. Incoming molecules diffuse and form nuclei, which subsequently grow [31]. The exact structure of the thin film phase of pentacene was determined in a very sophisticated x-ray analysis by Schiefer et. al. [32] and is depicted in Figure 3.8. The pentacene molecules are orientated upward with a little tilting angle of about 6° of the long molecular axis relatively to the surface normal, which leads to a monolayer spacing of 15.4 \AA . Monolayer terraces can also be seen in the AFM micrograph of Figure 3.7. Moreover, the unit cell of pentacene is triclinic with two translationally invariant molecules, which results in the so called Herringbone Structure. On polycrystalline gold, however, the first monolayer of pentacene molecules is lying flat [33], with the long molecular axis in parallel orientation with respect to the surface. Subsequently incoming pentacene molecules form small grains

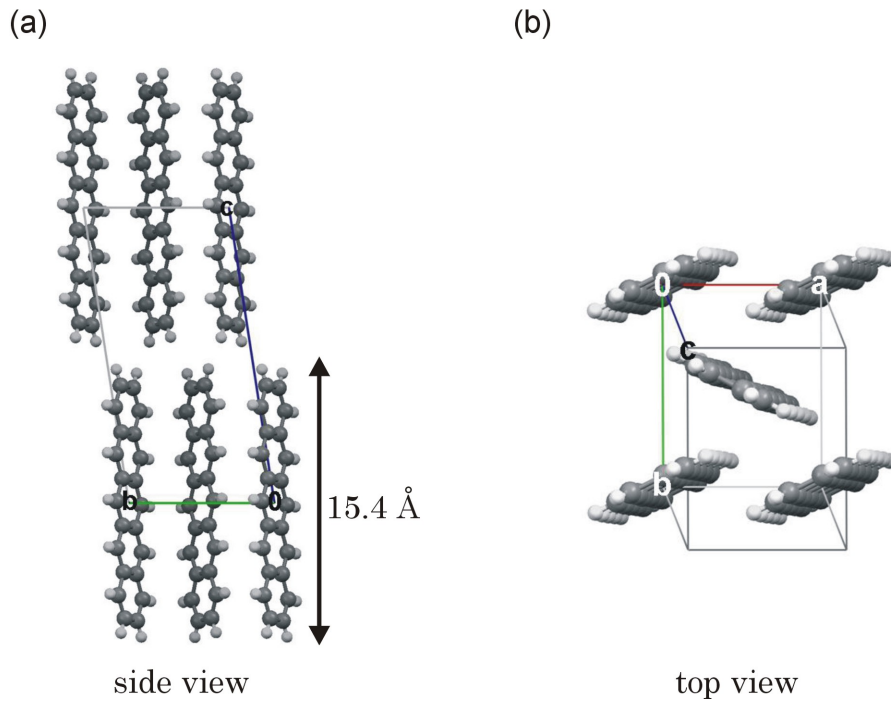


Figure 3.8: Herringbone structure of pentacene (a) in side view and (b) in top view.

on this wetting layer. With increasing film thickness, a pronounced dewetting takes place [34], since the surface energy of the lying phase is larger than the surface energy of the thin film phase [35]. This leads to a very uncontrolled growth mechanism and often results in very rugged and discontinuous films, cf. the AFM image in Figure 3.7. In the vicinity of gold, the growth mechanism on silicon oxide is disturbed, which results in a grain size decrease towards the contact edge. In the case of thermally evaporated gold, the uncontrolled growth mechanism is further pronounced by its high surface roughness.

Chapter 4

Fabrication of pentacene TFTs

This chapter describes the fabrication of our pentacene thin film transistors. A typical sample design is sketched in Figure 4.1. As it was continuously tried to optimize the quality of the transistors during the thesis, it is not possible to describe all tested variations of the single fabrication steps. Instead, the reader can find below a fabrication recipe that we recently used. Major problems, that we have encountered, and significant improvements are explained as well.

4.1 Dielectric

4.1.1 Silicon oxide

In thin film transistors, the accumulation channel is confined to a region of a few nanometers adjacent to the insulator-semiconductor interface (see Figure 2.9). Therefore, the quality of the insulator surface is crucial for the performance of pentacene TFTs. As our transistors were fabricated on a highly n-doped silicon substrate, which served as gate contact, we used thermal silicon oxide as dielectric. It was shown, that the performance of pentacene transistors dramatically decreases with an increasing surface roughness of the SiO_2 dielectric [36]. Thus, sputtered or chemically deposited silicon oxide layers are not suited for pentacene TFTs, as the rms-roughness of these layers, which is typically in the order of a few nanometers, is much too high. The roughness of thermal silicon oxide is determined by the surface of the silicon substrate, as it is not deposited on top of the silicon substrate but grown into it. Wafers with a 150 nm-thick thermal silicon oxide layers on top of highly arsenic doped silicon substrates could be purchased from the supplier CrysTec. Nevertheless, the quality of the purchased oxide was not ideal. Therefore, we started to oxidize bare samples, that were purchased from CrysTec as well, on our own using an RTP furnace. The roughness of the silicon oxide is determined by the roughness of the polished (100)-surface of the silicon substrate. For the purchased and the self-made oxide similar rms-roughnesses of about 0.3 nm were achieved. An advantage of producing a self-made silicon oxide is the tunability of its thickness, that was measured by ellipsometry. The

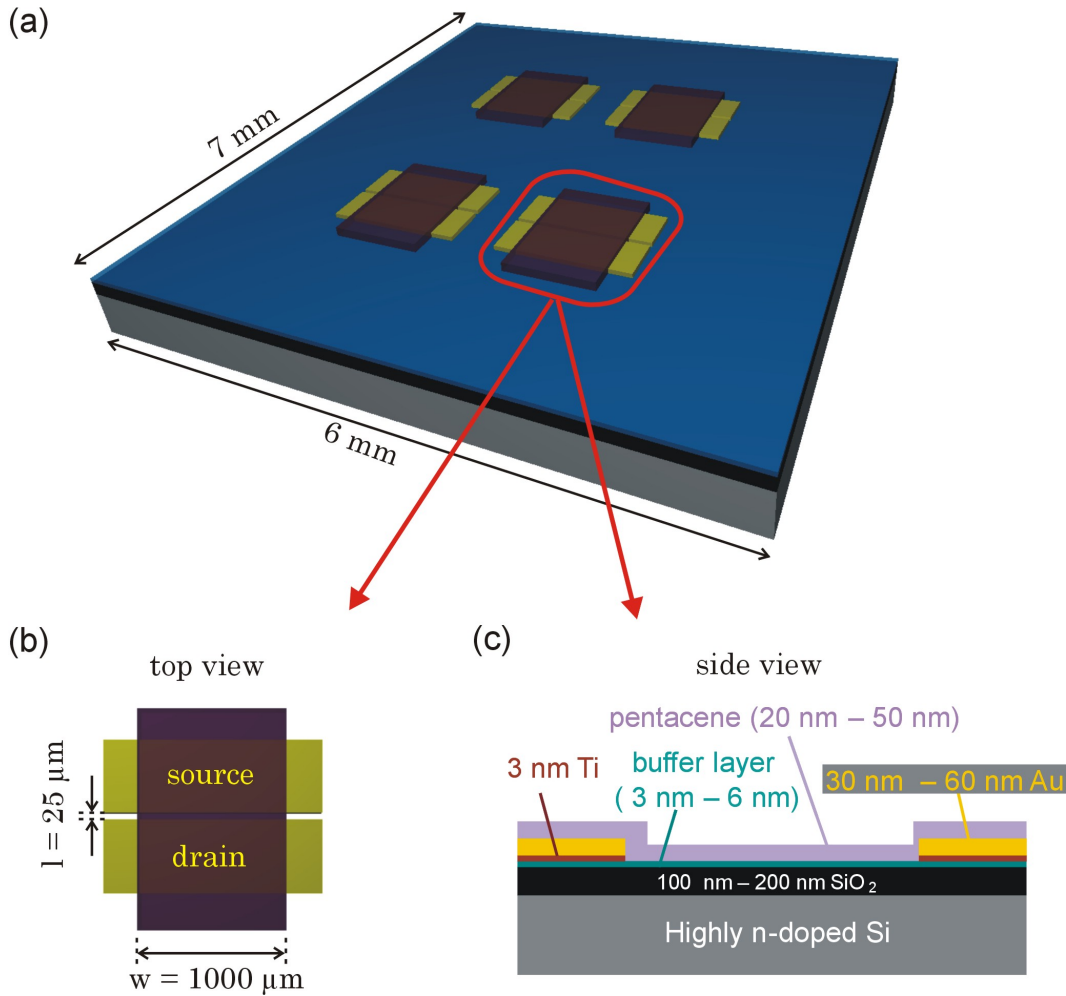


Figure 4.1: Design of the bottom-contact pentacene thin film transistors. (a) Overview of a sample including four transistors on a chip, that is cleaved to a size of 7 mm x 6 mm. (b) Top view of a single TFT with the channel length defined by the spacing of the two gold electrodes and the channel width which results from the extension of the pentacene layer. (c) Side view of a typically used bottom-contact transistor configuration where a polymer buffer layer was used.

thickness should not be below 100 nm, as it turned out, that the insulator layer was not dense enough for the gate voltages, that we typically used for accumulation. In order to calculate the mobility with equation (2.39) or (2.41) from I-V measurements, one has to know the area capacitance C_i of the silicon oxide. We measured C_i with an EG & G 7260 Lock-In Amplifier and obtained for a 150 nm-thick oxide layer a value of $2.2 \cdot 10^{-8} \text{ F/cm}^2$. This result is in good agreement with the theoretical value, that can be calculated using the relationship $C_i = \epsilon_i/d_i$, where $\epsilon_i = 3.9 \epsilon_0$ for silicon oxide and d_i is the thickness of the insulator. This formula was thus used to calculate the capacitance for the various oxide thicknesses of our transistors.

The oxidized wafers were first cut into pieces with a diamond tip to a final size of about 7 mm x 6 mm. Then, the samples were cleaned by a standard procedure with different steps in the following order:

- samples were put in a bath of remover 1165 for about 10 minutes
- samples were further put in an ultrasonic bath in acetone for about 5 minutes, followed by a short bath in isopropanole
- if under the microscope residua on the samples could be seen, the samples were carefully cleaned mechanically by acetone soaked photopaper, that was wrapped around a tweezer (important: the acetone must not be vaporized completely at any time, before the samples were rinsed in isopropanole in order to avoid residua)
- samples were dried by blowing them with nitrogen gas
- optionally, the samples were put in an oxygen plasma, using the Labash for 1 minute at a power of 50 W and a pressure of 2 torr

4.1.2 Polymer buffer layer

In order to improve the transport characteristics of our samples, we modified our insulator surface by adding an extra layer. First, we tried to functionalize the silicon oxide surface by a self assembled monolayer of octadecyltrichlorsilane (OTS), as it is done by lots of other groups [37–39]. Unfortunately, we could not improve our transistors by this method. Therefore, we decided to put a very thin polymeric buffer layer on top of the silicon oxide. We have used two different polymers with similar success, namely cyclic olefin copolymer (COC) of the supplier Ticoma, which is also called Topas, or polystyrene (PS). Their chemical structures are depicted in Figure 4.2.

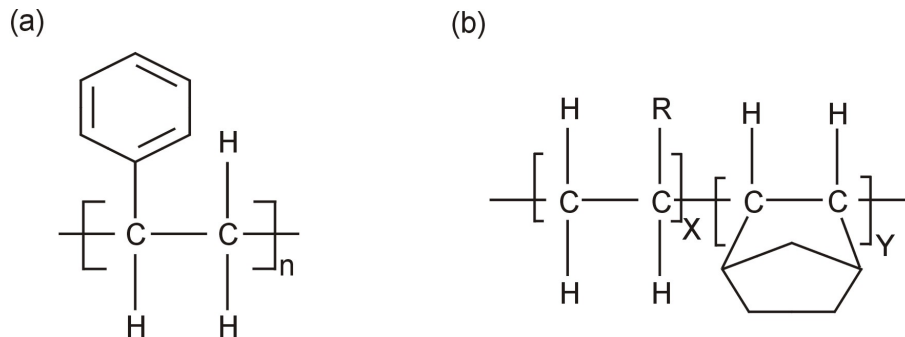


Figure 4.2: Chemical structure of the two polymers that were used as buffer layers. In (a) cyclic olefin copolymer (brand name Topas of the company Ticoma) and in (b) polystyrene are depicted, respectively.

The polymer, either Topas or polystyrene, was first dissolved with a mass concentration of 0.25 % in toluene. Afterwards, the samples were spincoated for 30 seconds at a spinning

rate of 6000 rpm. Subsequently, the samples were heated for 1 minute at a temperature of 100°C on a hotplate. The thickness of this layer was determined using atomic force microscopy and x-ray reflectometry. Both methods agreed that the polymer buffer layer was 6 nm thick and the rms-roughness of the silicon oxide surface was not significantly altered by the additional coating. As this layer is much thinner than the silicon oxide, the capacitance of the insulator of the transistors is only slightly changed and can be neglected in the calculation for the mobility.

4.2 Contacts

We have mostly produced bottom-contact TFTs (see Figure 2.11(a)). Hence, the next step in the fabrication process is the evaporation of the source and drain contacts. A general advantage of the bottom-contact configuration is the possibility to use optical lithography to define the transistor channels, as in top-contact configuration the pentacene layer would be destroyed by the solvents, that are needed for this method. Unfortunately, it turned out, that optical lithography could not be employed if the samples were covered by a buffer layer of Topas or polystyrene, as these polymer coatings were also damaged by the solvents, that are commonly used for the photoresist lift-off. It was tried to use isopropanole instead of acetone for the lift-off of the photo resist, which seemed not to destroy a Topas coating. Although the samples were sonicated for one hour, photoresist residua could not be removed completely with this solvent. Finally, we decided to evaporate our contacts using shadow masks instead. We usually employed masks, that created four transistors on one piece of wafer. First, we used a computer controlled drilling machine to cut quadratic holes with a side length of typically 1.5 mm into an aluminum blank. Then, we bridged these block-outs in the middle with a $25\text{ }\mu\text{m}$ -wide gold wire, that was fixed at the blank with a two component epoxy adhesive. This shadow masks were put on top of the prepared samples and locked together into the metal evaporation chamber. A 3 nm -thick adhesion layer of titanium at a rate of about 0.3 \AA/s was first evaporated before a $40\text{ nm} - 60\text{ nm}$ gold layer was deposited at a rate of typically 0.5 \AA/s to finish the source and drain contacts. The rms-roughness of the evaporated gold is a few nanometers and hence about one magnitude higher than the rms-roughness of the insulator. Due to the bond wire in the shadow mask, the spacing of two adjacent contacts was about 25 nm , which defines the channel length of the transistor.

At the end of the thesis, we also implemented the top-contact design (see Figure 2.11(b)). In this case, the contacts were deposited as described above, but after the deposition of pentacene. Some groups also reported, that palladium contacts can improve the performance of pentacene TFTs [40,41]. Therefore, we also produced some transistors using this metal for the contacts, but as we could not observe any improvements, we did not pursued fabrication of transistors with this material.

4.3 Pentacene deposition

It is very important, that the samples are as clean as possible, when they are mounted into the pentacene evaporation chamber. Hence, the samples should be either stored in vacuum or mounted directly after the contact fabrication step. All samples, except those that were intended for the thickness dependent in-situ measurements, were transferred into our relatively small and mobile growth chamber, that is depicted in Figure 4.3 (for the thickness dependent in-situ measurements, we used a different MBE chamber, which is described in section 6.2.1).

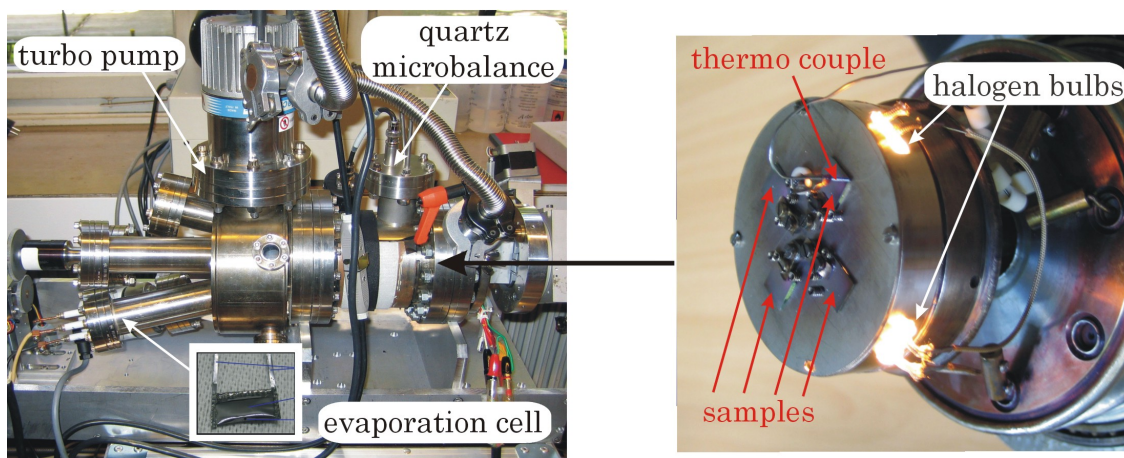


Figure 4.3: Photographs of UHV pentacene evaporation chamber. On the left, the complete chamber is shown. The inset depicts our self made evaporation cell consisting of a tantalum bag. On the right, the sample stage, which is loaded with four different samples, is depicted.

This UHV chamber could be loaded with four different samples as can be seen on the right of Figure 4.3. The chamber has a base pressure of about 10^{-8} mbar. The samples could be heated using halogen bulbs to temperatures above $200^{\circ}C$. As evaporation cell we used a self-made tantalum bag, which was filled with pentacene and could be heated with an electric current. This simple design turned out to be superior to a more sophisticated cell, which was constructed in the form of a tube made of aluminum, that was heated by a halogen bulb. However, the aluminum was not pure, i.e. other components, such as zinc, caused contamination if heated up to temperatures, that are used for pentacene evaporation.

We have purchased pentacene from Sigma Aldrich. In the beginning of the thesis, it was further purified by Jens Pflaum of Universität Stuttgart using gradual zone sublimation. Later, Sigma Aldrich offered triple sublimed pentacene, so that we could use it as purchased. Nevertheless, we think that the quality of the purchased pentacene was not constantly the same, as we had problems to produce transistors with high mobilities for some periods of time.

The whole evaporation process of pentacene could be controlled by a Labview program.

A Labview screenshot is depicted in Figure 4.4. This allowed us to monitor the chamber pressure, the sample temperature, the sample heating power, the deposition thickness, the deposition rate and the evaporation cell current during deposition.

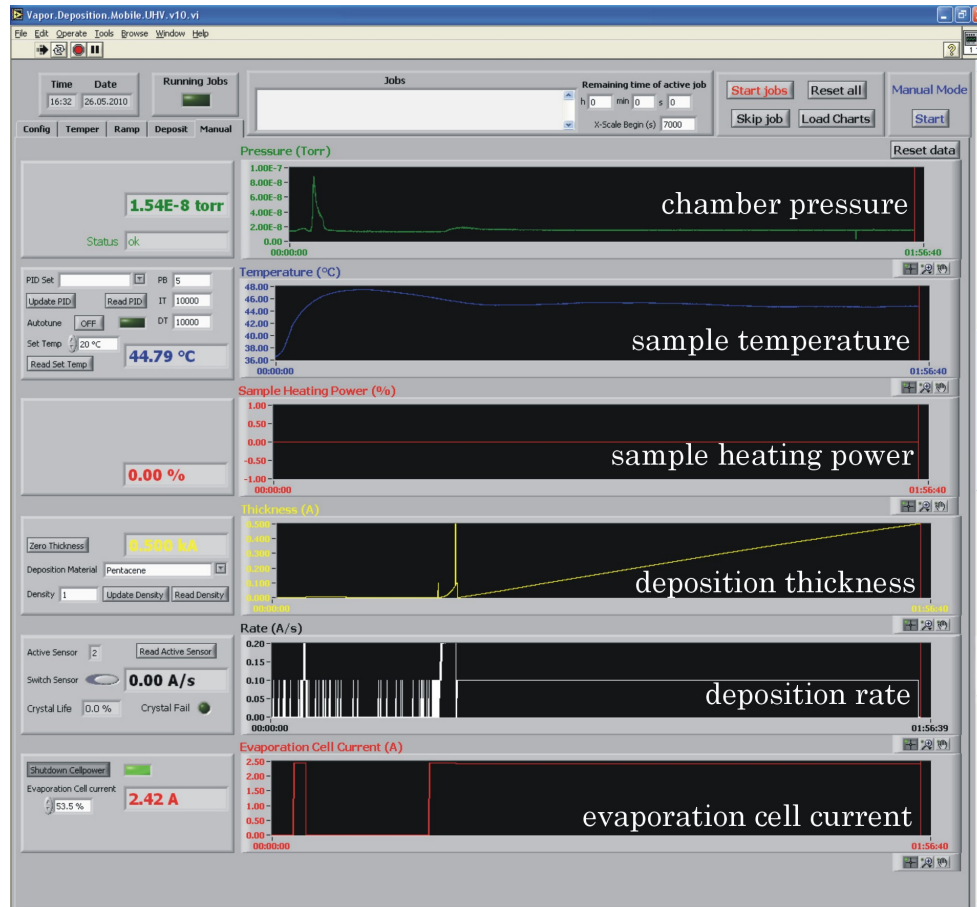


Figure 4.4: Screenshot of the self-made Labview program that was used for pentacene evaporation. Chamber pressure, sample temperature, sample heating power, deposition thickness, deposition rate, and evaporation cell current could be monitored and controlled during deposition.

After mounting the samples, the chamber was immediately evacuated. Once the pressure decreased below a value of 10^{-6} mbar, the samples were annealed as a last cleaning step. If no polymer buffer layer was used, the samples could be heated up to 200°C , but if Topas or polystyrene was used, the samples should not be exposed to temperatures exceeding 100°C , as the polymer layer might be damaged. For the pentacene evaporation, the pressure should be below 10^{-7} mbar. We have usually deposited a 48 nm -thick pentacene layer at an evaporation rate of about 0.1 \AA/s at a sample temperature between room temperature and 50°C .

After the deposition, the samples were withdrawn from the chamber and glued into chip

carriers with conductive silver paste. Finally the samples were electrically connected using a wedge bonder with aluminum wires. Gold wires could not be used due to the elevated temperatures, that are needed in the case of gold wires, since the polymer buffer layer melts beneath the contact and the wire could thus not stick to the gold pad.

Chapter 5

Electronic properties of pentacene TFTs

In this chapter, the basic electronic characteristics of pentacene TFTs, that we have fabricated as reported in chapter 4, are described.

5.1 Experimental setup

The experimental setup, that we have used for basic electronic measurements is depicted in Figure 5.1. The more sophisticated setups for the spatially resolved measurements are described in section 6.2.1 (in-situ measurements) and 7.2 (optoelectronic measurements), respectively.

The bonded samples were mounted into a sample holder in the measurement chamber, that could be evacuated down to a pressure of about 10^{-6} *mbar*. In this chamber, the samples were protected from light, therefore we also used it to perform measurements under ambient but dark conditions. The source-drain voltage and the gate voltage were applied by two Yokogawa 7651 DC sources at the drain and gate contact, respectively. It turned out, that for relatively thin dielectrics with a thickness of about 100 nm , the gate voltage should not exceed values of 20 V . Otherwise, the insulating layer could be damaged or destroyed. In contrast, for a dielectric thickness of 150 nm , we did not encounter these problems for voltages of up to -32 V , which is the limit of the Yokogawa source. The source-drain current was measured at the source-electrode. We used a Femto DLPCA-200 I-V converter with an amplification factor of $10^4 - 10^6$ to transform the signal into a DC-voltage up to a range, that could be determined by a HP 34410 multimeter with high precision. The voltage sources and the multimeter were controlled and read out by a Labview program, that communicated with the devices using GPIB interfaces.

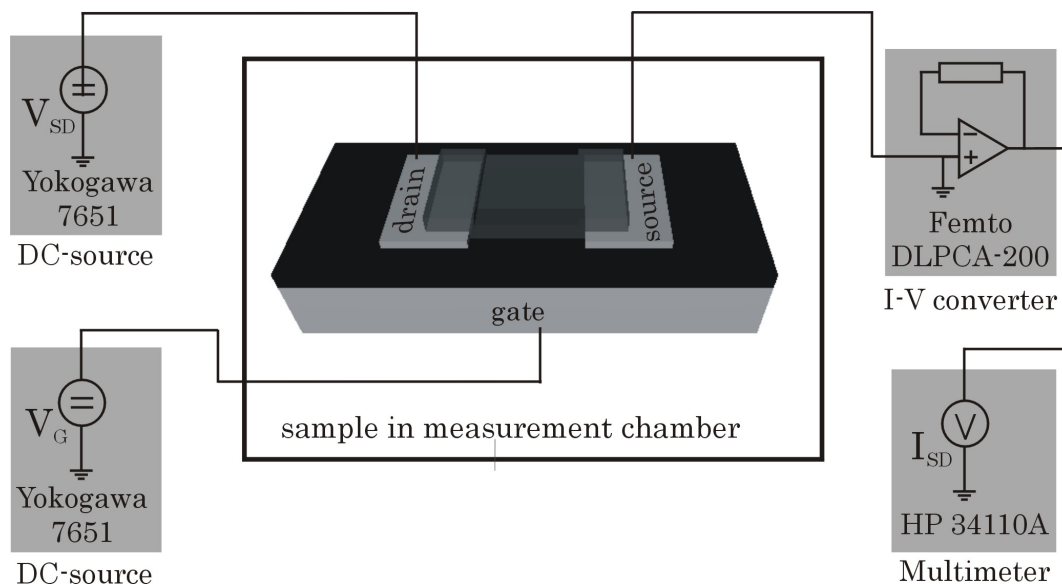


Figure 5.1: Scheme of the setup for the electronic measurements. The measurement chamber could be evacuated to about 10^{-6} mbar. The source-drain voltage V_{SD} and the gate voltage V_G were applied by two Yokogawa 7651 DC sources, that were connected to drain and gate, respectively. The source-drain current I_{SD} was measured by a combination of a Femto DLPCA-200 I-V converter and a HP 34410A multimeter, that were connected to source.

5.2 Basic transport characteristics

In this section, the transport characteristics of a typical sample are presented. The sample, that is presented in the following, was fabricated as shown in Figure 4.1 with a polystyrene buffer layer.

5.2.1 Conductance measurements

Using the setup described above, we have measured the conductance of our pentacene thin film transistors. Therefore, the source-drain voltage V_{SD} was swept from 0 V to negative voltages up to -32 V for different constant gate voltages V_G and the source-drain current I_{SD} was measured. Representative conductance curves of a bottom-contact pentacene transistor with a polystyrene buffer layer for $V_G = -10$ V, $V_G = -20$ V, and $V_G = -30$ V are depicted in Figure 5.2. The typical behavior of a hole-conducting unipolar TFT, that was sketched in Figure 2.13, could be observed. For low source-drain voltages, I_{SD} increased linearly with respect to V_{SD} , while for high source-drain voltages I_{SD} saturated.

The ohmic behavior in the linear regime could be used to calculate the resistance of the device in dependence on the gate voltage. Using Ohm's law

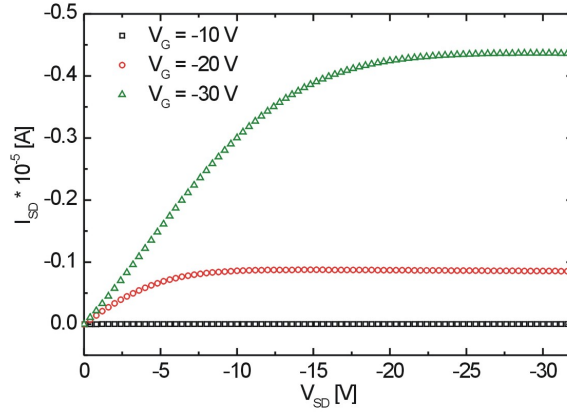


Figure 5.2: Conductance curves for a bottom contact pentacene TFT. The source-drain current is plotted against the source-drain voltages for gate voltages of $V_G = -10 V$, $V_G = -20 V$, and $V_G = -30 V$.

$$R = \frac{V_{SD}}{I_{SD}} \quad (5.1)$$

one obtains $5.9 \cdot 10^6 \Omega$ and $3.4 \cdot 10^6 \Omega$ for $V_G = -20 V$ and $V_G = -30 V$, respectively.

With increasing negative gate voltage, the saturation regime set in for higher source-drain voltage magnitudes. This is due to the condition $|V_{SD}| > |V_G - V_T|$, which must be matched for the saturation regime (compare section 2.3.2). As the threshold voltage was very close to $-10 V$, there was only a very small current for $V_G = -10 V$.

5.2.2 Transconductance measurements

The mobility of our TFTs was extracted using transconductance measurements, as described in section 2.3.3. The gate voltage was swept for different constant source-drain voltages while recording the source-drain current continuously. In order to calculate the mobility in the linear regime, relatively small source-drain voltages are needed to fulfill the linear regime condition ($|V_{SD}| < |V_G - V_T|$) within the gate voltage range of the sweep. Instead, for an accurate determination in the saturation regime, relatively large source-drain voltages should be applied in order to have a sufficiently large gate voltage range, where the saturation regime condition $|V_{SD}| > |V_G - V_T|$ is satisfied.

In Figure 5.3(a), the transconductance curves for $V_{SD} = -3 V$, $V_{SD} = -5 V$, and $V_{SD} = -10 V$ are shown. The linear mobility was extracted from the slope of the linear fits using equation (2.39). In this case, the linear mobility was $0.04 \text{ cm}^2/(\text{Vs})$ for all three different source-drain voltages.

In order to extract the saturation mobility, $|\sqrt{I_{SD}}|$ was plotted against V_G for $V_{SD} =$

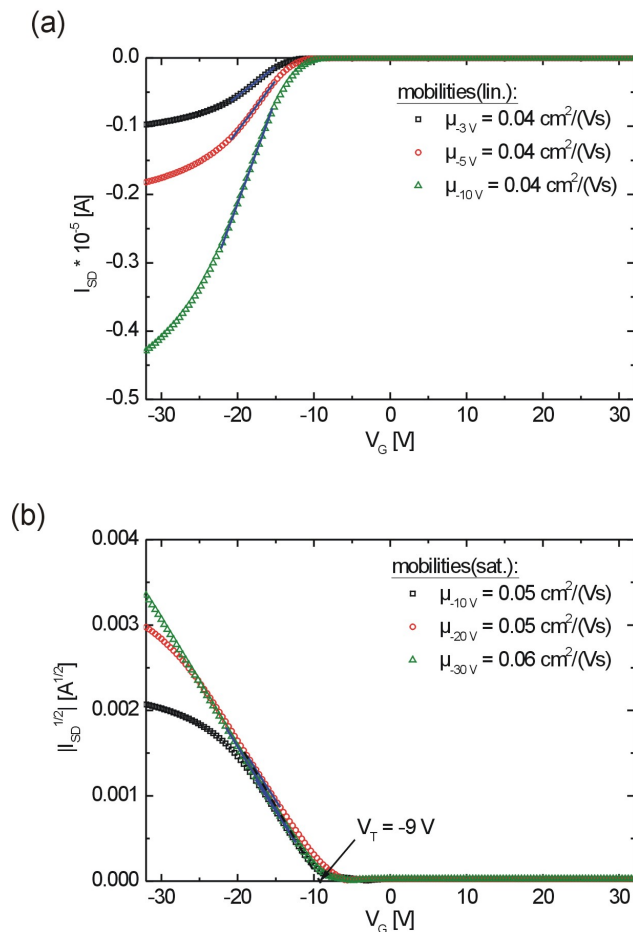


Figure 5.3: Transconductance curves for a bottom contact pentacene TFT. (a) Plot of the source-drain current I_{SD} vs. the gate voltage V_G for source-drain voltages of $V_{SD} = -3$ V, $V_{SD} = -5$ V, and $V_{SD} = -10$ V in order to extract the linear mobility using equation (2.39). (b) Plot of the $\sqrt{|I_{SD}|}$ vs. for source-drain voltages of $V_{SD} = -10$ V, $V_{SD} = -20$ V, and $V_{SD} = -30$ V in order to extract the saturation mobility using equation (2.41) and the threshold voltage.

-10 V, $V_{SD} = -20$ V, and $V_{SD} = -30$ V, as it is shown in Figure 5.3(b). Using equation (2.41), saturation mobilities of 0.05 $cm^2/(Vs)$, 0.05 $cm^2/(Vs)$, and 0.06 $cm^2/(Vs)$ could be extracted for $V_{SD} = -10$ V, $V_{SD} = -20$ V, and $V_{SD} = -30$ V, respectively. Furthermore, the threshold voltage can be deduced from the intersection of the linear fit in the saturation regime with the abscissa. In the case of the sample in Figure 5.3, the threshold voltage was about $V_T = -9$ V.

A semilogarithmic plot of the source-drain current against the gate voltage for $V_{SD} = -20$ V is presented in Figure 5.4. The subthreshold slope of the sample could be determined to be $S = 1.2$ V/decade and the on-off ratio to be about 10^4 . The on-off ratio is probably limited

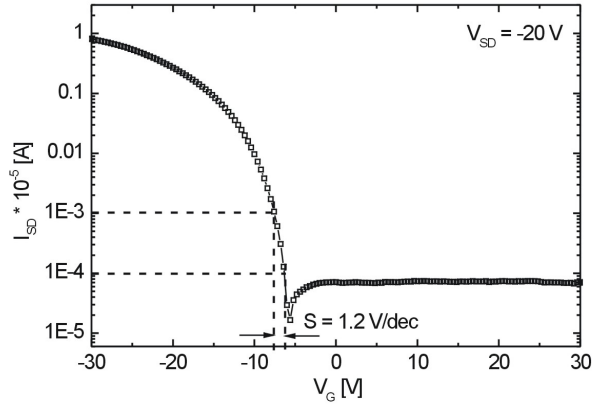


Figure 5.4: Semilogarithmic plot of the source-drain current vs. the gate voltage of a bottom contact pentacene TFT in order to determine the subthreshold slope for a source-drain voltage of $V_{SD} = -20 V$.

by the measurement setup, i.e. the offset current. The influence of the offset current effect can be seen in the logarithmic representation of Figure 5.4. Here, the source-drain current dips before the transistor turns on, which suggests a little positive offset current in the order of $10^{-9} A$, that is compensated in this regime by the onset of the negative transistor source-drain current.

It is possible to estimate the accumulated hole density per unit area N_h with the extracted parameters above. The conductivity σ and the mobility μ are linked by the relationship $\sigma = ne\mu$, with n being the mobile volume charge density and e being the elementary charge. Using $n = N_h/d$, $\sigma = 1/\rho$, and $\rho = (W \cdot d/L) \cdot R$, one finally obtains for the area hole density

$$N_h = \frac{L}{e\mu WR} \quad (5.2)$$

where ρ is the resistivity, R is the resistance and L , W , and d are the channel length, channel width, and the thickness of the accumulation channel, respectively. Inserting $L = 25 \mu m$, $W = 1000 \mu m$, $\mu = 0.04 cm^2/(Vs)$, which was determined from the transconductance curves in the linear regime, and $R = 5.9 \cdot 10^6 \Omega$ and $R = 3.4 \cdot 10^6 \Omega$, which were calculated in section 5.2.1 for $V_G = -20 V$ and $V_G = -30 V$, hole densities of $N_h(V_G = -20 V) = 6.6 \cdot 10^{11} cm^{-2}$ and $N_h(V_G = -30 V) = 1.1 \cdot 10^{12} cm^{-2}$ were determined.

5.3 Deviations from ideal behavior

5.3.1 Hysteresis

In an ideal TFT device, the current should only depend on the voltages, that are currently applied. However, in real devices the source-drain current also depends on the biases, that have been applied before. In order to investigate this, the transconductance was measured by conducting a gate voltage sweep from $V_G = +32\text{ V}$ to $V_G = -32\text{ V}$ and a subsequently gate voltage sweep back from $V_G = -32\text{ V}$ to $V_G = +32\text{ V}$, as it is presented in Figure 5.5. For both directions, the source-drain voltage was held at $V_{SD} = -20\text{ V}$ at a gate voltage sweeping rate of 0.4 V/s without interruption between the forward and backward sweep. In our transistors, we always observed a larger current for the forward sweep, though the margin between the two sweeps depended highly on the insulator of our transistors. In the case of a TFT without a polymer buffer layer on top of the silicon oxide, this hysteresis effect is much larger than for a TFT without such an additional coating. In order to quantize the hysteresis, one can use the difference of the threshold voltages, which is

$$V_{Hys} = \Delta V_T = V_T(\text{forward}) - V_T(\text{backward}) \quad (5.3)$$

where $V_T(\text{forward})$ and $V_T(\text{backward})$ are the threshold voltages determined from the gate sweeps from a positive voltage to a negative voltage and vice versa, respectively. Using the transconductance curves of Figure 5.5, the hysteresis voltage in the case of a transistor without polymer buffer layer was about 13 V , while for the transistor with a Topas buffer layer it was much smaller with a value of about 1 V .

The reason for this behavior is typically considered to arise from shallow trap states in the band gap of pentacene [42]. These trap states can be located at the semiconductor-insulator interface, within the bulk of the pentacene or at the surface of the semiconductor, which is explained in more detail in section 6.4. The traps, that cause hysteresis, are called shallow, as they can be filled and emptied, depending on the gate voltage and on time. In the case of traps, that are closely above the valence band, the traps can be regarded as hole traps, that are filled for negative gate voltages, as the energy of the trap level can be lifted above the Fermi level. If the gate voltages is switched to positive values, the trap level gets below the Fermi level again, leading to detrapping of the hole. In the case of traps, that are closely below the conduction band, the traps can be considered as electron traps that are emptied for a negative gate voltage and filled for a positive one. Whether the traps are electron-like or hole-like can not be distinguished by the hysteresis measurements, as the effect of a hole trap, that gets filled, is equivalent to the effect of an electron trap, that gets emptied. It is important to understand, that trapping an additional hole, which is the same as releasing an additional electron, results in a TFT accumulation channel which is short of one additional free hole.

In order to estimate the density of the shallow traps, one can neglect the voltage drop in the semiconductor allowing to calculate the areal density of shallow trapped charges N_{st} using

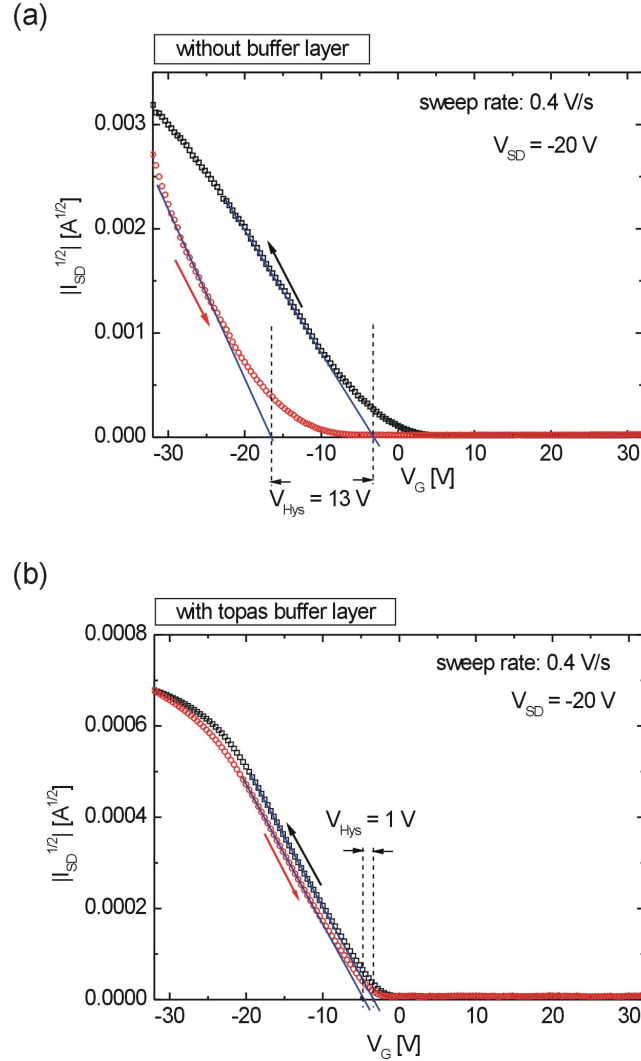


Figure 5.5: Hysteresis of transconductance measurements showing a gate voltage sweep from $V_G = +32$ V to $V_G = -32$ V and a subsequent gate voltage sweep from $V_G = -32$ V to $V_G = +32$ V of two different pentacene TFTs. In (a) the hysteresis of a TFT without a polymeric buffer layer is shown, while in (b) the hysteresis of a TFT with a topas buffer layer is presented. In both cases, the source-drain voltage was held at $V_{SD} = -20$ V and V_G was swept at a rate of 0.4 V/s.

$$N_{st} = \frac{Q_t}{e} = \frac{C_i}{e} \cdot V_{Hys} \quad (5.4)$$

where Q_t is the area charge density, e is the elementary charge and C_i is the area capacitance of the insulator [43]. This equation implies, that the trapped charges consume free charges. The trapped charges can be compensated by accumulating extra charges capacitively by

an appropriate additional gate voltage, which corresponds to V_{Hys} .

Using the extracted V_{Hys} from Figure 5.5 and equation (5.4) gives a shallow trap density of $1.8 \cdot 10^{12} \text{ cm}^{-2}$ for the transistor without buffer layer and $1.4 \cdot 10^{11} \text{ cm}^{-2}$ for the transistor with the Topas buffer layer. In the case of the transistor without buffer layer, this is in the same order of magnitude as the density of free charge carriers at a gate voltage between $V_G = -20 \text{ V}$ and $V_G = -30 \text{ V}$, while for the transistor with the Topas buffer layer it is one order of magnitude below.

The trap states can have different origins. As it was explained in section 3.3.2, the energy of the electronic states in an organic crystal depends on the polarization energy, which is altered in the material by varying distances of lattice sites in the crystal or by impurities. In order to obtain the density of dislocation, which can be responsible for distance variations of adjacent lattice sites, x-ray studies were performed on pentacene thin films by Nickel et al. [44]. The dislocation density per unit area estimated from diffuse scattering is about $2 \cdot 10^{11} \text{ cm}^{-2}$. This value is in the same range as the shallow trap density of $2 \cdot 10^{11} \text{ cm}^{-2}$ for the TFT with the Topas buffer layer. However, structural defects alone can not explain the much larger hysteresis of $1.8 \cdot 10^{12} \text{ cm}^{-2}$ for the TFT without buffer layer. Most likely, the silicon oxide-pentacene interface must play a crucial role in these devices. It is known, that the silicon oxide surface is passivated by hydroxy groups. These hydroxy groups are known as electron acceptors, which can cause trap states. Moreover, this surface is more hydrophilic than the Topas surface leading to an increased absorption of water molecules at the insulator-pentacene interface. Gu et. al. argued, that these water molecules cause electron trapping for positive biasing [45]. For negative gate voltages however, these electron traps are emptied, resulting in a decay of holes, which finally leads to the observed hysteresis.

Whatever the microscopic origin for the large hysteresis is, we could show, that a polymer buffer layer reduces hysteresis dramatically and thus enables much more stable transistor operation for a constant biasing. This is essential for the spatially resolved measurements, that are presented in chapter 7. These measurements are long time experiments, that usually last at least a few minutes, in some cases even hours.

5.3.2 Threshold voltage shift

We commonly measured our pentacene TFTs using exactly the same measurement scheme consisting of twelve different gate voltage and source-drain voltage sweeps. The first and the last measurement were always a transconductance measurement at $V_{SD} = -20 \text{ V}$ at a gate voltage sweeping rate of 0.4 V/s . These two measurements, that were performed at a TFT with a polystyrene buffer layer, are presented in Figure 5.6, where the gate voltage was swept from positive to negative in both cases.

It is clearly visible, that the threshold voltage of the transistor shifted during operation to a more negative value. For further subsequently performed measurements, the threshold voltage is only altered a little bit and remains quite stable. This behavior could be observed in all our transistors. Moreover, the magnitude of this shift was quite similar for TFTs with a polymer buffer layer and those with bare silicon oxide as gate dielectric.

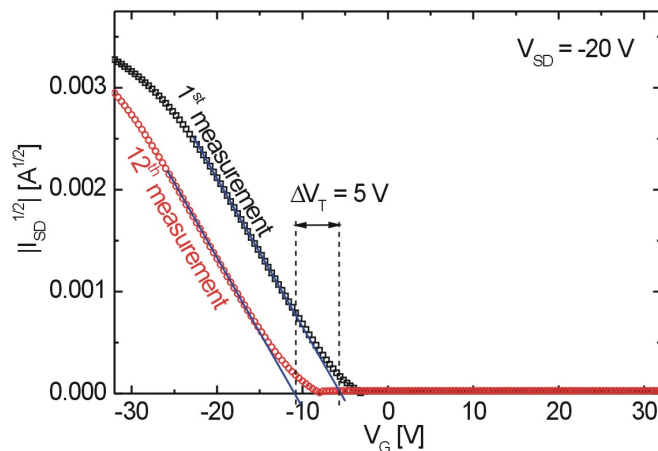


Figure 5.6: Threshold shift of a pentacene TFT. Compared are the transconductance curves of the same transistor with $V_{SD} = -20\text{ V}$ and sweeping rates of 0.4 V/s . The black curve is the first measurement, that was conducted on the transistor, while the red curve was recorded after a cycle of eleven measurements.

We think that the threshold voltage is also generated by traps, as it is the case for the hysteresis. Unlike the hysteresis, the effect is not reversible, thus the traps that cause the threshold voltage shift have to be deep rather than shallow. Since the shift is independent of the insulator surface, we think that the shift is mainly due to traps in the bulk of the pentacene thin film, probably caused by defects and dislocations, as it was discussed for the hysteresis. In order to estimate the density of deep traps N_{dt} , similar to equation (5.4), we use the relationship

$$N_{dt} = \frac{Q_t}{q} = \frac{C_i}{q} \cdot \Delta V_T \quad (5.5)$$

where ΔV_T is the difference of the threshold voltage of the first and twelfth measurement. In Figure 5.6, $\Delta V_T = 5\text{ V}$ which, using equation (5.5), corresponds to a deep trap density of $N_{dt} = 7.0 \cdot 10^{11}\text{ cm}^{-2}$. This value is similar to the density of the shallow trap states, that was determined by the hysteresis.

5.3.3 Nonohmic contact

In section 2.3, the equations of the transport in a TFT are derived assuming a perfect contact between the semiconductor and the source and drain contacts. Furthermore, it was explained in section 2.1, that in order to form an ohmic contact between a metal and a p-type semiconductor as pentacene, the work function of the contacts should be as close as possible to the valence band energy of the semiconductor. Since the work function of gold

is about 5 eV (see table 2.1) and the valence band of pentacene was also determined to be at about 5.1 eV using ultraviolet photoemission spectroscopy (UPS) [46], one can generally expect these two materials to form an ohmic contact. A closer look at the conductance curves of our transistors reveals that there is often a nonlinear increase of the source-drain current for small source-drain voltages. Especially for transistors, where optical lithography was used, we often observed a high deviation from an ideally linear increase of I_{SD} , as it can be seen in Figure 5.7.

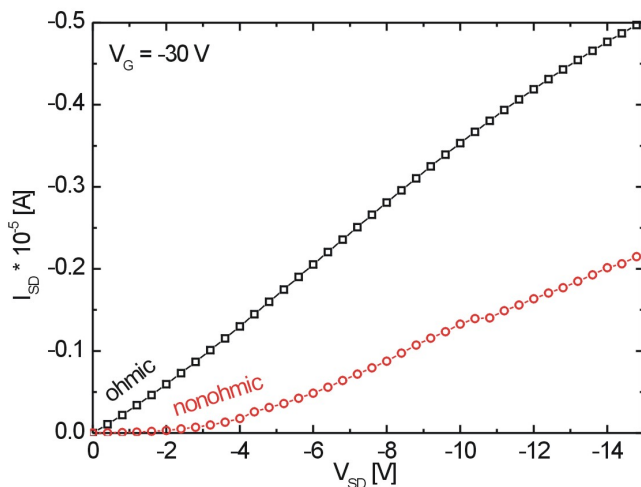


Figure 5.7: Contact resistance of a pentacene TFT. The source-drain current is plotted against the source-drain voltage for a constant gate voltage of $V_G = -30\text{ V}$ for a transistor with contacts, defined by using a shadow mask (black squares) and for a TFT with contacts, defined by using optical lithography (red circles). The TFT with optically defined contacts shows a much higher deviation from an ideal ohmic current increase.

There are several possible reasons for the deviations from ohmic contact behavior. It might be possible, that the contacts are not completely free of solvent residua arising from the lithography process. It is well known, that little contaminations can already change the work function of gold dramatically [47]. Furthermore, it was described in section 3.4, that the pentacene growth is disturbed close to the contacts, resulting in smaller grains adjacent to the electrodes (see Figure 3.7). This structural perturbation can also lead to the formation of bad contacts.

In the literature, there are lots of investigation of the contact resistances in organic thin film transistors. The easiest approach is to fabricate transistors of various channel length and to determine their overall resistance [40, 41, 48, 49]. The contact resistance can be interpolated by a plot of the resistance vs. the channel length. The disadvantage of this method is, that organic TFTs usually show some variations from sample to sample. Moreover, it is not possible to distinguish the contact resistance at source and drain. A more elegant way

to investigate contact resistances is to employ four point measurements, where additional electrodes within the channel measure the potential [50, 51]. This method enables to determine the contact resistances at source and drain separately, but it can only be used in the linear regime of the transistor. The most sophisticated technology to visualize contact barriers is probably to map the potential drop within the transistor channel by Kelvin probe force microscopy (KFM) measurements [52–54].

Most of these investigations on contacts agree, that the contact resistances play a crucial role in the performance of organic TFTs. Therefore the mobilities, that are calculated by equation (2.39) and (2.41), can be considered to be underestimated, as they do not include the reduction of I_{SD} that is caused by the contact resistances. Usually, the injection from holes into the pentacene film is considered to be the bottle neck of charge transport. This is in agreement with the picture of the Schottky diode, as it is depicted in Figure 2.2, because the injection of holes corresponds to the backward biasing direction, while for the hole extraction at drain the diode is biased in forward direction. Especially Puntebeklar et. al. [52] and Gundlach et. al. [40] have employed comprehensive analysis of contact barriers at pentacene TFTs. They could show, that the contact resistances are much higher for bottom contact devices compared to their top contact counterparts. They also attributed the high potential drops at the bottom contacts to the deteriorated structure adjacent to the electrodes, which is not the case for the top contacts, as they are deposited after the pentacene film had already been grown. It was also discussed, that gold particles can penetrate into the pentacene film, thus forming a good ohmic contact to the channel of the pentacene film, which is located at the dielectric interface. In the end of this PhD-thesis we have also fabricated top contact pentacene TFTs, and indeed these devices always showed a linear increase of the I_{SD} for low V_{SD} and comparatively high mobilities in the range of $0.1 \text{ cm}^2/(\text{Vs})$. Nevertheless, even if the conductance curves show ohmic behavior in the linear regime, this does not necessarily mean, that the contact resistance can be neglected. In summary, it is important to remember that contacts play a significant role in pentacene transistors, especially hole injection into the pentacene film seems to be a bottle neck in these devices.

5.4 Simulation of basic electronic circuits

During the PhD thesis, we had a collaboration with Christoph Erlen, who performed drift-diffusion simulations in the group of Prof. Dr. Paolo Lugli from the Institute of Nanoelectronics at the Technische Universität München. They succeeded in simulating our experimentally measured output curves and extracted material parameters. Subsequently, it was demonstrated that our devices are generally suited to build model circuits such as the inverter or the ring oscillator. In this section, only a small summary of the output of this collaboration will be shown. A more comprehensive description can be found in our publication [55].

For the drift-diffusion simulations, the commercially available simulation suite SENTAU-RUS, which was modified for the purposes of organic semiconductors [56, 57], was used.

Besides the standard parameters such as the mobility or the band gap, it was also possible to adjust trap density concentrations and trap site energies in order to reproduce the experimentally obtained conductance curves. Experimentally measured and simulated output curves are presented in Figure 5.8.

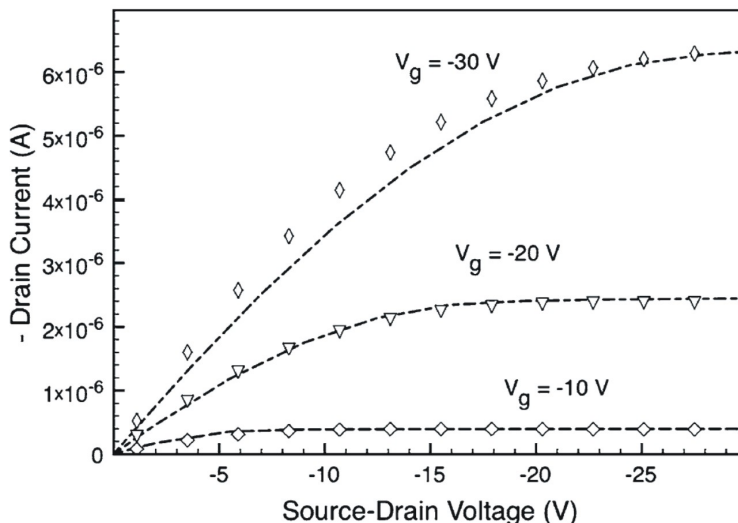


Figure 5.8: Measured and simulated conductance curves of a bottom-contact pentacene TFT. Experimentally measured (symbols) and simulated (lines) output curves for different gate voltages are shown. The simulations were conducted using only one parameter set for all conductance curves.

The simulations extracted a density of positive fixed charges Q_f of $1 \cdot 10^{11} \text{ cm}^2/(\text{Vs})$ and an acceptor-type trap density of $8 \cdot 10^{11} \text{ cm}^2/(\text{Vs})$ at a level of 0.15 eV above the valence band. These densities are in the same order of magnitude as those of deep traps and shallow traps that have been determined in section 5.3 by the threshold shift and the hysteresis, respectively. Unfortunately, it must be noted that the transistors, that we have fabricated at this stage of the PhD-thesis, had an unfavorable channel width to length ratio of $1/2$ with a channel width of $10 \mu\text{m}$ and a channel length of $20 \mu\text{m}$. Moreover, the pentacene film covered the whole sample. Therefore, we have probably considerably overestimated the mobility, which was calculated to be $\mu = 2 \text{ cm}^2/(\text{Vs})$ using equation (2.41). The reason for this overestimation are edge currents, that flow outside of the real channel between source and drain. These edge currents can dominate at such a low channel width to length ratio. In order to prevent these edge currents, Dimitrakopoulos et. al. suggest [23] that either this ratio should exceed a value of 10, or the pentacene film should be structured, as we have done it later during the PhD-thesis (compare Fig 4.1). However, except the mobility the other important parameters such as the subthreshold slope, the threshold voltage and the hysteresis are not affected by the disregarded edge currents. This justifies the assumption, that the simulation provide useful information of our transistors and the extracted parameters should be in the right order of magnitude.

These parameters have been used to simulate the output of an inverter circuit, which is

presented in Figure 5.9. In the inset of this Figure, the simulated inverter circuit with depleted load, a typical design for an inverter, which only integrates transistors of one unipolar type (p-type in the case of pentacene TFTs) is sketched.

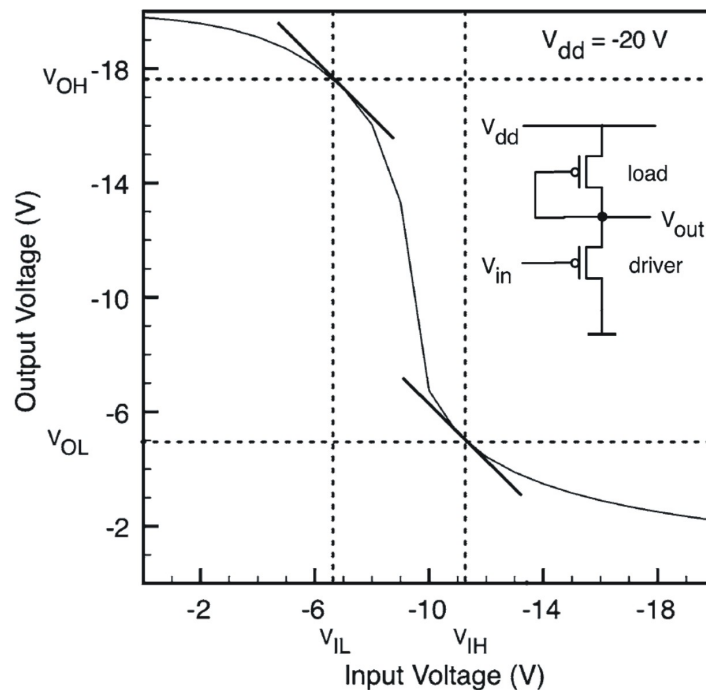


Figure 5.9: Simulated transfer characteristic of organic inverter circuit with depleted load using the extracted TFT transport parameters gained by the simulation of the pentacene transistor, that is shown in Figure 5.8. The organic inverter circuit is sketched as inset.

One step further is the simulation of a ring oscillator, which consists of an odd number of inverters in series with a feed back of the first and last inverter. A ring oscillator is considered to be an important model circuit to proof, if large integrated circuits such as radio frequency identification circuits, which rely on organic field effect devices, are feasible [58]. Furthermore, a three-stage ring oscillator was simulated, as it is depicted in Figure 5.10(a).

This ring oscillator successfully reaches steady-state operation, as it is shown in Figure 5.10(b). The oscillation has got a frequency of 105 kHz , which depends on the load capacitances, which were set to 20 fF in this case. This value might be overestimated, however the purpose of the simulation is to demonstrate feasibility. The main experimental challenge is the structured gate, which is not available in our present configuration.

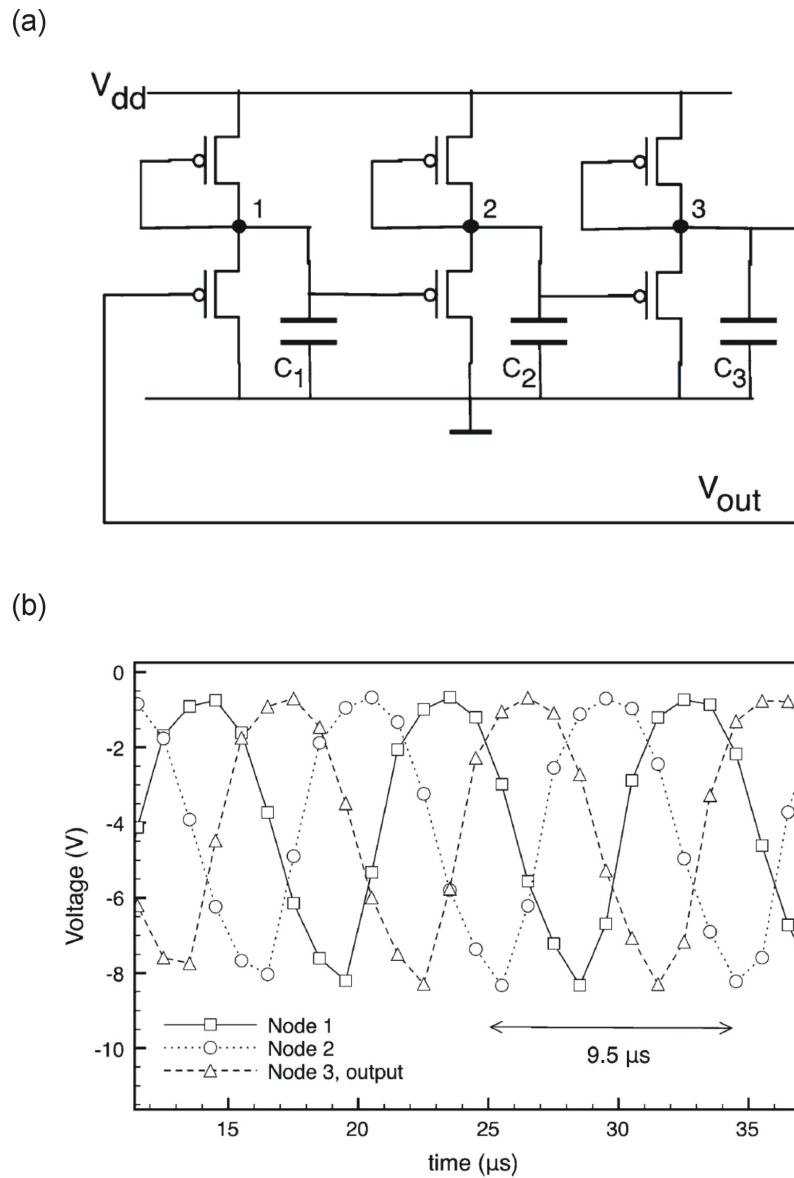


Figure 5.10: Simulation of a three-stage ring oscillator including the inverters used in Figure 5.9. In (a) a schematic of the three-stage oscillator is depicted including load capacitances. The three output nodes are labeled. In (b) the voltage outputs in steady-state operation for the different nodes are shown.

Chapter 6

Electronic thickness dependent in-situ measurements

In this chapter, the results of our in-situ measurements are presented and discussed. Here, the electronic properties of pentacene TFTs during growth have been investigated. A very comprehensive description of these experiments can be found in the diploma thesis of Daniel Beckmeier [59]. The most important results of this chapter are concisely summarized in our publication in the journal *Applied Physics Letters* [60].

6.1 Principle idea of in-situ measurement

The accumulation channel in a TFT is confined closely to the semiconductor-insulator interface within a width given by the Debye length [23, 24], as described in section 2.2.3. Performing capacitance measurements at pentacene Schottky diodes, Lee et. al. determined a carrier concentration of about $n = 3 \cdot 10^{17} \text{ cm}^{-3}$ in a pentacene film [61]. In combination with the low dielectric constant of pentacene of $\epsilon_s = 3 \epsilon_0$, this results in an estimated Debye length of about 5 nm (see Figure 2.9). Therefore, it is crucial to investigate the charge transport characteristics of transistors with very thin organic films, that match this small length scale [62], to address the channel formation. Several groups have studied thickness dependent charge transport phenomena by fabricating and comparing several transistors with varying thin film thicknesses [63–66]. The disadvantage of this method is, that usually it is very challenging to avoid sample to sample variations of organic TFTs, which thus hampers a detailed study of small changes in the charge transport.

In order to enhance the sensitivity to small changes in the transport behavior of organic TFTs, it is useful to conduct in-situ measurements [67, 68]. The idea of this method is to measure the transport of the transistor during the deposition of the semiconductor, as it is sketched in Figure 6.1.

The prepared sample is located and electrically connected in an evaporation chamber. Then, the organic semiconductor, which is pentacene in our case, is evaporated while measuring the thickness of the deposited material as well as conductance and transconductance

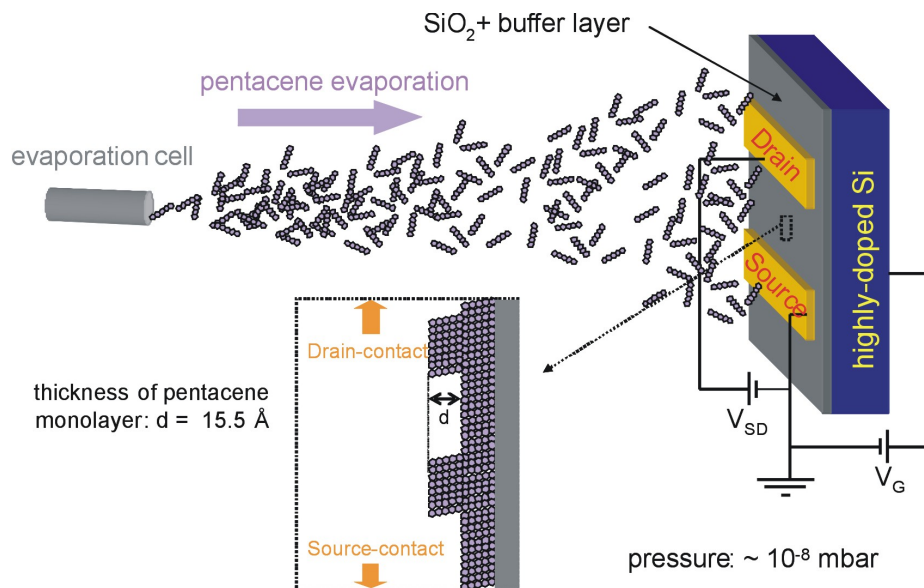


Figure 6.1: Idea of electronic in-situ measurements of pentacene TFTs. During pentacene growth, conductance and transconductance curves are measured.

curves of the TFT.

6.2 Experimental implementation

6.2.1 Measurement setup of in-situ measurements

The in-situ measurements were performed using an existing ultra high vacuum (UHV) chamber with load lock. However, this chamber was not prepared to conduct electronic measurements and to evaporate organic material in a controlled way. Therefore, we had to customize the chamber by equipping it with an evaporation cell and a sample stage. Especially making contact using the load lock was challenging and will be explained in detail below. In the following, a short description of the evaporation chamber including the sample stage and sample holder, is given.

Evaporation chamber

A photograph of the evaporation chamber is depicted in Figure 6.2. For a better overview, the important parts of our measurement chamber for the in-situ measurements are sketched in Figure 6.3.

The evaporation chamber is equipped with a Perkin Elmer ion getter pump and a titanium sublimation pump. Originally, the base pressure was about 10⁻⁹ mbar, but due to the electronic components and several feed throughs, that had to be added, it deteriorated about one order of magnitude to roughly 10⁻⁸ mbar, which was measured by a Balzers full

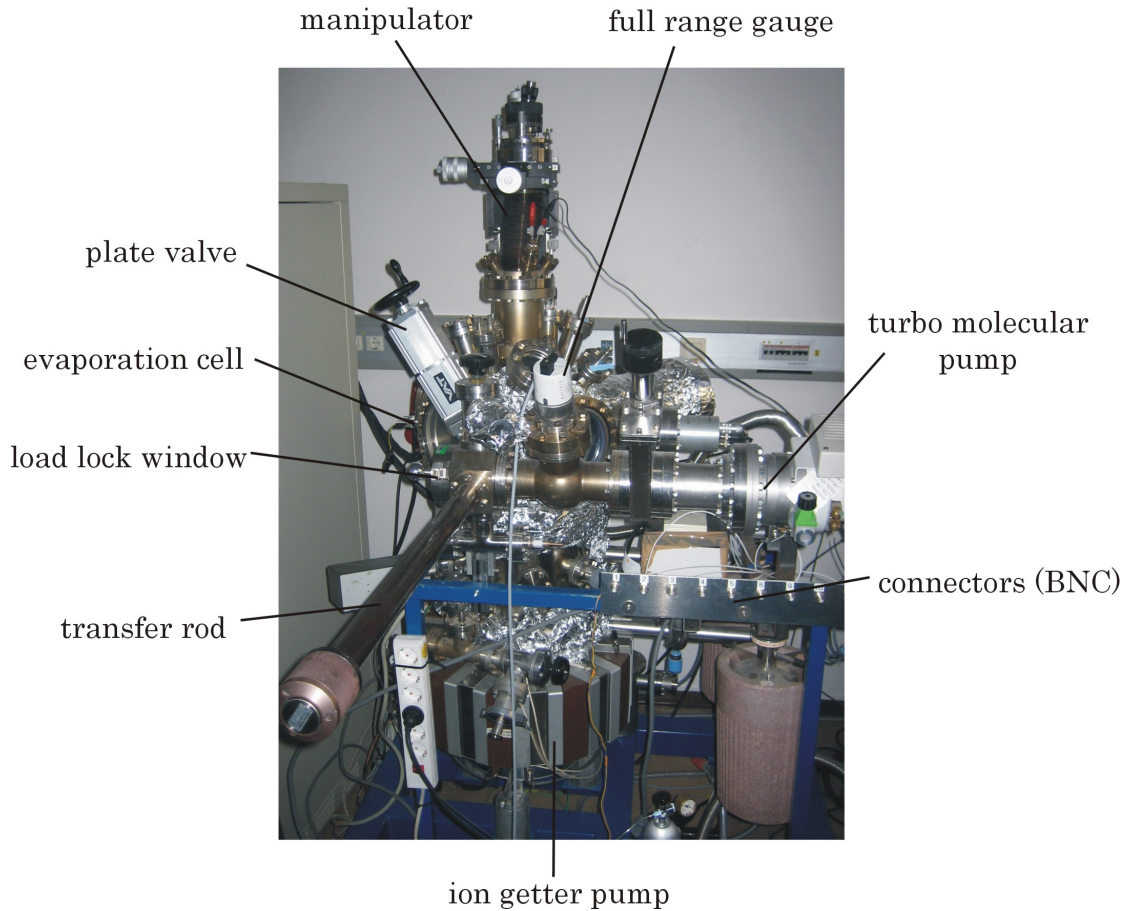


Figure 6.2: Photograph of evaporation chamber. Most relevant parts for the in-situ measurements are labeled.

range gauge. This pressure was sufficient for our experiments and is comparable to the pressure of the UHV evaporation chamber, that we used for the fabrication of our standard transistors (see Figure 4.1). We incorporated a tantalum bag, that was resistively heated by an electric current, as described in section 4.3. A new sample stage, which is explained in more detail below, was mounted at a manipulator rod, that was located in the center of the chamber. It was possible to rotate the sample stage enabling us to turn the samples in and out of the evaporation flux. Furthermore, two quartz crystals were installed adjacent to the sample stage at the manipulator rod in order to measure the thickness of the deposited pentacene. The sample stage could be transferred into the main chamber without braking the vacuum using a transfer rod. The load lock was evacuated by a turbo molecular pump, that worked in combination with a rotary vane pump. As soon as the pressure of the pre-vacuum chamber was below 10^{-5} mbar, the plate valve, that separated the pre-vacuum chamber from the main chamber, could be opened to enable the transfer of the sample holder to the sample stage. The whole mounting procedure could be done within about ten minutes.

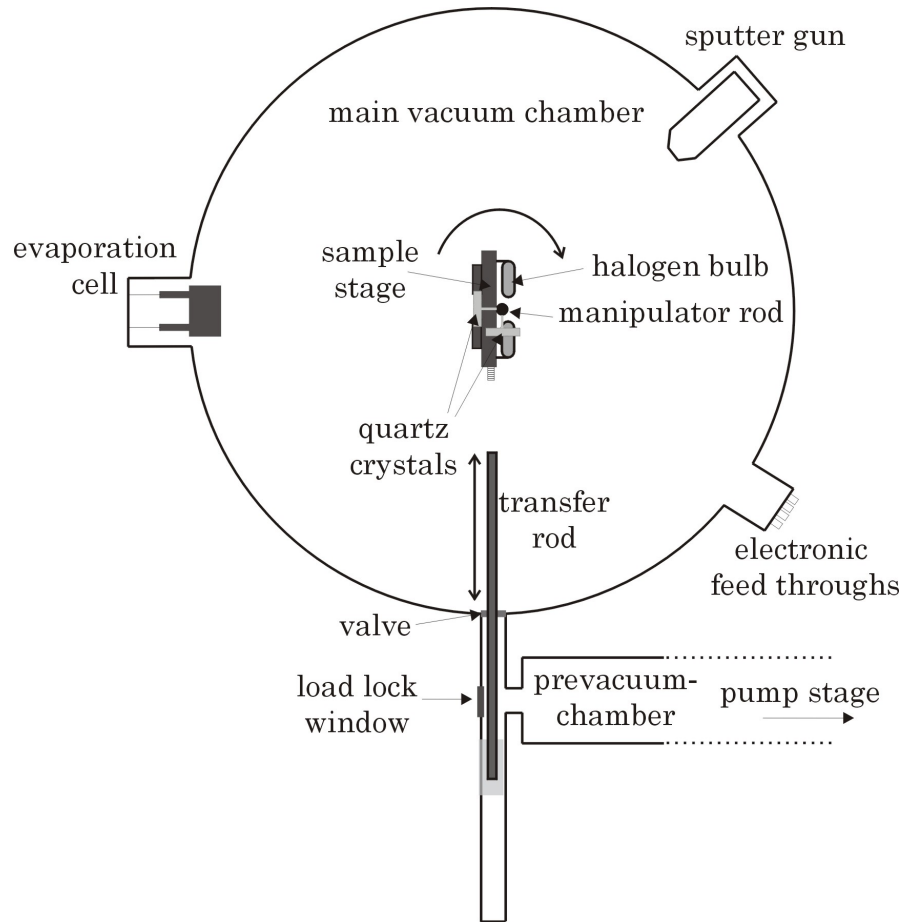


Figure 6.3: Schematic overview of the in-situ measurement chamber. For clarity purposes, only the main components, which are relevant for the electronic in-situ measurements, are sketched.

Sample stage

A completely new sample stage for the in-situ measurements was built. The design was optimized to comply with the following demands:

- transfer of the sample holder and clamping it as stable as possible
- electrically connecting the samples to the feedthroughs of the evaporation chamber
- heating the samples and controlling the sample temperature
- measuring the deposited thickness
- turning the samples in and out of the evaporation jet
- capability for high vacuum

For high vacuum capability, any use of alloys including tin or zinc should be avoided, which excludes soldering. Therefore, clamping was used as often as possible. Ceramics should be chosen as insulator materials, since polymers usually do not endure temperatures above 100°C commonly used for annealing.

The sample stage consisted of three parts, namely the quartz crystals, the upper station part and the lower station part. All these parts were clamped at the manipulator rod, which consisted of an inner and outer rod and was located in the middle of the evaporation chamber (see Figure 6.4).

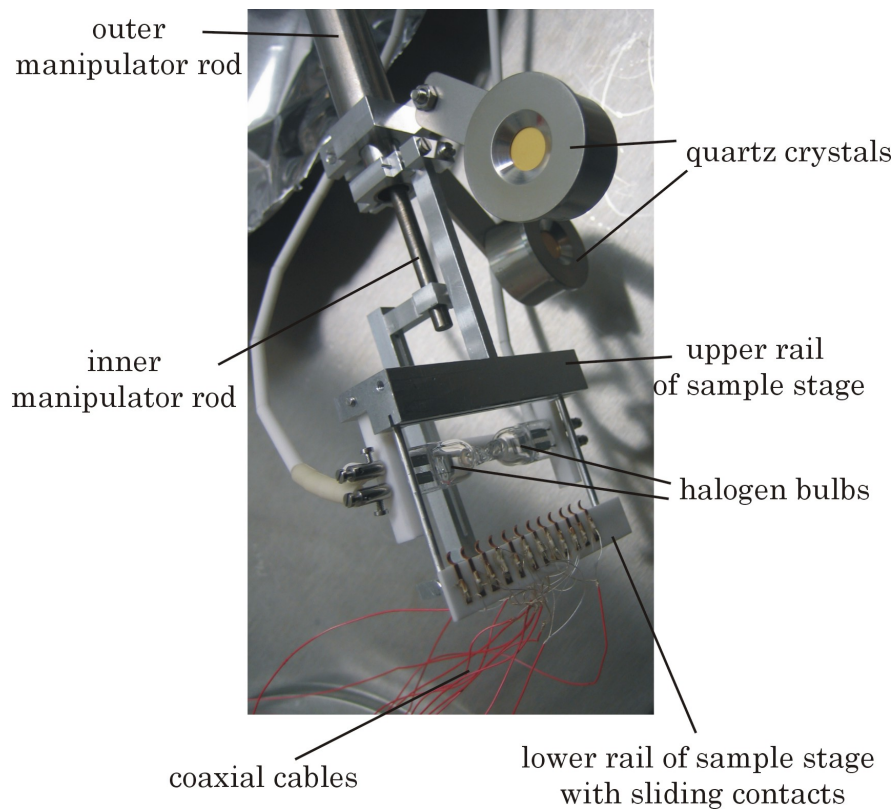


Figure 6.4: Photograph of the sample stage. Most relevant parts for the in-situ measurements are labeled.

First, two quartz crystals were clamped at the outer rod of the manipulator. One was orientated in the same direction as the upper and lower station part, and one was orientated perpendicular to it. This allowed us to measure the evaporation rate, when both, the samples were turned into and out of the evaporation jet.

Second, the upper stage was clamped below the crystals. The upper stage consisted of mainly two important parts. First, a sliding rail was designed in order to enable a precise mounting of the sample holder. Second, two 20 W halogen light bulbs were put behind the designated position of the mounted sample holder and electrically connected to a feedthrough. This allowed us to heat the samples up to temperatures of about 200°C .

Third, the lower stage was clamped at the inner rod of the manipulator. The inner rod of

the manipulator could be moved independently of the outer rod enabling us to adjust and change the distance between the two stage components. The lower stage part was designed to establish electric contact between the samples in the sample holder and feedthroughs of the chamber. Therefore, we used sliding contacts, that were glued by a vacuum suited silver paste onto a ceramic plate. The sliding contact were connected to further feedthroughs of the chamber using the inner conductors of coaxial cables. The outer conductors of the coaxial cables were connected to the chamber. Furthermore, two guide rods were placed on the lower stage, that guaranteed alignment of the upper and lower stage part.

Sample holder

The sample holder is the counter piece to the sample stage and it is depicted in Figure 6.5.

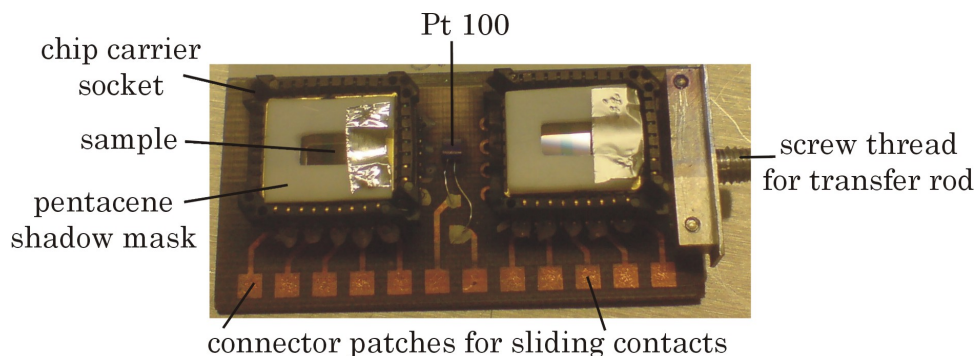


Figure 6.5: Photograph of the sample holder. Most relevant parts for the in-situ measurements are labeled.

It is a plate made of a vacuum-capable composite and contains two sockets for the chip carriers, which are electrically connected to contact patches, that were defined lithographically on the plate. The floor basement of the sockets and the plate below the socket itself have been removed to increase the thermal contact between the halogen light bulbs and the samples in the chip carrier. Finally, for temperature measurement a Pt 100 was glued on the plate and connected to the patches.

6.2.2 Sample preparation for in-situ measurements

The samples that we used for the in-situ measurements were prepared in the exactly same way as it was described in chapter 4 up to the deposition of the contacts. We could only measure two transistors of one sample during deposition, therefore we adjusted the contact evaporation shadow masks for the purpose of the in-situ measurements (see Figure 6.6). Using these shadow masks, two transistor structures with a source-drain spacing of $25\ \mu\text{m}$ were evaporated. The thickness of the contacts was between $30\ \text{nm}$ and $60\ \text{nm}$ (compare Figure 4.1 (c)). The TFT width of $3.5\ \text{mm}$ was defined by the pentacene shadow masks, that were glued on the chip carriers, as it is shown in Figure 6.5.

In contrast to samples that were not measured in-situ, the samples had to be electrically

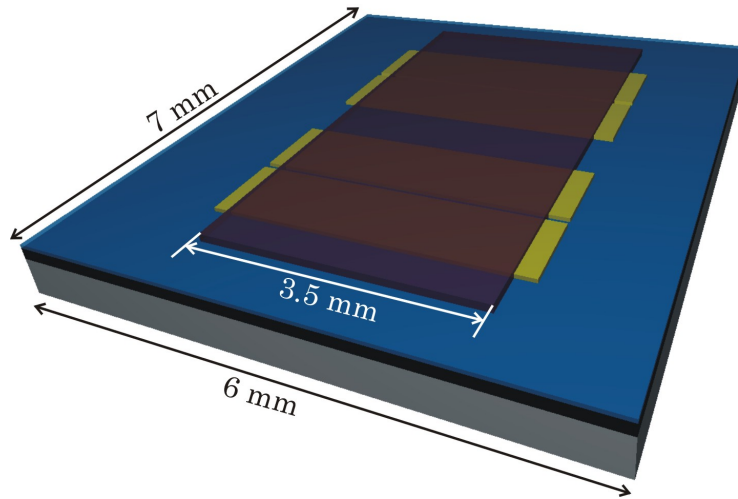


Figure 6.6: Design of the samples for the in-situ measurements. For a side view, cf. Figure 4.1.

connected prior to pentacene deposition. For this purpose, the samples with the gold structures were glued into a chip carrier with silver paste and bonded.

6.2.3 Mounting of the sample

The bonded samples in the chip carriers were pushed into the sockets of the sample holder. Subsequently, the pentacene shadow masks were put on the chip carriers using carbon adhesive tape (also compare Figure 6.5). Then, the pre-vacuum chamber was vented, the load lock door was opened and the sample holder was screwed on the transfer rod. After shutting the load lock door, the pre-vacuum chamber was evacuated to a pressure below 10^{-5} mbar. Now, the plate valve, that connected the two vacuum chambers, was opened and the transfer rod with the sample holder was approached carefully to the guide rail of the upper sample stage. The lower stage part should be sufficiently lowered using the inner rod of the manipulator to avoid contact of the sliding contacts with the sample holder at this moment of transfer. After the holder had completely been inserted into the guide rail, the lower sample stage part was slowly lifted to fix the sample holder in the sample stage and to establish contact between the sliding contacts and the connector patches of the sample holder. Now, the transfer rod could be carefully rotated to unscrew it from the sample holder, before it was pulled back completely into the pre-vacuum chamber. Finally, the plate valve could be closed, but before it should be verified that the transfer rod is removed far enough, so that the sensitive plate valve can not be damaged hitting the rod. In order to check if the sliding contacts made contact to the contact patches, we used an EG & G LockIn 7265 amplifier to measure the capacitance between the gate contact and all source and drain contacts. If no contact could be established, the capacitance signal can not be determined. If this happened, the mounting process had to be repeated.

6.2.4 Measurement procedure

After mounting, the samples were annealed for some minutes using the halogen light bulbs to remove adsorbates. If the samples were covered by a polymer buffer layer, the temperature was not increased beyond 100°C . If no polymer layer was used, the temperature could be elevated to 200°C . Higher temperatures should be avoided, as some components of the sample stage and the sample holder start to melt at temperatures at about 250°C .

We usually deposited pentacene at room temperature, hence the evaporation could not be started before the samples cooled down, which could last several hours due to the little thermal contact in high vacuum. Once the samples have reached room temperature, the titanium sublimation pump was turned on to further improve the vacuum, which typically resulted in a pressure close to $1 \cdot 10^{-8} \text{ mbar}$.

Before the evaporation started, the sample holder was turned away from the evaporation cell, so that the second quartz crystal was orientated towards this cell. We used the same Labview program to control the pentacene deposition, shown in Figure 4.4 of section 4.3. When the evaporation rate has reached the value for deposition, the sample holder was turned into the evaporation jet and the in-situ measurement was started using a measurement scheme, which is depicted in Figure 6.7.

We evaporated the pentacene very slowly at a rate of about 0.02 \AA/s , while the voltage sweeps were performed very fast at a rate of 4 V/s . This combination was chosen to guarantee that the thickness increase of the pentacene layer during one voltage sweep is only on the order of 1 \AA . The thickness of one monolayer (ML) of the pentacene thin film phase is 15.4 \AA (compare Figure 3.8), therefore a thickness change of 1 \AA can be neglected. During the deposition, we continuously repeated a defined measurement cycle.

This measurement cycle consisted of five transconductance gate voltage sweeps from $V_G = +40 \text{ V}$ to $V_G = -40 \text{ V}$ (off-to-on gate sweep) and back from $V_G = -40 \text{ V}$ to $V_G = +40 \text{ V}$ (on-to-off gate sweep), while the source-drain voltage was kept constant at $V_{SD} = -20 \text{ V}$. Subsequently, one single conductance curve was measured by sweeping the source-drain voltage from $V_{SD} = 0 \text{ V}$ to $V_{SD} = -40 \text{ V}$ for a constant gate voltage of $V_G = -20 \text{ V}$. During all sweeps, we have continuously recorded the source-drain current.

The evaporation was usually stopped, when a film thickness was reached, at which the transconductance and conductance curves did not change significantly any more. Usually, this happened at a nominal pentacene thin film thickness between 30 nm and 100 nm . Nevertheless, if the curves changes much beyond a thickness of 100 nm , the measurement was also stopped. For finishing the deposition, we first turned the samples out of the evaporation jet and subsequently stopped to drive the evaporation cell.

6.3 Experimental results

6.3.1 Thickness dependent conductance and transconductance

First, an overview of the trends of the measured conductance and transconductance curves in dependence of pentacene thickness is given. Selected conductance curves with nominal

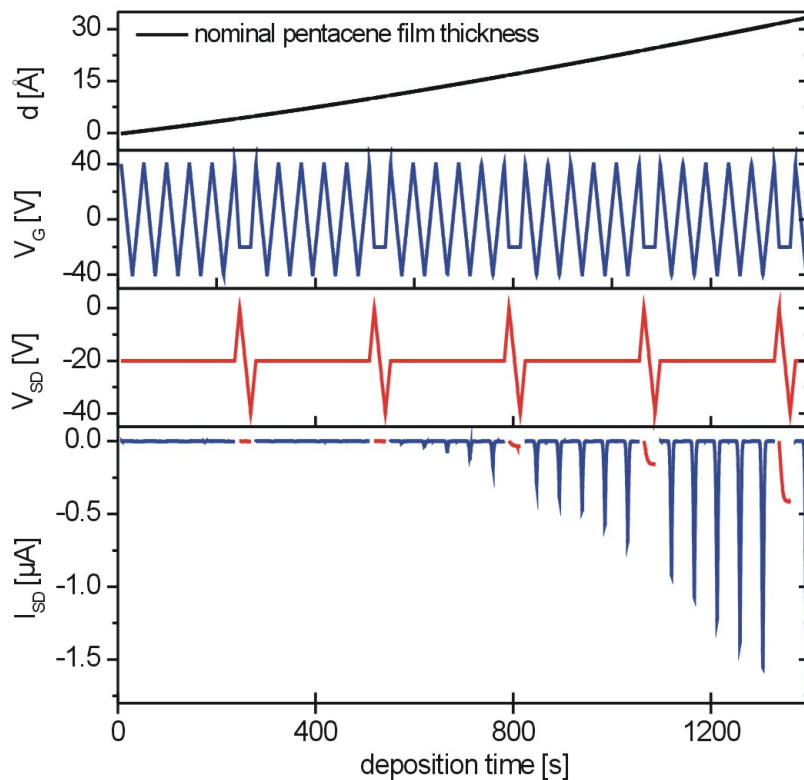


Figure 6.7: In-situ measurement scheme. During pentacene deposition, the source-drain current is continuously measured while gate and source-drain voltage sweeps are performed. One measurement cycle consists of five gate voltage sweeps followed by a single source-drain voltage sweep. This measurement scheme is repeated during the pentacene deposition time for up to several hours. Adapted from [60].

pentacene film thicknesses of 17 Å, 48 Å, 101 Å, 201 Å, and 399 Å are presented in Figure 6.8.

The pentacene film thickness is called nominal, since for thicker films, the pentacene does not grow in a layer by layer fashion. This leads to a large surface roughness of several pentacene monolayers (see AFM picture in Figure 3.7). Hence, the film thickness, that is monitored by the quartz crystals, is an average film thickness, which we call nominal. One monolayer (1 *ML*) is 15.4 Å thick (see Figure 3.8), i.e. the nominal pentacene thicknesses allocated to the conductance curves in Figure 6.8 correspond to 1.1 *ML*, 3.1 *ML*, 6.6 *ML*, 13.1 *ML*, and 26.9 *ML*. The conductance curves show the typical saturation behavior for large source-drain voltages and an ohmic linear behavior for small source-drain voltages, as it is expected for a unipolar p-type TFT (see Figure 2.13) and as it was measured for the samples, that have been measured ex-situ (see Figure 5.2). It is clearly visible, that

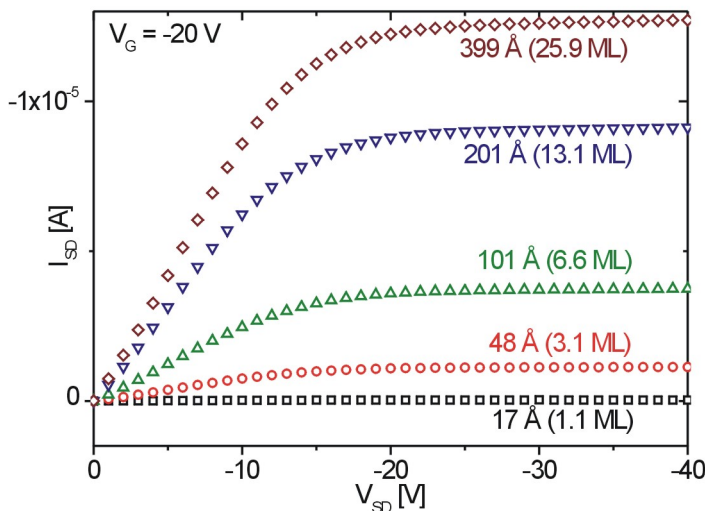


Figure 6.8: Conductance curves for a gate voltage of $V_G = -20 V$ for selected pentacene thicknesses for a single transistor with a polystyrene buffer layer. Adapted from [60].

the linear slope of I_{SD} for small V_{SD} and the saturation value of I_{SD} increase with rising pentacene film thickness.

Transconductance curves for a nominal pentacene film thickness of 1.5 *ML* and 25 *ML* are shown in Figure 6.9. For both film thicknesses the transconductance curves show typical behavior of an unipolar p-type TFT with depletion for positive V_G and accumulation for negative V_G , as it was explained in section 2.3.2, and also measured ex-situ, which is shown in Figure 5.3. The mobility of the TFT with the ultra thin layer of 1.5 *ML* was $1 \cdot 10^{-3} \text{ cm}^2/(\text{Vs})$ and hence much smaller compared to the same TFT with a larger pentacene coverage of 25 *ML*, when its mobility increased to $3.4 \cdot 10^{-2} \text{ cm}^2/(\text{Vs})$. The threshold voltage, as it was defined in section 2.3.3, for the 1.5 *ML* coverage was about $-20 V$ and thus more negative than for the 25 *ML* coverage, where it was at about $-14 V$. The hysteresis, as it was defined in section 2.3.3, was considerably larger for the ultra thin pentacene layer with nearly 2 *V* than for the 25 *ML*-thick film, where it had decreased to less than 1 *V*.

6.3.2 Thickness-dependent transport characteristics

In order to investigate the thickness dependence of the TFTs more thoroughly, we have analyzed the mobility, the threshold voltage and the hysteresis evolution, including all measured transconductance curves of chosen TFTs. In Figure 6.10, these transport characteristics are plotted against the nominal pentacene film thickness to up to 25 *ML* (same transistor as in Figure 6.8 and 6.9).

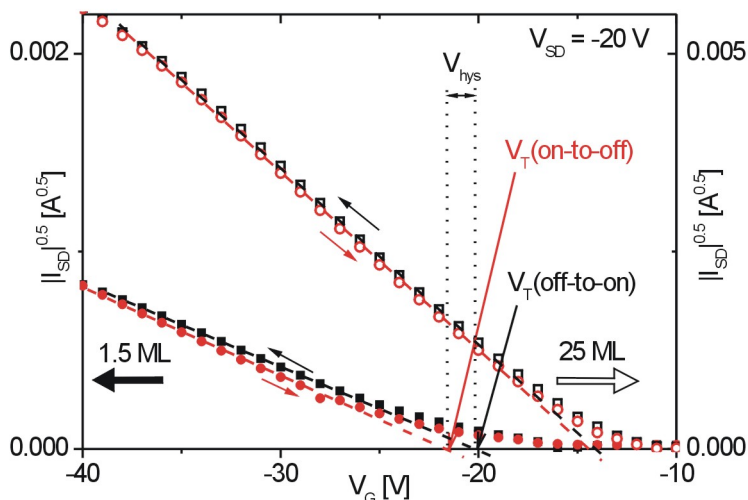


Figure 6.9: Transconductance curves at a source-drain voltage voltage of $V_{SD} = -20 V$. Shown are the off-to-on and the subsequently performed on-to-off gate sweeps for two different nominal pentacene thicknesses of $1.5 ML$ and $25 ML$. Please note, that the y-axis for the transconductance curve measured at $1.5 ML$ is on the right, while it is on the left for the measurement at $15 ML$. Adapted from [60].

The first source-drain current is measured at a coverage of about $0.7 ML$, which can be seen in the inset of Figure 6.10 (a). A similar onset thickness for the source-drain current was also measured by Dinelli et. al. [63] and Park et. al. [69]. This can be explained by percolation theory. Nucleating islands, that initially grow as described in section 3.4, start to coalesce at such a pentacene coverage forming a continuous path from source to drain. Once, we have stopped the deposition at a test sample as soon as we detected the first current signal beyond noise, which was at a coverage of $0.7 ML$. Then, the sample was unmounted and an AFM micrograph, which is depicted in Figure 6.11, was taken.

The single monolayer islands are clearly visible in the AFM picture. Only a very small fraction of the sample is covered by a second monolayer of pentacene. This confirms the layer-by-layer growth mode for the first monolayer, that was observed by Ruiz et. al. [31]. For such a two-dimensional growth, theoretical calculation also predict a percolation threshold thickness at a coverage between $0.66 ML$ and $0.68 ML$, depending on the shape of the nucleating islands [70, 71]. It can be nicely seen, that the first monolayers of the single grains started to coalesce. A possible percolation path for charge carriers is drawn into the AFM picture. At this early stage of charge transport during deposition, there is no straight line from source to drain which does not cross parts of the sample, that is uncovered by pentacene. Hence, the transport path between the contacts is effectively longer than the channel length. Therefore, the mobility, that is determined using equation

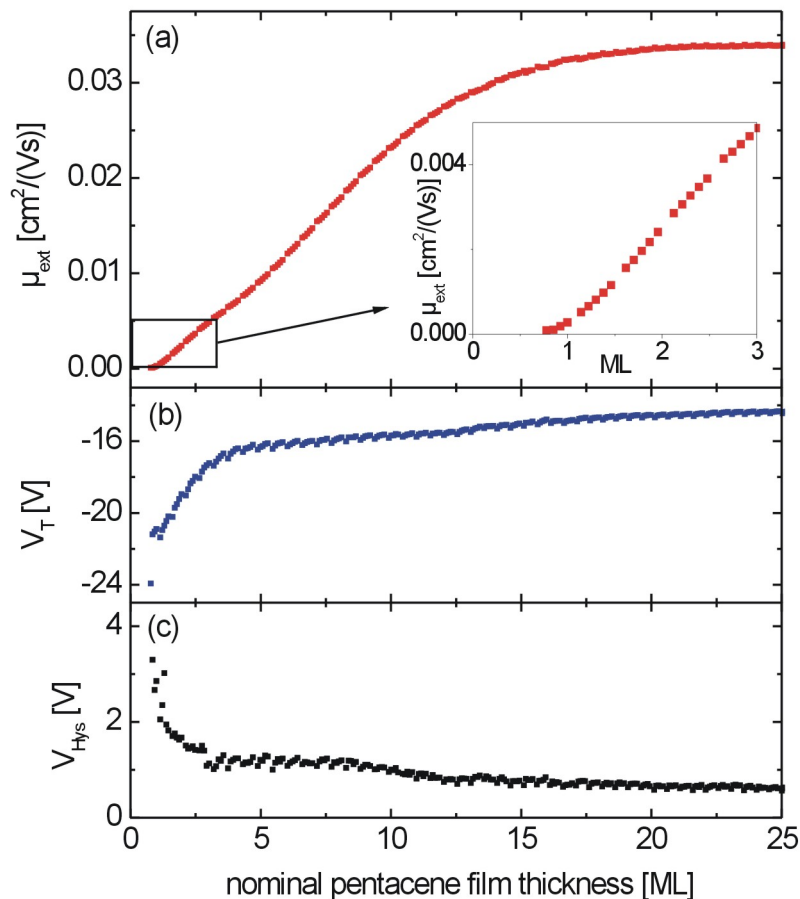


Figure 6.10: Thickness dependence of (a) the extrinsic mobility, (b) the threshold voltage and (c) the hysteresis of a pentacene transistor with a polystyrene buffer layer. Adapted from [60].

(2.39) or (2.41), underestimates the real mobility due to the curved percolation paths for the carriers. Therefore, the values, that are calculated using this equation, will be called extrinsic mobility μ_{ext} in the following.

In Figure 6.10(a), this extrinsic mobility is plotted against the nominal pentacene film thickness. It increased strongly during the deposition of the first 15 *ML*, before it started to saturate at a value of about $0.034 \text{ cm}^2/(\text{Vs})$. The threshold voltage shifted during the evaporation of the first 3 *ML* from -22 V to -17 V . For larger pentacene coverages, the threshold voltage only changed slowly to even more positive values. The hysteresis also changed strongly during the deposition of the first 3 *ML*. Initially its value is about 3 V , but for a thickness of 3 *ML* it decreased to about 1 V . Further increase of the pentacene thickness only resulted in comparatively small changes.

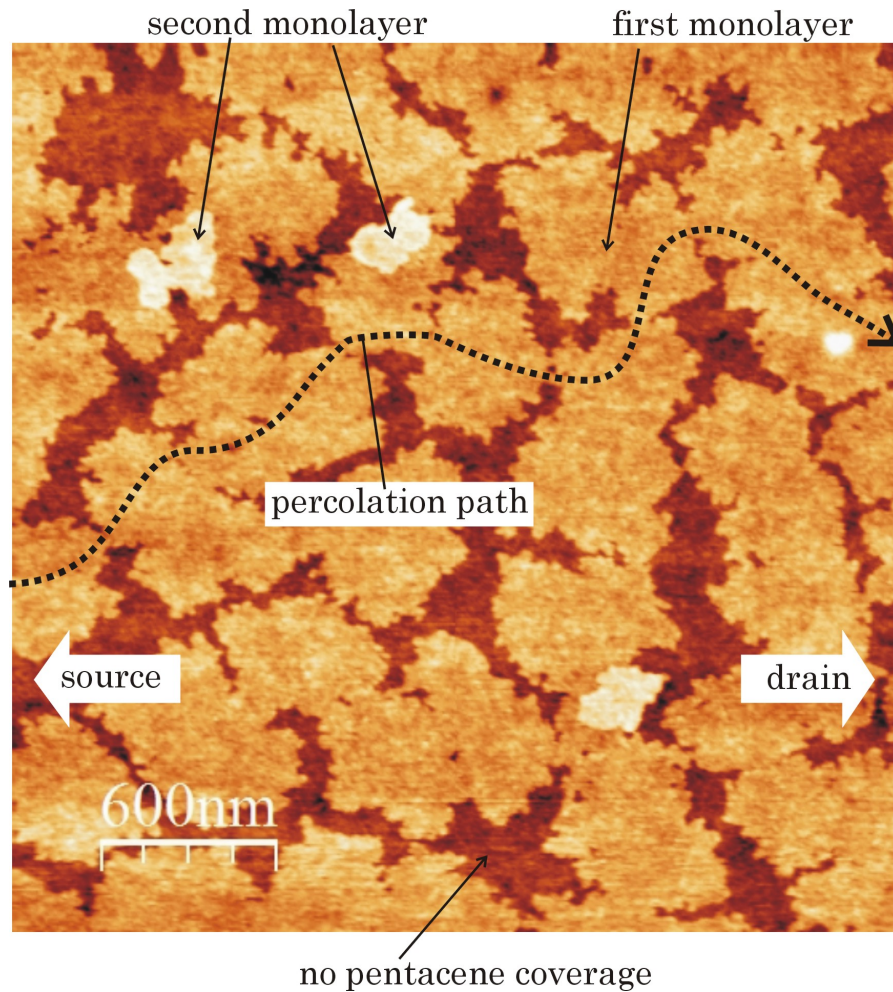


Figure 6.11: AFM micrograph of pentacene film at percolation threshold thickness. The AFM was taken of a test sample that was unmounted from the in-situ chamber as soon as source-drain current could be detected. The crystal quartz measured a thickness of $0.7 ML$.

For comparison, a second device, for which topas was used instead of polystyrene as buffer layer, is shown in Figure 6.12.

In this device, the mobility increased strongly during the deposition to up to $4 ML$, before it saturated very early at a value of $\mu_{ext} = 0.27 \text{ cm}^2/(Vs)$. Of all our measured pentacene transistors, it showed the smallest saturation thickness and the highest threshold mobility. Generally, mobilities and threshold thicknesses of our TFTs varied. By trend, transistors showing a low mobility saturated later than those with high mobility. Some of our worst transistors without a polymer buffer layer did not saturate even for thicknesses far beyond 50 nm . In contrast, the evolution of the threshold voltage and the hysteresis were qualitatively very similar for all our TFTs, meaning that they strongly change within the first

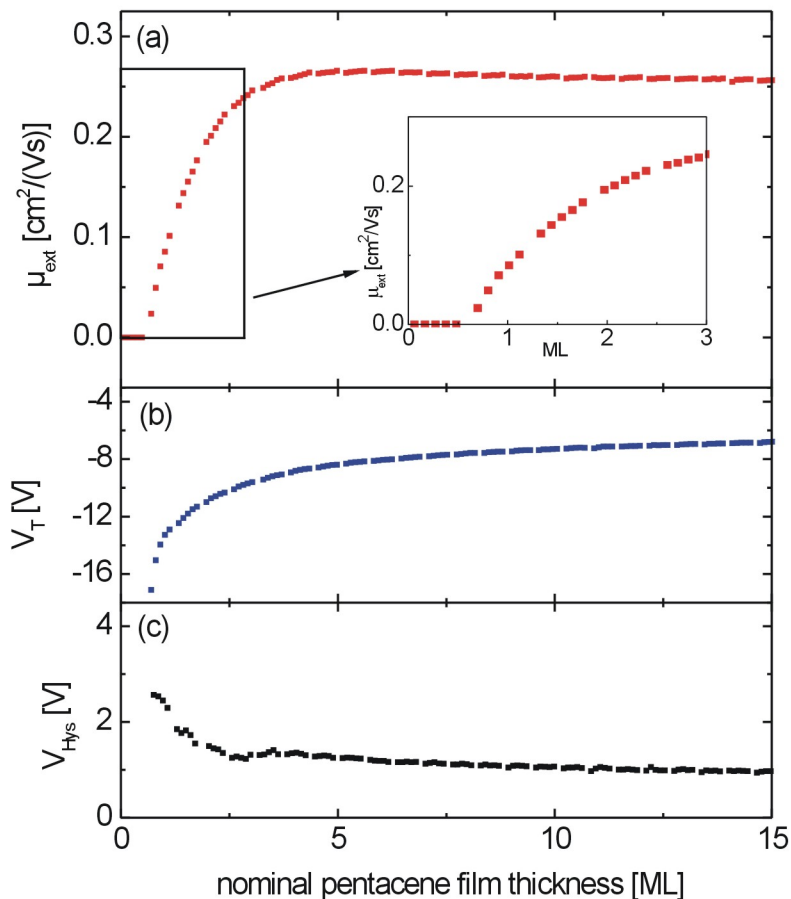


Figure 6.12: Thickness dependence of (a) the extrinsic mobility, (b) the threshold voltage and (c) the hysteresis of a pentacene transistor with a topas buffer layer.

3 *ML* before they started to stabilize. This can be seen by comparison between the devices shown in Figure 6.10 and Figure 6.12.

6.4 Discussion

The transport in organic semiconductors is strongly influenced by electronic states within the bandgap. The origin of these trap states can be explained by the polaron model, which is described in section 3.3.2 (see also Figure 3.5). When the trap states get charged or discharged, they change the operating point of the transistor resulting effectively in a change of the threshold voltage. In general, one can imagine, that the trap states are located on qualitatively three different sites. First, they can be at the interface between the dielectric

and the pentacene layer. In the following, these trap states are called interface trap states. Second, they can be within the bulk of the pentacene film, thus they are called volume trap states. Finally, they can be located on the uncovered surface of the pentacene film. These states can be named surface trap states.

Let us first consider the influence of interface trap states. It is well known, that the surface of silicon oxide is terminated by hydrophilic hydroxy groups. This dielectric surface attracts water molecules that can penetrate through the pentacene layer to the interface thus forming trap states. Therefore, we have coated the silicon dioxide with a hydrophobic polymer buffer layer in order to prevent water molecules to adsorb at the interface. Moreover, the in-situ measurements are performed in vacuum under a pressure of about 10^{-8} mbar. In such an environment, the amount of water molecules should be negligible resulting in comparatively little interface trap states. Considering the in-situ measurements, the interface trap states are expected to shift the threshold voltage of a TFT, but not depending on the pentacene thickness. Comparing the polystyrene coated TFT of Figure 6.10 with the topas coated TFT of Figure 6.12 reveals that the threshold voltage of the TFT with a polystyrene buffer layer had a threshold voltage which was shifted in comparison to the threshold voltage to the TFT with a topas buffer layer by about -5 V. This shift might be explained by interface traps, but it is very difficult to analyze this shift quantitatively, as also TFTs with the same coating showed significant sample to sample variations. The shift might also be due to differing interface dipoles, that arise from the interface between the silicon dioxide and the polymer buffer layer. It was shown by Pernstich et. al [72], that using self assembled monolayers with varying dipole moments, the threshold voltage can be tuned.

Volume trap states, shifting the threshold voltage or causing hysteresis in pentacene TFTs, have also been suggested [73,74] to influence the transport properties in pentacene TFTs. It was argued, whether these volume trap states capture holes or electrons. The positive threshold voltage shift during the deposition of the first 3 ML – 4 ML in our experiment can only be explained by an increasing amount of volume trap states, that capture electrons but not holes. During the deposition of the first monolayers, more and more electron trap states are filled by electrons resulting in a negative charging of the transistor channel. Consequently, a more positive gate voltage is needed for compensation resulting in a threshold voltage shift towards a more positive value. It is possible to estimate the area density of filled electron volume trap states $n_{e^-}[x]$ between a nominal pentacene film thickness of $(x - 1)$ ML and x ML using

$$n_{e^-}[x] = \frac{C_i}{e} (V_T[x] - V_T[x - 1]) \quad (6.1)$$

where e is the elementary charge, C_i the area capacitance of the dielectric, and $V_T[x]$ is the threshold voltage for a coverage of x ML of pentacene. Inserting the threshold voltages obtained from Figure 6.10, we obtain $n_{e^-}[2] = 2.5 \cdot 10^{11} \text{ cm}^{-2}$, $n_{e^-}[3] = 2.1 \cdot 10^{11} \text{ cm}^{-2}$, and $n_{e^-}[4] = 1.0 \cdot 10^{11} \text{ cm}^{-2}$. The density of trap states in the first monolayer can not be calculated, as the threshold voltage without pentacene can not be determined. Since beyond 4 ML nominal pentacene thickness the threshold shift is dramatically reduced, we

argue that the width of the accumulation channel, which is called the Debye length (see section 2.2.3), is nominally $4 ML$ in our transistors. Since the pentacene does not grow in a layer by layer fashion after the first monolayer [31], this probably corresponds to three completed monolayers of pentacene. Pentacene that is deposited beyond three monolayers is probably still full of deep volume trap states and these trap states do probably still form but are not filled any more, as the gate voltage is screened. In Figure 2.9 it can be seen, that for a bulk hole concentration of $3 \cdot 10^{17} cm^{-3}$, which was determined for pentacene [61], the theoretical Debye length for pentacene is about $5 nm$. This is in very good agreement with our result of $3 ML$, as this corresponds to a thickness of roughly $4.5 nm$ (compare Figure 3.8). The slight increase of V_T for larger pentacene film thicknesses could arise from the bulk conductance, as suggested by equation (2.32). Unfortunately, this increase was not observed for all of our transistors. Therefore, we think that the slight variation of the threshold voltage, that we observed beyond $4 ML$ is also caused by bias stress [75].

The hysteresis behavior can not be explained by volume trap states, as an increase of shallow volume trap states during pentacene deposition would lead to an enhanced hysteresis, which was not observed. Therefore we propose, that the hysteresis is associated with shallow trap states, that are located at the surface of the pentacene film. These shallow trap states at the surface can be expected from the polaron model, that was described in section 3.3.2. In the polaron model, the energy of the electronic states is altered by the polarization energy. Due to equation (3.12), the polarization energy of an electronic state of a particular molecule is dominated by the sum of the polarizabilities of its adjacent molecules. It is not surprising, that this energies are shifted at the surface of the crystal. This energy shifts can result in electronic states, that are within the bandgap of the pentacene bulk. Furthermore it was suggested, that shallow trap states at the surface might arise from molecular sliding or in general from distortions of the molecular arrangement [76].

Up to a nominal pentacene film thickness of $4 ML$, the surface is within the Debye length. As long as the surface of the pentacene film is within the transistor channel, these surface trap states get filled and emptied by the applied gate voltage, resulting in the hysteresis. However, the more the pentacene film surface is grown out of the transistor channel, the more surface trap states get screened, i.e. they are not filled or emptied by the gate voltage. This results in the observed decrease of the hysteresis, sketched in Figure 6.13.

After the deposition of three monolayers of pentacene, the whole surface of the pentacene film is beyond the Debye length and the hysteresis saturates. Since both the threshold voltage shift and the hysteresis saturated for all transistors close to a nominal pentacene film thickness of $4 ML$, we conclude that the potential landscape of our pentacene TFTs converged at this coverage.

However, the mobility did not saturate at this pentacene thickness. We think, that the mobility in our transistor was probably dominated by extrinsic factors, such as contact barriers or grain boundaries [64, 77]. The strong sample to sample variations that we observed in the mobility evolution, is also in favor of the domination of extrinsic factors. Additionally, for very thin layers one has to take into account, that the measured mobility is reduced due to the percolation, that was explained above. Therefore, the mobility of thin films is probably not suited for the investigation of the intrinsic transport properties

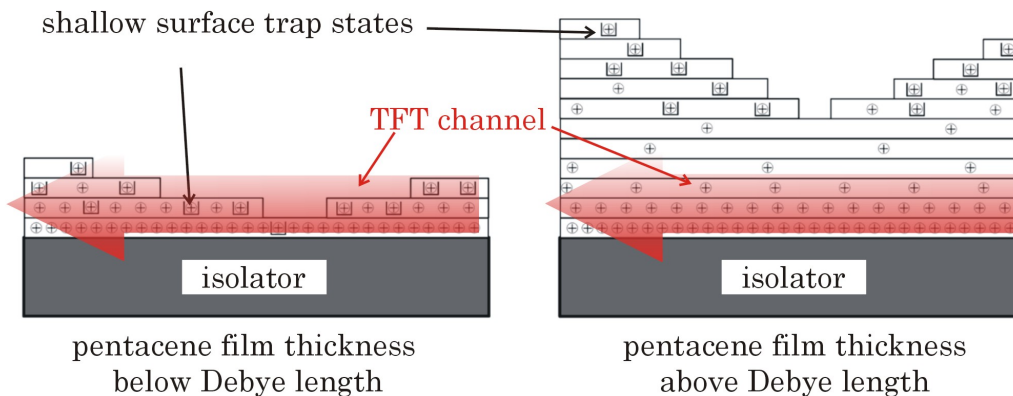


Figure 6.13: Model of surface trap states. On the right, the pentacene film thickness is below the Debye length. Therefore, shallow trap states at the surface are within the transistor channel. On the left, the pentacene film thickness is above the Debye length. In this case, the surface is grown out of the transistor channel and the shallow trap states do not affect the current transport in the TFT.

of pentacene. Nevertheless, it is important to know, that in order to optimize the performance of pentacene transistors, the pentacene layer should be much thicker than the Debye length of $3 ML$ of the transistor.

In conclusion, we have described the evolution of the threshold voltage and the hysteresis by deep bulk and shallow surface trap states, respectively. Only trap states within the Debye length of about $5 nm$ influence the device. Therefore, for optimization one has to address the first three monolayers. The mobility seems to be very vulnerable to extrinsic influences and thus not suited to investigate intrinsic properties of pentacene thin films.

Chapter 7

Spatially resolved optoelectronic measurements

This chapter describes our spatially resolved measurements at pentacene thin film transistors. This work was done together with Martin Göllner and Christian Westermeier, who both finished their diploma thesis during the course of this PhD-thesis [78, 79]. After the principle and the implementation of a laser scanning microscope is explained, the chapter presents and discusses the reflection and the luminescence measurements at pentacene films. Subsequently, a detailed summary of the results of the spatially resolved photoresponse measurements is given. Finally, these results are discussed and a model is developed to explain the observed behavior. The measurement setup and some of the results of the spatially resolved photoresponse have been already published in the journal *Applied Physics A* [80].

7.1 Principle of laser scanning microscope

A pentacene film is composed of micrometer sized grains with different crystal orientations and with grain boundaries in between. At source and drain, the film is on top of the metal contacts, which disturb the growth (see also the AFM micrograph in Figure 3.7). Furthermore, the symmetry of this device is broken by the two voltages, one at the drain contact and one at the back gate. However, optical and optoelectronic measurements at organic TFTs are predominantly performed using a global illumination. Similar to electronic measurements, this method integrates different contributions arising from various regions of the transistor into one single signal. Hence, global illumination makes it difficult to address the influence of inhomogeneities in the device. Our idea was to exploit the lateral structure of the TFT by implementing a laser scanning microscopy technique to disentangle different contributions. The principle of operation of this microscope is sketched in Figure 7.1.

A laser beam is focused at a transistor on a sample stage, which can be moved laterally with high precision using a piezo stage. The light can be switched on and off with a constant

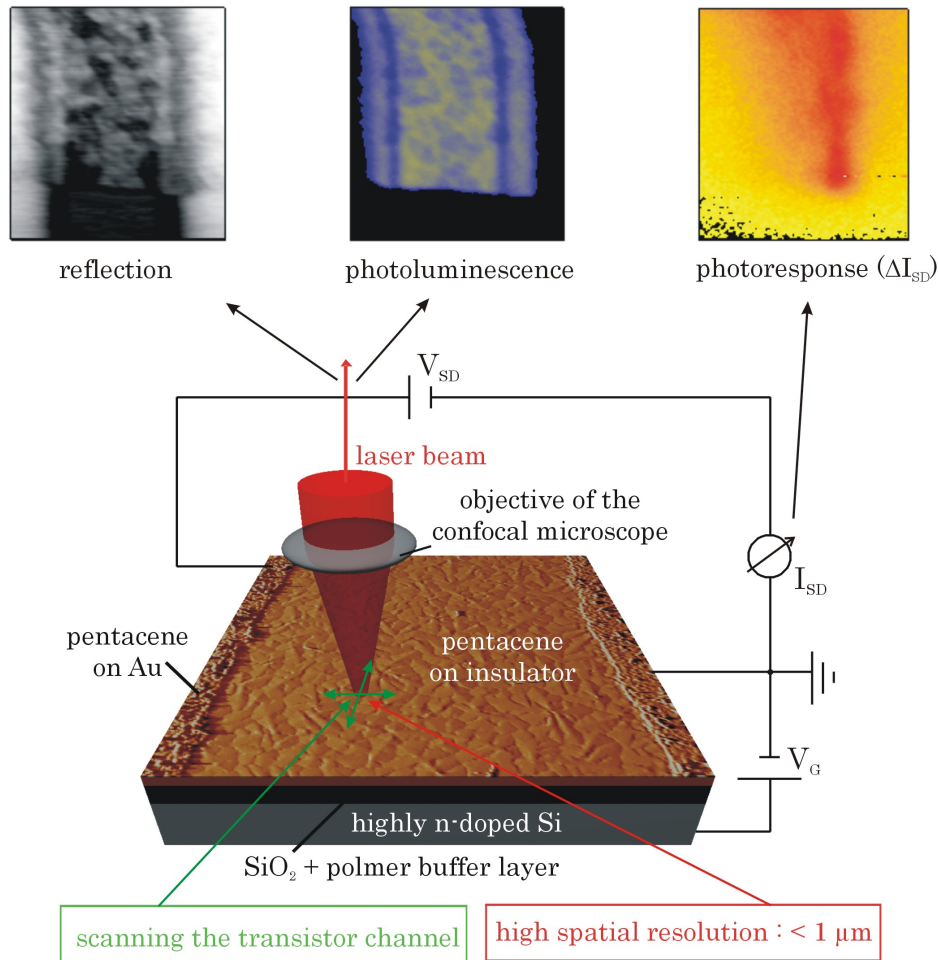


Figure 7.1: Principle of the laser scanning microscope. The sample with a TFT in operation is moved beneath a focused laser beam. The reflected laser light, the photoluminescence and the change of the source-drain current caused by illumination, which is called photoresponse, are measured in dependence on the position of laser light excitation. For illustration, scanned maps of the reflection, the photoluminescence and the photoresponse are shown on top.

frequency. The reflection and the photoluminescence light get partly collected by the same lens, which focused the incident laser light. As the photoluminescence is redshifted compared to the reflected light, these two signals can be separated by a dichroic mirror and thus directed to different detection devices. A source-drain voltage and a gate voltage is applied to drive the transistor, and the change of the source-drain current between light on and light off, the photoresponse, is measured, while the transistor is scanned using the piezo stage. Signals which are measured for each position of the laser excitation, are therefore the reflection, the photoluminescence and the photoresponse. These signals can be assembled to two-dimensional maps (see top of Figure 7.3).

7.2 Measurement setup

In order to meet our requirements, a home-made laser scanning microscope in combination with a brightfield microscope and an optical spectrometer was designed and developed during this PhD-thesis. The setup was improved several times, therefore only the final version is explained in the following. Photograph of the setup can be seen in Figure 7.2.

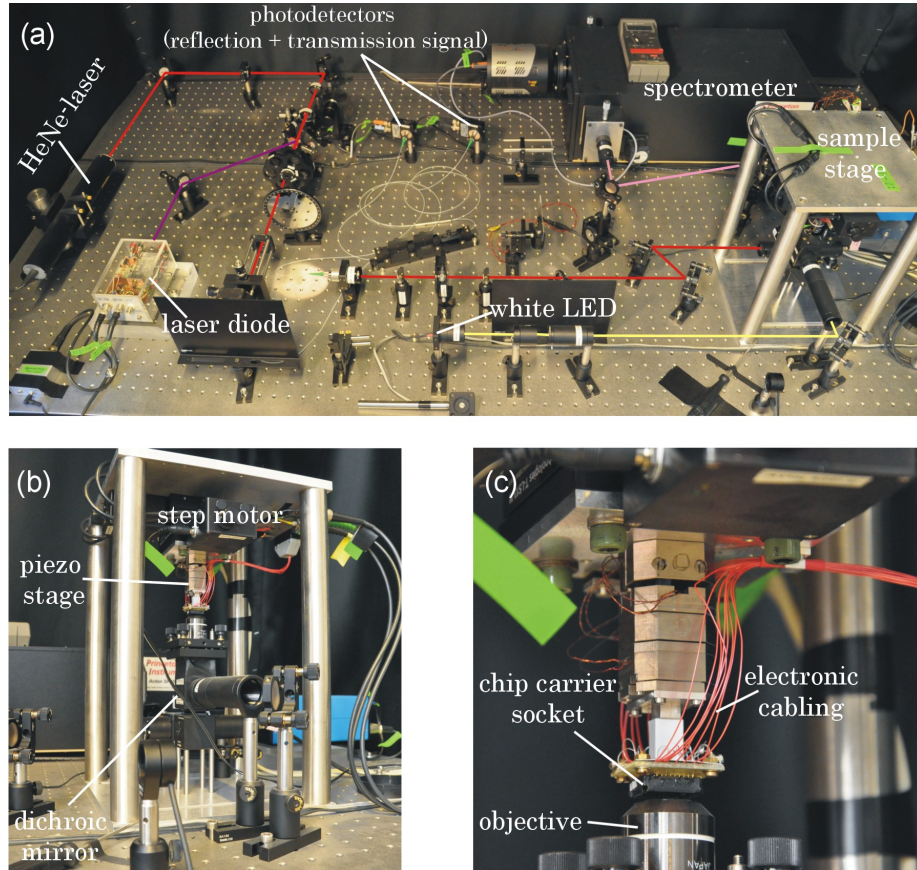


Figure 7.2: Photographs of the optical setup in the final stage of the PhD-thesis. Some crucial components of the setup are labeled. (a) The whole configuration on the optical table including the light sources, the detectors and the sample stage. (b) The hanging sample stage with the sample on top of the piezo stage. (c) Zoom towards the sample showing the electronic cabling and the close gap between the socket of the sample and the objective caused by its small operating distance of 3.4 mm .

For a schematic overview, see Figure 7.3.

Optical setup of the laser scanning microscope

For the laser scanning microscope, we have used a Helium-Neon (HeNe) laser as standard light source. The wavelength of this laser is 632.8 nm , which corresponds to an energy

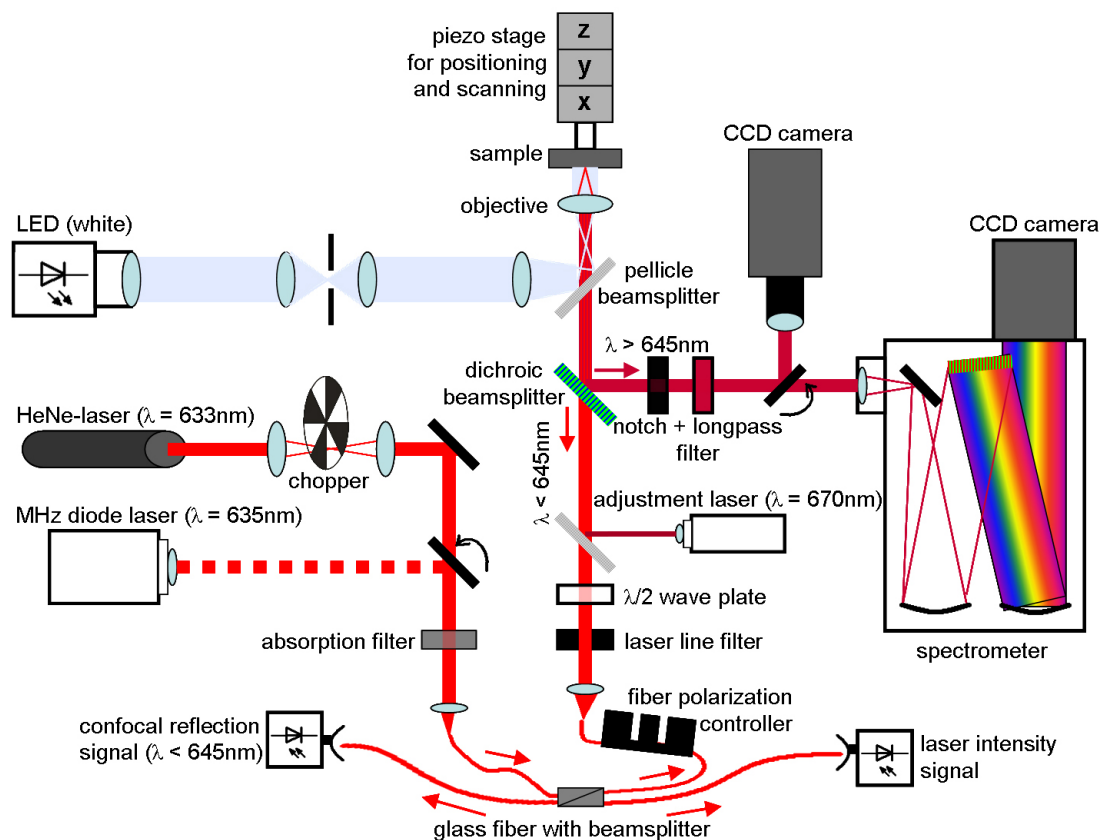


Figure 7.3: Optical measurement setup. The optical setup consists of a brightfield microscope, a confocal laser scanning microscope operating in reflection mode, a photoluminescence microscope and a spectrometer.

of 1.96 eV . This wavelength is suited for pentacene, as it shows an absorption maximum at 1.95 eV (compare Figure 7.7). The laser light passed a chopper (Thorlabs MC2000) to switch the light on and off at a frequency that could be chosen between 2 Hz and 10 kHz . The light was focused through the chopper blade to minimize edge effects due to the spatial extension of the laser beam (a more detailed explanation is given in the diploma thesis of C. Westermeier [79]). For measurements beyond a frequency of 10 kHz , we installed a pulsed laser diode with a wavelength of 635 nm . This laser diode was driven by a lock-in amplifier at a maximum frequency of 250 kHz . Turning a flip mirror, the light of this laser diode could be chosen instead of the HeNe-laser.

The light first passed adjustable absorption filters to control the incident light intensity before it was coupled into a glass fiber with the help of a lens and a coupling stage. We used a single mode glass fiber with a fiber beamsplitter (50:50), that split the light into two parts. One part was directed to an amplified silicon photodiode (PDA10A), that measured the transmission signal. The other branch of the fiber guided the light through a fiber polarization controller, which enabled us to polarize the light linearly by twisting the fiber appropriately. The light left the fiber through a lens and passed a $\lambda/2$ wave plate. The po-

larization axis of the linearly polarized light could be adjusted to the desired orientation by turning the $\lambda/2$ wave plate accordingly. Subsequently, the parallel laser light was directed towards a dichroic mirror. The dichroic mirror only reflected light above a wavelength of 645 nm , hence the incident light transmitted this mirror. Then, the light was focused by a 100 fold objective with a numerical aperture of 0.85 on the sample, that was mounted on the sample stage (also compare Figure 7.2 (c)), which is described below.

Reflected light and photoluminescence light, that was emitted of the sample at an angle of below 54° was collected by the objective. The reflected light had the same wavelength as the incident light, therefore it passed the dichroic mirror and got focused back into the glass fiber. The glass fiber acted like a pinhole. Therefore, only a parallel light beam got coupled into the fiber. If the sample was not in the focal plane of the objective, the light would not be parallel before the lens in front of the fiber. Consequently, this light would not get coupled into the fiber. That is why the reflection signal, which was detected by a silicon photodiode (PD36A) at the end of one branch of the glass fiber, was measured confocally.

In contrast to the reflection light, the photoluminescence light was mainly redshifted to wavelengths beyond 645 nm . Thus, the photoluminescence light got reflected by the dichroic mirror. The light then passed a notch filter and a long pass filter in order to further reduce the reflection light by about nine orders of magnitude. This enabled the detection of photoluminescence even if the yield was very low. A flip mirror was used to select whether the photoluminescence light was focused directly into a CCD-camera (pco sensicam) for spatially resolved detection, or led into a spectrometer (Acton SP2500) for spectral analysis. The spectrally fanned out signal was finally read out by another CCD-camera (Acton PIXIS 100).

Electronic circuit of the laser scanning microscope

The electronic circuit of the laser scanning microscope is depicted in Figure 7.4.

The setup was optimized for concurrent detection of the source-drain current, the reflection, the photoluminescence and the photoresponse for each position of illumination during the scan.

The sample was scanned using the piezo stack of attocube, which was controlled by an ANC350 controller. The investigated transistor was operated as usual by applying a source-drain voltage and a gate voltage using two Yokogawa 7651 DC sources, as it was also explained in section 5.1. The source-drain current, which was measured at the source contact, was amplified and converted into a voltage signal using a FEMTO DLPCA-200. We measured both, the DC and the AC component of this voltage. For the DC-voltage detection, an Agilent 34410A multimeter was used, while the AC component was measured using an EG&G 7265 lock-in amplifier. The reference frequency for the lock-in detection was supplied by the chopper controller, which modulated the incident light at a constant frequency. The lock-in method was necessary to detect the photoresponse signal, since it was usually much smaller than the DC-signal. The reflection signal, which was preamplified by a silicon diode PDA36A, was also measured by a lock-in amplifier. Alternatively, an

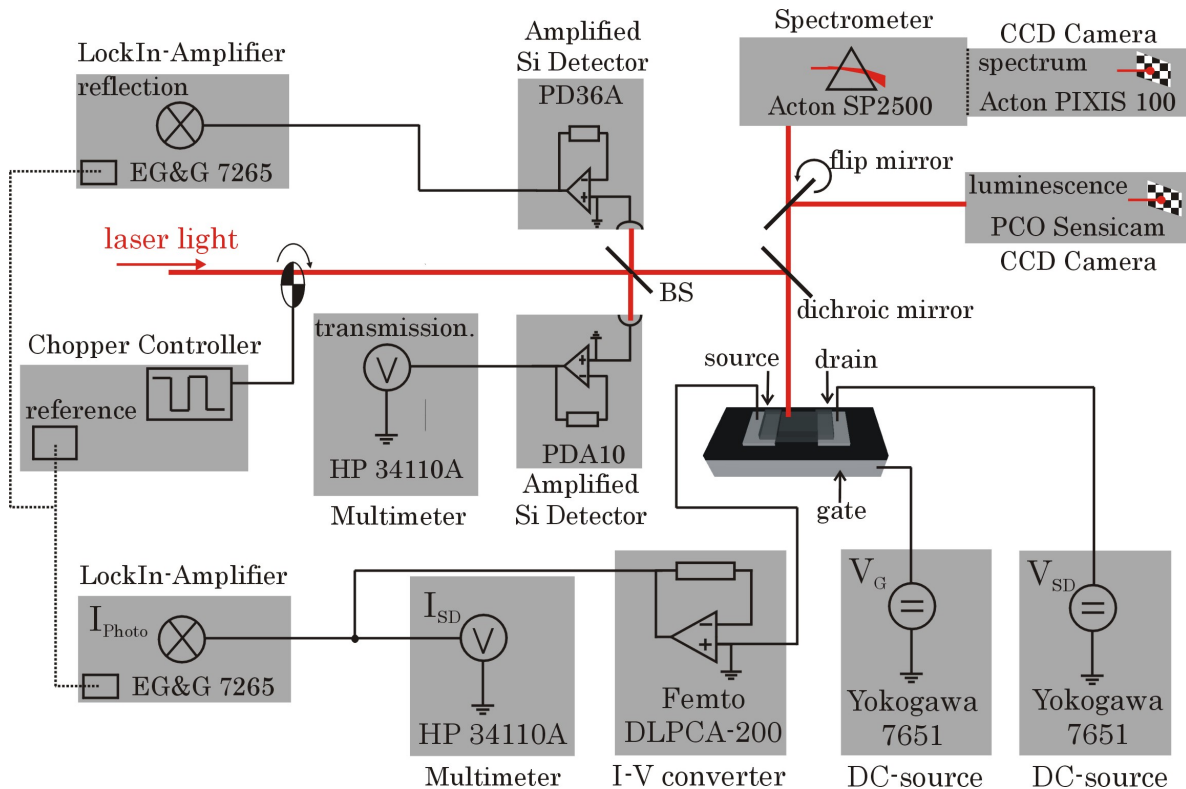


Figure 7.4: Circuitry of the optoelectrical setup. During TFT-operation the source-drain current, the photoresponse, which is the change of the source-drain current caused by illumination, the signal of the reflected laser light, the signal of the incident laser light, the photoluminescence and the spectrum of the photoluminescence could be measured simultaneously in dependence on the position of the laser excitation.

Agilent 34410A multimeter can be used for this signal. In the case of the transmission signal, we used the multimeter to determine the incident optical power prior to scanning. The luminescence signal was measured by a PCO sensicam CCD camera, which had an internal circuitry. The same applies for the Acton SP2500 spectrometer and the Acton PIXIS 100 CCD camera, which were used to record the spectra. The PCO sensicam camera was controlled via a PCI card, while the attocube controller, and the Acton devices were controlled via USB interface. All other detection devices were controlled using GPIB interfaces. A home-made Labview program was developed to allocate all measured signals to the position of illumination, which was controlled by the steps of the attocube piezo positioners.

Positioning system

A crucial component of a laser scanning microscope is the positioning system, which should work as accurately as possible. In our setup, we have used a piezo stack of attocube, which consisted of three linear positioners (attocube ANPx/z 101/RES) for all three directions

to move the sample beneath the focused laser spot. These positioners are powered by slip and stick motion [81]. The controller ANC350 drives the positioners by applying a triangle voltage with two different slopes. During the slow slope, the positioner sticks to the piezoelectric rod and is thus moved forward or backward by a well defined distance, which depends on the magnitude of the applied voltage. During the fast slope, the positioner does not travel, since the rod slips through the positioner due to the moment of inertia of the system. Therefore, the positioner has moved by one step and the piezo rod is unbiased again. This method allows for travel distances of up to about 4 mm with nanometer precision.

A typical two-dimensional scan was realized in the following way. First, the laser spot was moved to the desired starting position of the transistor by applying several steps manually. The scan itself was performed automatically and controlled by a Labview program. First, a single step forward in x-direction was performed. Subsequently, all desired signals were measured, before the next step was done. This was typically repeated between 80 and 120 times in order to drive the illumination spot from source to drain. When a single line of the scan was finished, the transistor was driven back in x-direction to its original position by a well defined amount of backward steps. Subsequently, the sample was moved by a single step in y-direction, before the next line was scanned. This was also repeated between 80 and 120 times before the scan was finished.

In order to calibrate the positioners, we have fabricated a sample with a chess board with an edge length of 10 μm . This sample was scanned and the reflection signal was recorded. The result of such a scan with supply voltages of 28 V for both spatial direction is presented in Figure 7.5(b). For comparison, a CCD picture using the brightfield microscope, which is explained below, is also shown in Figure 7.5(a). 25 steps corresponded to a 10 μm motion in both directions, hence a single step moved the sample by a distance of 400 nm. Furthermore, this scan demonstrated, how accurately this piezo positioners were able to move the sample back to its original x-position, as the chess board was mapped very accurately with sharp edges.

Sample stage and focusing

The sample stage can be seen in the photograph in Figure 7.2(b). The sample was in a chip carrier, which was pressed into a socket. The socket was electronically connected and mounted on a sample holder, which is explained in more detail in the diploma thesis of C. Westermeier [79]. The sample holder could be mounted on a piezo stack, which was on top of step motors, that have been fixed to a metal plate. This whole system could be mounted headfirst on top of metal bars in such a way, that the sample hung closely above the objective.

In order to get the sample into focus, the step motors were used to move the sample laterally roughly into the desired position. Then, the sample was approached towards the objective using the z-axis piezo positioner of the stack. The focal plane could be determined by two different methods. First, the brightfield microscope could be used. The sample was moved as long as the laser spot size was minimized on the CCD-camera. This

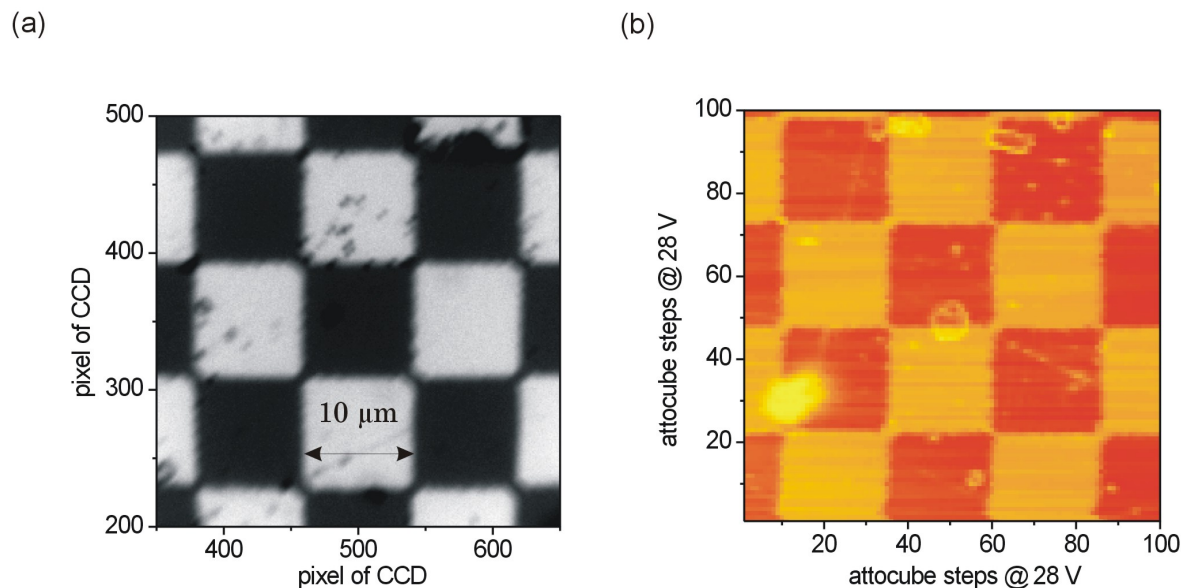


Figure 7.5: Calibration of the laser scanning microscope. A photolithographically defined chess board sample with an edge length of $10\ \mu\text{m}$ was used for calibration. In (a) the chess board is mapped using the brightfield microscope. One pixel of the CCD camera corresponds to $125\ \text{nm}$. In (b) the confocally measured reflection signal of the laser scanning microscope is shown. Using a step voltage of $28\ \text{V}$ to drive the piezo motors, a single step moved the sample of about $400\ \text{nm}$.

method only worked for luminescent light (e.g. from pentacene), since the filters of the laser scanning microscope pass only photoluminescence light but not reflected light to the CCD-camera. If the laser light was directed on parts of the sample without pentacene, the reflection signal was measured confocally. The reflection signal only differed significantly from zero, if the sample was in the focal plane. Therefore, the sample could be approached carefully towards the objective and as soon as the reflection signal peaked, the sample could be considered to be in the focal plane.

Brightfield microscope

The laser scanning microscope was optimized for measuring small signals with a high spatial resolution. However, orientation was difficult, as this method did not allow for mapping the transistor at the CCD-camera. For this purpose, a broad illumination of the sample was needed. Therefore, we included a brightfield microscope in the setup.

A white light emitting diode (LED) was used as light source. Using a pellicle beam splitter, that reflected 8%, the white light could be directed towards the objective, which was also used for the laser scanning microscope. In contrast to the HeNe-laser, the white light was focused into the focal plane of the objective. Therefore, a parallel light beam left the

objective, thus illuminating a broad part of the sample (Köhler illumination). The reflected white light was finally directed into the CCD-camera, which mapped the illuminated area of the sample. In Figure 7.6, an illuminated pentacene transistor channel is shown.

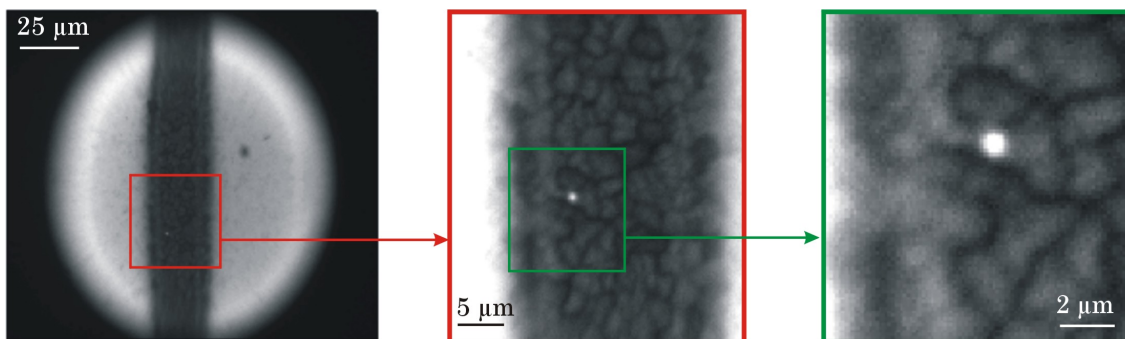


Figure 7.6: Principle of the brightfield microscope. The light of a white LED is focused into the objective resulting in a broad illumination of the sample, which is reflected into a CCD-camera (left). Simultaneously, the position of the focused laser beam on the sample can be observed (middle). The polycrystalline structure of the pentacene film can be resolved, showing that the focused laser spot is significantly smaller than single pentacene grains (right).

Single pentacene grains are resolved by this brightfield picture. Furthermore, the photoluminescence of the focused laser beam can be estimated. It is apparent, that the laser spot was much smaller than the typical size of a pentacene grain. With this brightfield microscope, we were able to position the laser spot very exactly before we performed our laser scans by moving the sample with the piezo stage.

7.3 Absorption measurements

7.3.1 Absorption spectrum

In order to excite pentacene films optically with a high efficiency, as much incident light as possible should be absorbed. Therefore, we have taken an absorption spectrum of a 48 nm thick pentacene film, that was evaporated on a glass substrate. The absorption spectrum was taken with a Xenon lamp as light source and an UV/VIS Spectrophotometer Jasco V-550. The absorption of the pentacene film on glass was subtracted by the absorption spectrum of the glass substrate, giving the absorption spectrum of the pure pentacene film, which is depicted in Figure 7.7.

Mainly, four different absorption peaks can be observed in the spectrum, with energies of 1.85 eV, 1.97 eV, 2.12 eV, and 2.27 eV. Accordingly, a HeNe-laser with a characteristic wavelength of 632.8 nm, which corresponds to an energy of 1.96 eV, is highly absorbed (absorption coefficient $k = 1.8 \cdot 10^5 \text{ cm}^{-1}$) and well suited as source of illumination for optical experiments at pentacene thin films. Electroabsorption measurements, that were

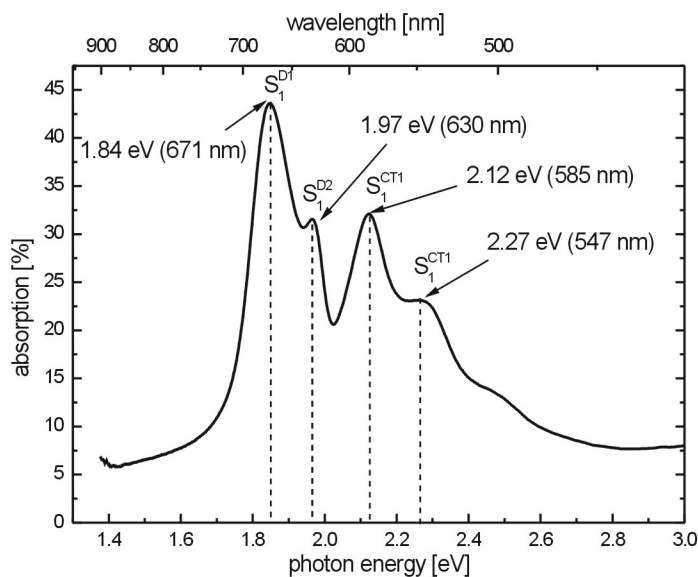


Figure 7.7: Absorption spectrum of a pentacene thin film on a glass substrate with a thickness of 48 nm .

performed by Sebastian and Baessler [82] revealed, that the two lowest energy excitations have a low dipole moment, thus they are of Frenkel type character. Contrary, they observed a quadratic Stark Effect at the two additional absorption peaks centered at 2.12 eV and 2.27 eV . Further sophisticated analysis revealed, that the 2.12 eV excitation can be attributed to a charge transfer state with the hole and electron being at the sites of the two molecules of one unit cell, while the 2.27 eV excitation corresponds to an electron-hole pair, which is situated on two neighboring molecules of adjacent unit cells.

7.3.2 Spatially resolved absorption - Davydov splitting

As explained in section 3.2.2, the excited states are singlet states, since the transmission from the ground state, which is a singlet state, to a triplet state is not allowed due to spin conservation. Therefore, the excitation at 1.85 eV can be assigned to the S_1 state. As shown in section 3.4, the unit cell of pentacene consists of two translationally invariant molecules, which should lead to a Davydov splitting (see section 3.3.1). In order to testify, if the absorption peak of 1.97 eV corresponds to the the second level of the Davydov doublet, we used our spatially resolved measurement setup to determine the reflection of a pentacene film, using linearly polarized light with two different wavelengths. First, we performed a scan with our standard HeNe-laser as light source with a wavelength of 633 nm , which corresponds quite exactly to the 1.97 eV absorption peak. The reflection signal of the HeNe-laser light could be observed confocally as explained in section 7.2. Second, we performed a scan at exactly the same sample position with the same polarization, but

using a laser diode with a wavelength of 670 nm instead. This wavelength corresponds to the absorption peak with the lowest transmission energy (see Figure 7.7). The light beam of this laser diode was integrated in the optical setup by a pellicle beamsplitter behind the glass fiber (see Figure 7.3). For that reason, we could not measure this signal confocally at the usual reflection detector. However, due to its long wavelength beyond 645 nm , the reflected light was directed towards the CCD camera, which acted as reflection detector for this light. Hence, the spatial resolution of the reflection signal at this wavelength was a little bit reduced. Nevertheless, we were able to resolve single pentacene domains for both wavelengths, since the grain size of our pentacene film exceeded the spatial resolution by far. The two reflection maps are depicted in Figure 7.8.

The pentacene film did not reflect the light uniformly. It is evident, that pentacene grains which showed high reflection for HeNe-laser light were less reflective for an illumination with the laser diode and vice versa, which can be nicely seen in Figure 7.8(c), where the reflection of both illuminations are merged and, for differentiation of the two different exciting energies, color coded.

This is exactly the behavior, which is expected in the case of excitation into the two different energy levels of the Davydov doublet. The pentacene unit cell is triclinic, therefore the exact orientation of the transmission dipoles can not be derived as easily as in the case of monoclinic structures. For pentacene, laborious Kramer-Kronig calculations must be performed to determine the extinction coefficients. These calculations show, that the lowest energy excitation is orientated along the crystal axis **a**, while the second lowest energy level can be excited with a dipole along the crystal axis **b** [83,84]. Since the angle between these two axes is about 95.2° , the dipoles of the two transmissions of the Davydov doublet are orientated nearly perpendicularly. Hence, depending on the orientation of a single pentacene grain, light with a given polarization is either efficiently absorbed by light with a wavelength of 633 nm or 670 nm . In a polycrystalline pentacene thin film, this leads to Davydov excitation domains, which, to our knowledge, we could not resolve spatially for the first time in the visible.

Nevertheless, most of the light is not absorbed by the pentacene film. This can be seen in the cut, presented in Figure 7.8(d). The reflection signal variations within the pentacene film are much smaller than the difference to the reflection signal of the gold contacts, which is about five to six times larger. This shows, that only a small fraction of the incident light is absorbed in the pentacene film, but most of it in the silicon substrate beneath the pentacene.

7.4 Photoluminescence and Raman

7.4.1 Spatial distribution and yield of photoluminescence

The luminescence yield of organic materials has gained lots of attraction, since its applications have reached marketability, mainly implemented as organic light emitting diodes (OLEDs) [85]. Polymers, that are often used as semiconductors, show, besides electrolumi-

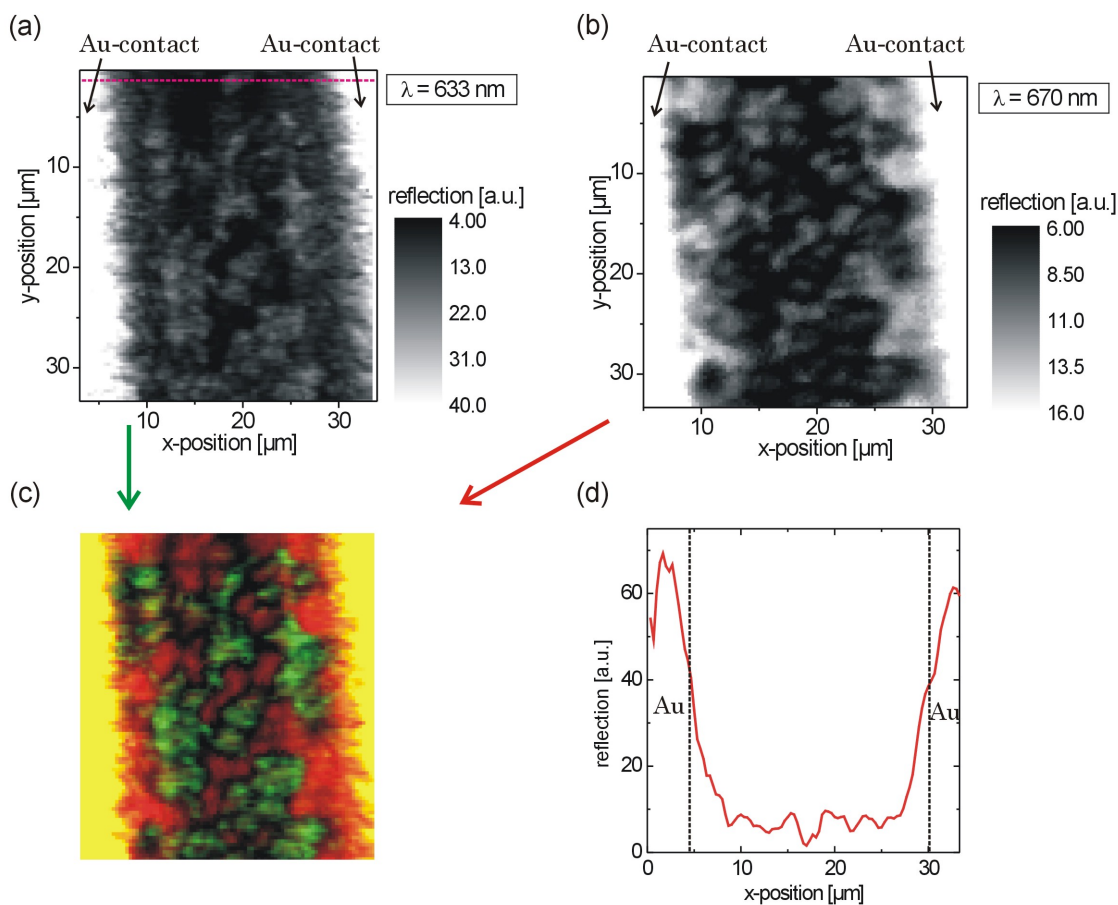


Figure 7.8: Reflection map of a 48 nm thick pentacene film using an illumination with linear polarized light at (a) a wavelength of 633 nm, and (b) a wavelength of 670 nm. Dark areas represent high absorption domains, while bright areas correspond to more transparent regions. In (c) both maps were merged, using a color coding to distinguish illumination with 633 nm (green) and illumination with 670 nm (red). In (d) a section between the two gold contacts at the indicated line in (a) is shown. The gold contacts are on top of the pentacene film.

nescence, very high photoluminescence efficiencies of up to 80% [86]. However, publications on electroluminescence on pentacene are very rare [87, 88] and, to our knowledge, has not been observed in devices using transistor geometry yet. Therefore, it is not surprising that we could not observe electroluminescence in our transistor as well. Publications reporting on photoluminescence at pentacene agree that the photoluminescence yield is very low [89–91].

We included a CCD camera and a spectrometer in our optical setup to measure the photoluminescence spatially and spectrally resolved, as depicted in Figure 7.3. A spatially resolved photoluminescence signal of pentacene on silicon dioxide is depicted in Figure 7.9(a). Here, a very high incident illumination power of $200 \mu W$ and an integration time of $10 ms$ of the CCD camera was used. The reflection signal of a bare gold surface, which was determined using the same light intensity of $200 \mu W$, but a long integration time of $10 s$, is depicted in Figure 7.9(b). This high incident energy was needed for the reflection signal to enable enough light to pass through the notch and longpass filters, which reduce the HeNe-laser light of about nine orders of magnitude. Both signals were maximized by moving the sample into the focus of the laser, using the confocal reflection signal for optimization. It is evident, that both, the reflection signal and the luminescence signal have Gaussian shape with the same width of about $660 nm$. Therefore, it can be concluded, that the pentacene film shows photoluminescence only at the site of illumination. No widening due to diffusion or drift of the excitation states could be observed. Please note, that an absolute displacement of the signal is not refraction limited and could theoretically be determined at least with a resolution given by the CCD pixel size, which corresponds to $125 nm$ at the sample as determined by the brightfield microscope (see Figure 7.6).

The photoluminescence intensity in dependence on the incident optical power is shown in Figure 7.10. A slope of 1.02 reveals a linear dependence within the experimental accuracy for incident optical powers between $1 nW$ and $100 \mu W$. Taking the spatial extension of the excitation spot into account, this corresponds to intensities of about $10^{-1} W/(cm^2) - 10^4 W/(cm^2)$. Therefore, neither saturation or bleaching effects, which would cause a sublinear behavior, nor two photon or bimolecular recombination processes, which would result in a quadratic increase, were observed. Including the spatial pinning of the luminescence leads to the assumption, that the signal arises from a monomolecular recombination process. The external photoluminescence efficiency η , which is defined as

$$\eta = \frac{I_{PL}}{I_{inc}} \quad (7.1)$$

where I_{PL} is the intensity of the photoluminescence signal and I_{inc} is the optical incident intensity of the excitation light, is about 10^{-7} . Even if one includes a quantum efficiency of 0.3 of the CCD camera and an absorption efficiency of about 10%, only a very small fraction of excited states in the thin-film decays radiatively, especially if compared to polymers, that are used for OLEDs [85].

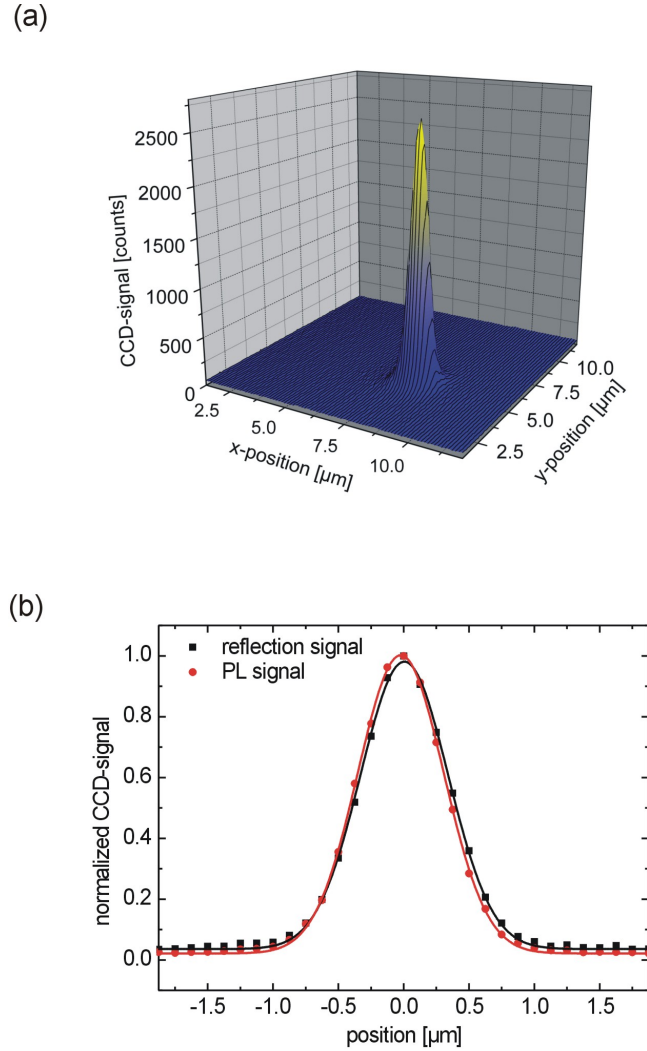


Figure 7.9: Spatial extension of photoluminescence at a pentacene film. Spatial distribution of a photoluminescence peak measured at a 48 nm -thick pentacene film on thermal SiO_2 , which was covered by a 7 nm -thick TOPAS buffer layer. The film was excited by a focused HeNe-laser. (a) Three dimensional plot of the photoluminescence signal in dependence on both spatial directions of the CCD-camera at an illumination of $1\ \mu\text{W}$ and a CCD integration time of 2 s . (b) Cuts of the photoluminescence signal of (a) and a reflection signal on gold with an illumination power of $200\ \mu\text{W}$ and an integration time of 10 s , is shown. Both signals can be fitted by a Gauss curve with a width of 660 nm .

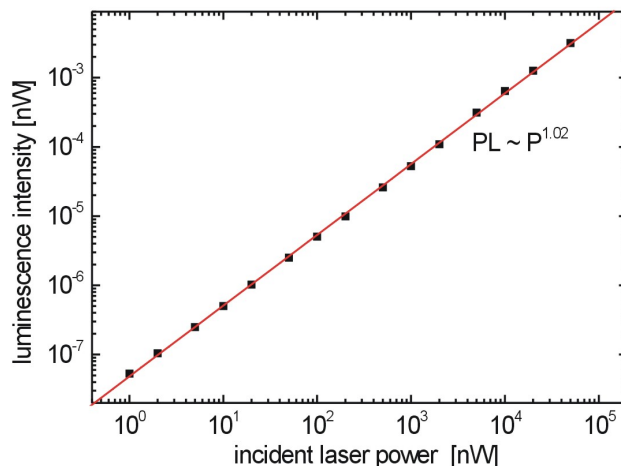


Figure 7.10: Photoluminescence as a function of incident light intensity. The luminescence signal is plotted double-logarithmically against the optical incident power of the HeNe-laser, revealing a linear dependency.

7.4.2 Discussion of low photoluminescence signal - Exciton dynamics

We started a collaboration with Stefan Lochbrunner [92], who could perform transient pump and probe measurements with a 30 fs time resolution. Since these transient measurements are performed in transmission, we prepared a 48 nm -thick pentacene film on a transparent foil of polymeric TOPAS. In the measurement setup, the samples are first excited by 30 fs long light pulse with a center wavelength of 670 nm , using a noncollinearly phase matched optical parametric amplifier (NOPA) [93]. Absorption changes can be either probed over the whole visible spectrum by a light continuum generated in a sapphire substrate, or for the highest time resolutions with a second NOPA at a specific wavelength. Pump and probe beams are overlapped and focused to a spot of $260\text{ }\mu\text{m}$ at the sample, which was oriented normal to the beams or with an angle of incidence of 65° . The change of the transmitted light of the probe beam was measured, which can be expressed in a change of the optical density ΔOD of the pentacene film, which is defined as

$$\Delta OD = \frac{T}{T_0} \quad (7.2)$$

where T and T_0 are the transmission signals with and without pump beam photoexcitation, respectively. A reduction of the optical density for a given probe wavelength can arise from a depopulation of a certain state or a radiative transmission from the excited state, while an increase of the optical density might arise from excited state absorption.

The measurements revealed that the emission from photoexcited Frenkel type states decay

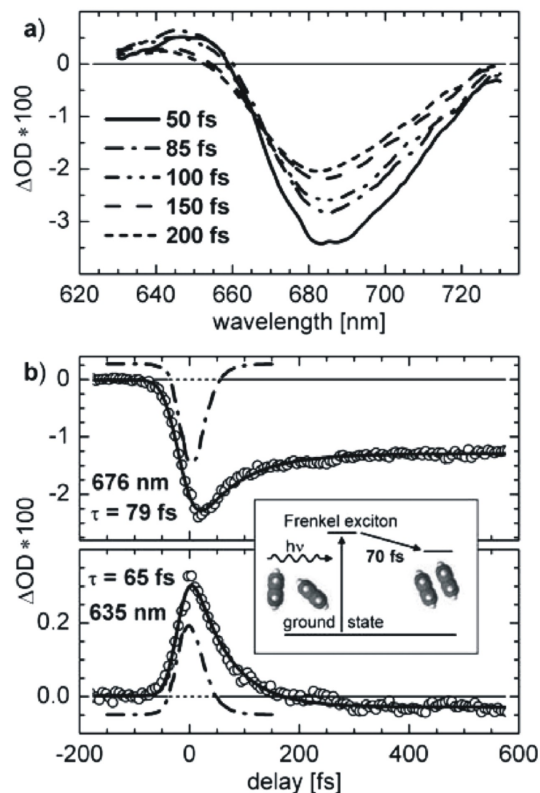


Figure 7.11: (a) Transient spectra under normal incidence during the first 200 fs. (b) Time traces measured with 25 fs probe pulses centered at 635 nm and 670 nm. The inset shows the corresponding energy diagram. Adapted from [92].

within 70 fs after excitation (see Figure 7.11), resulting in a bleach at a probe wavelength of 676 nm and an excited state absorption at 635 nm. This fast quenching of the original state must arise from a transition from the radiative Frenkel exciton to a state with a reduced transition dipole moment.

Jundt et al. [94], who performed similar transient measurement on pentacene films, assigned this ultrafast transition to a fission of the excited singlet state into two excited triplet states. This fission seems to be plausible, as in pentacene a triplet excitation possesses less than half of the energy than a singlet excitation. Moreover, unlike the usual intersystem crossing transition of one singlet state into one triplet state (compare section 3.3.1), this transition into two triplet excitations is spin-allowed, as the two created triplet exciton have a total spin of zero. However, the transition dipole moment in pentacene is orientated along the long molecular axis of the molecule, which, for the pentacene thin film phase, corresponds to an orientation normal to the surface. As the excitation light is also orientated normal to the sample surface, this transition dipole can not be addressed by this experiment. In order to investigate triplet excitations, the measurement was repeated with an excitation light which was orientated with an angle of incidence of 65° to the normal of the sample surface. Indeed, extra features at other probe wavelengths could be observed, but the changes of the optical density were much smaller. Therefore, we argued that the creation of triplet can be assigned to the 70 fs-transition. Alternatively, we proposed, that the formation of an excimer state is responsible for the ultrafast decay [92]. Such an excimer

is created by the rotation of adjacent pentacene molecules. The transition from such an excimer state to the ground state is electric dipole forbidden as soon as the molecules are orientated in a parallel geometry [18]. Theoretical calculation by Kuhlman et. al. [95] using density functional theory together with a combined quantum mechanics and molecular mechanics approach revealed, that the rotation of pentacene molecules is energetically not favorable. They proposed, that in the first 70 *fs* the excited singlet excitation undergoes internal conversion into a double excited singlet excitation S_D , which consists of two triplet excitations of the two pentacene molecules in the unit cell, that couple to a singlet state. The transition from S_D to the ground state is forbidden by symmetry, as the symmetries of the triclinic pentacene crystal and the doubly excited state are different. This coupled state S_D can split into two independent triplets states on a timescale which is too long for an investigation by the pump and probe measurements. Therefore, the missing triplet signal after 70 *fs* does not mean, that triplet states are not finally created by illumination. Whichever model might be the most appropriate, the radiative singlet Frenkel state, that is initially excited by the light pulse, is depopulated by a transmission into a nonradiative state. This explains the low photoluminescence yield of about 10^{-7} in our measurements. Please note, that the missing triplet state signal after 70 *fs* does not necessarily mean, that triplet states are not finally created, since it is likely, that the doubly excited state S_D splits into two independent triplet states on a timescale which is too long for determination by pump and probe measurements.

7.4.3 Photoluminescence spectrum and Raman

To further gain information on the excitation states of the pentacene film, we measured the spectral light emission response of a photoexcited pentacene film, which is depicted in Figure 7.12.

The broad signal between 640 *nm* (1.95*eV*) and 720 *nm* (1.75*eV*) can be attributed to photoluminescence, arising from a radiative recombination of a Frenkel type exciton [89, 90]. As expected, it is redshifted compared to the absorption spectrum, as the singlet excitons decay into the vibrational subbands of the molecular ground state. A Davydov splitting, that was observed in the absorption spectrum, can not be resolved. This is probably due to a very fast internal conversion process. A Davydov splitting in the photoluminescence has only been observed for ultrathin pentacene cluster and was explained by a nonequilibrium exciton recombination process, which might be faster than the thermalization to the lower Davydov level [89]. However, additional sharp peaks in the spectrum can not be attributed to photoluminescence, as their characteristic width is much too small for a photoluminescence signal taken at room temperature, which corresponds to 25 *meV*. Therefore, it has to be Raman scattering modes, as their width is not broadened by the temperature, but mainly determined by the bandwidth of the excitation light, which is very small for a HeNe-laser. Compared to inorganic semiconductors, where atoms possess the lattice sites, in organic molecule crystals additional Raman modes, arising from stretching or bending of the molecular bonds, can be observed. The positions of the Raman lines have already been published by Colangeli et. al. [96]. The Raman line at 996 cm^{-1} can be assigned to an

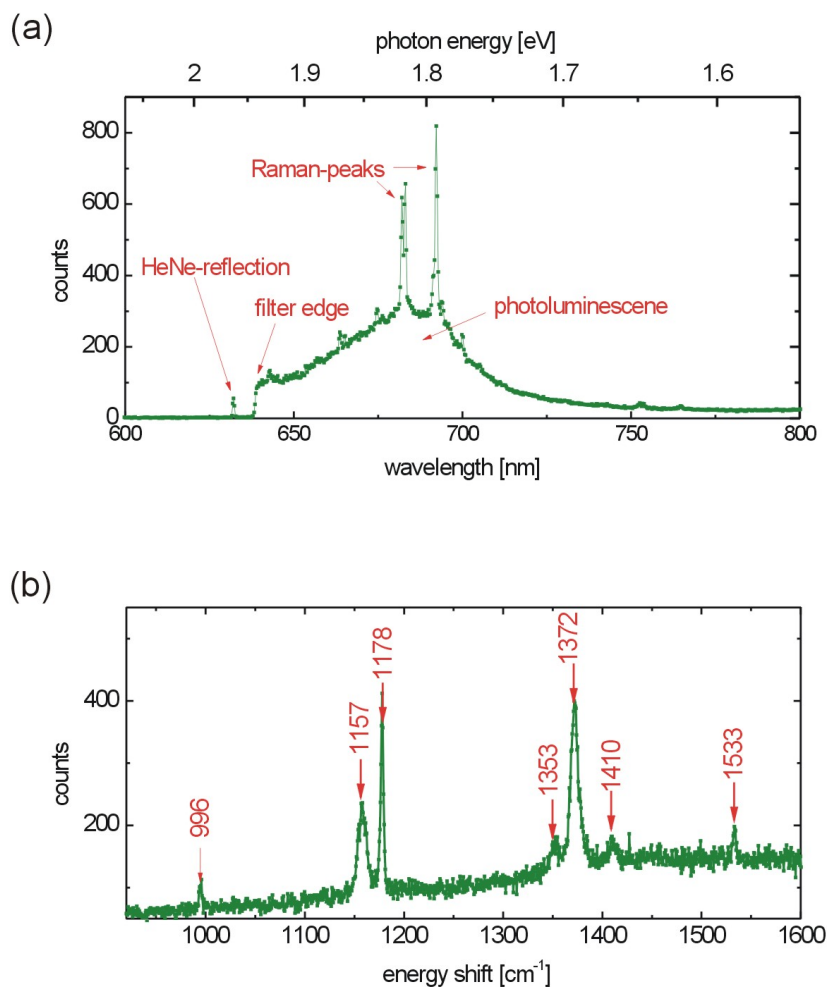


Figure 7.12: Spectral response of a 48 nm-thick pentacene film upon excitation with a HeNe-laser with an incident optical power of $1 \mu W$ and an integration time of 100 s. In (a) a grating of 150 *grooves/cm* was used. Both, the photoluminescence and different resonant Raman peaks can be observed. In (b) a grating of 1200 *grooves/cm* was used in order to evaluate the Raman excitations with a higher precision. Here, the spectrally resolved light is plotted against the energy shift with respect to the HeNe excitation wavenumber of 15802 cm^{-1} .

out-of-plane bending of the C-H bonds of the pentacene molecule, the peaks at 1157 cm^{-1} and 1178 cm^{-1} was attributed to an in-plane bending of the C-H bonds and the lines of 1353 cm^{-1} , 1372 cm^{-1} , 1410 cm^{-1} and 1533 cm^{-1} were interpreted to belong to stretching modes of the aromatic C-C bonds. Broadening or shifts of the Raman peaks can still be caused by a disordered film or interactions with the substrate at the interface, but are usually much smaller [97]. We have not yet observed variations in the Raman spectrum for different illumination spots, although the optical resolution in our setup is better than single pentacene grains. In future, it might be interesting to investigate the Raman spectra with higher accuracy in order to see differences within the single grains, or particularly deviations at grain boundaries.

7.5 Optoelectronic properties of pentacene transistors

The main purpose of our optical setup was to measure spatially resolved photoresponse at pentacene TFTs, which is defined as the change of the source-drain current caused by the illumination, see section 7.1. Here, the results of these measurements are presented and discussed.

7.5.1 Electrical response to global illumination

We investigated the response to an illumination of a large area of the transistor channel, which will be called global illumination in the following. For this purpose, we used the brightfield microscope of our setup (see section 7.2). The white LED roughly illuminated a circle with a diameter of $125\text{ }\mu\text{m}$, which was sufficient to easily cover the whole transistor length of $25\text{ }\mu\text{m}$, as it can be seen in Figure 7.6.

The change of the transconductance curves of a pentacene TFT, that is caused by global illumination, is shown in Figure 7.13. The square root of the source-drain current was plotted against the gate voltage in order to compare the threshold voltage of the device between dark and illuminated conditions. The threshold voltage under dark conditions was $V_T^{dark} = -8\text{ V}$, while the threshold voltage under global illumination can be determined to be at $V_T^{light} = -2\text{ V}$. Therefore, the threshold voltage shifted about 6 V in positive direction due to illumination. However, the mobility, which is proportional to the increase of the transconductance (also compare Figure 2.14), did not change significantly by the global illumination. For positive gate voltages, the transistor remained in the off-state if illuminated. Consequently, the general characteristics of a p-type unipolar transistor was preserved under illumination. The photoresponse, which is the difference between the source-drain current under dark conditions and under illumination, arised only from the threshold shift. A more precise look at the off-current and the subthreshold regime of the transistor, which can be read of a semilogarithmic plot of the source-drain current against the gate voltage, revealed that illumination increased the off-current by about one order of magnitude.

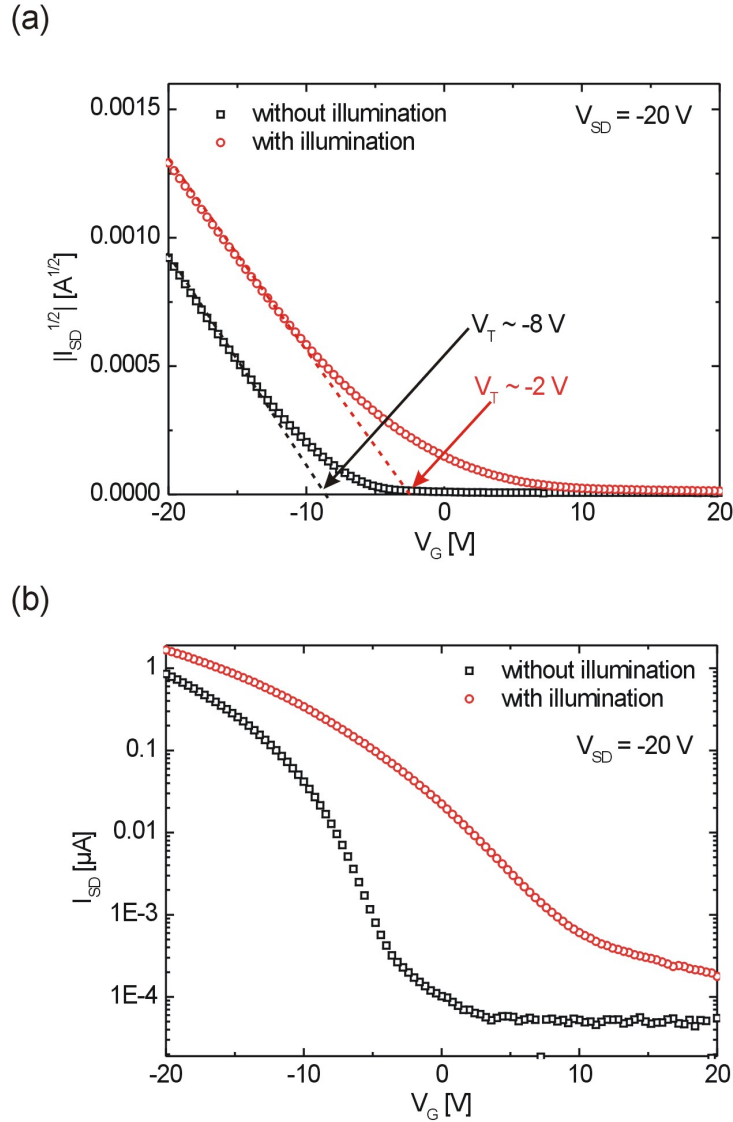


Figure 7.13: Transconductance curves in dark and with global illumination. The white LED of the brightfield microscope was used at a power of $10 \mu W$ as light source. (a) Square root of the source-drain current is plotted against the applied gate voltage at a constant source-drain voltage of $V_{SD} = -20 V$ under dark conditions and under global illumination. (b) Same data, here the source-drain current is plotted semilogarithmically against the gate voltage.

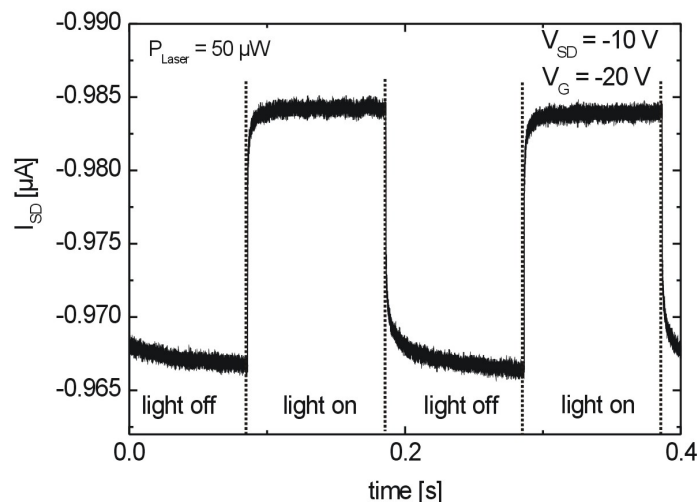


Figure 7.14: Time dependence of source-drain current under global illumination. The illumination power of the LED of the brightfield microscope was $50 \mu W$. The increase and decrease of the source-drain current upon switching the light on and off revealed a fast and a slow component of the photoresponse.

If the transistor was to be used as photo switching device, it is desirable to maximize the gain, which is the ratio between the source-drain current in the dark and the source-drain current under illumination for a constant gate voltage. This can be achieved at a gate voltage that is close to the turn-on voltage of the transistor. Utilizing the semilogarithmic plot of Figure 7.13(b), it can be seen that a gain of about 10^3 was obtained at a gate voltage of $V_G = -2 V$.

We also investigated the characteristic time scales of the photoresponse. For this purpose, we illuminated our sample with the HeNe-laser of the laser scanning microscope. We defocused the sample using the attocube positioner in z-direction in order to illuminate at least the whole transistor length from source to drain. The source-drain current was sampled by the HP 34401 multimeter using its internal buffer mode at a rate of 50000 measurements per second, while the illumination was turned on and off at a very slow frequency by the chopper.

The time evolution of the source-drain current at a source-drain voltage of $V_{SD} = -10 V$ and a gate voltage of $V_G = -20 V$ using an illumination power of $50 \mu W$ and a chopper frequency of $3 Hz$ is presented in Figure 7.14. As expected from Figure 7.13, the source-drain current increased when the transistor was illuminated and decreased when the incident light was switched off. At least two time scales of the photoresponse could be observed for both switching operations (turning on and turning off the illumination). First, a fast response was measured, which could not be resolved by the sample rate of 50000 measurements per second. Hence, this response time had to be faster than $40 \mu s$. Second, at

least one slow component of the photoresponse was observed. The typical time scale of the component was about 10 ms . The increase of the source-drain current upon illumination seemed to be slightly faster than the decrease of the current when the light was switched off.

The two different time scales indicate, that different mechanisms contributed to the photoresponse signal. Our approach to disentangle these contributions were the spatially resolved photoresponse measurements, that are presented in the following.

7.5.2 Experimental results of spatially resolved photoresponse measurements

We used our laser scanning microscope (see section 7.2) to measure the photoresponse in dependence on the position of illumination for a selected combination of source-drain voltage and gate voltage. Simultaneously, we recorded the reflection signal, which enabled us to allocate the assembled photoresponse map to the position of the source and drain contact of the TFT. Moreover, the reflection signal could be used as a sensor for focusing, as the confocal signal decreased rapidly when the sample was moved out of the focal plane during the scan. We were able to scan regions of about $50\ \mu\text{m}$ times $50\ \mu\text{m}$ without losing significant reflection signal, which was sufficient to scan from source to drain, since the usual channel length was $25\ \mu\text{m}$. A further limit of the scanning distance was also given by the hysteresis of the TFTs (see Figure 5.5). The optimization by the polymer buffer layer, which was described in section 5.3, enabled us to scan these distances without losing more than $10\% - 20\%$ of the source-drain current. To cover larger parts of the channel width it was necessary to stitch several scans together. A stitched reflection map of a bottom contact pentacene TFT is presented in Figure 7.15(a).

At x-positions of about $70\ \mu\text{m}$ and $175\ \mu\text{m}$ the sample was manually moved into the focal plane of the objective using the piezo positioner in z-direction, which resulted in the sharp signal change at these positions. The source and the drain contact could be clearly resolved in the reflection map. Moreover, the reflection signal revealed domains, which can be attributed to the different pentacene grains. In section 7.3.2, it was explained that the absorption depends on the orientation of the crystal with respect to the polarization of the incident light. The contrast of the domains is not comparable to those in Figure 7.8, as we did not control the polarization of the laser light, which in general left the fiber elliptically. In Figure 7.15(b) the photoresponse map is shown for a source-drain voltage of $V_{SD} = -5\text{ V}$ and a gate voltage of $V_G = -10\text{ V}$. As the threshold voltage of this TFT was at about -6 V , the transistor can be regarded to be in the saturation regime at these voltages. The dashed lines represent the contact edges of source and drain, which have been allocated from the reflection map of Figure 7.15(a). It is apparent, that the photoresponse was strongly enhanced towards source, which was the hole injecting contact of the transistor. The sharp vertical stripes in the map arised from the stitching and is a result of the hysteresis of the TFT. The signal is not homogeneous along the contact edge, which could be due to variations of the contact resistance. These variations might originate from the dis-

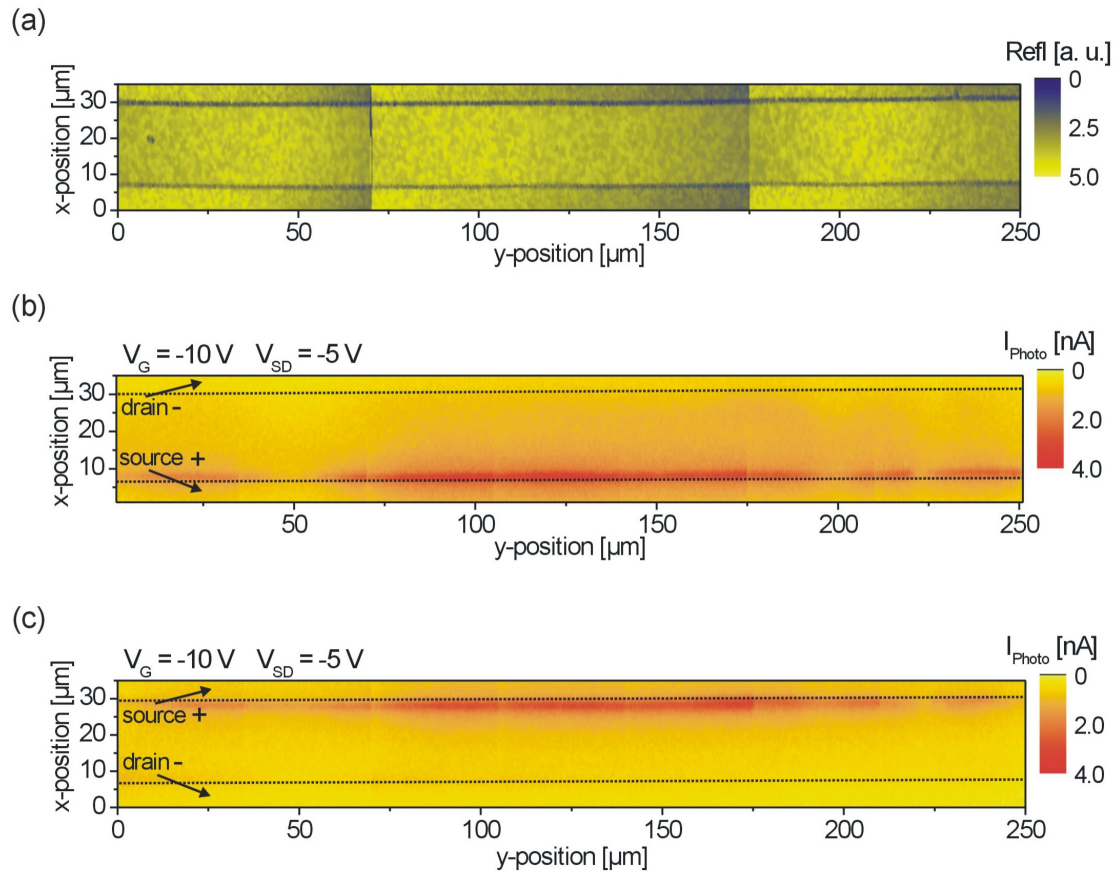


Figure 7.15: Reflection and photoresponse maps of a broad part of the pentacene transistor channel. The maps were stitched together by numerous scans. In (a) the reflection map is shown. The sharp edges at x -positions of $70 \mu\text{m}$ and $175 \mu\text{m}$ arised from manually refocusing of the sample. In (b) the photoresponse map is shown for $V_{SD} = -5 \text{ V}$ and $V_G = -10 \text{ V}$, which corresponds to the saturation regime of the transistor. In (c) a photoresponse map of the same region with the same biasing is depicted with source and drain contacts exchanged. The incident illumination power and the chopper frequency were $10 \mu\text{W}$ and 1110 Hz , respectively. Partly Adapted from [80].

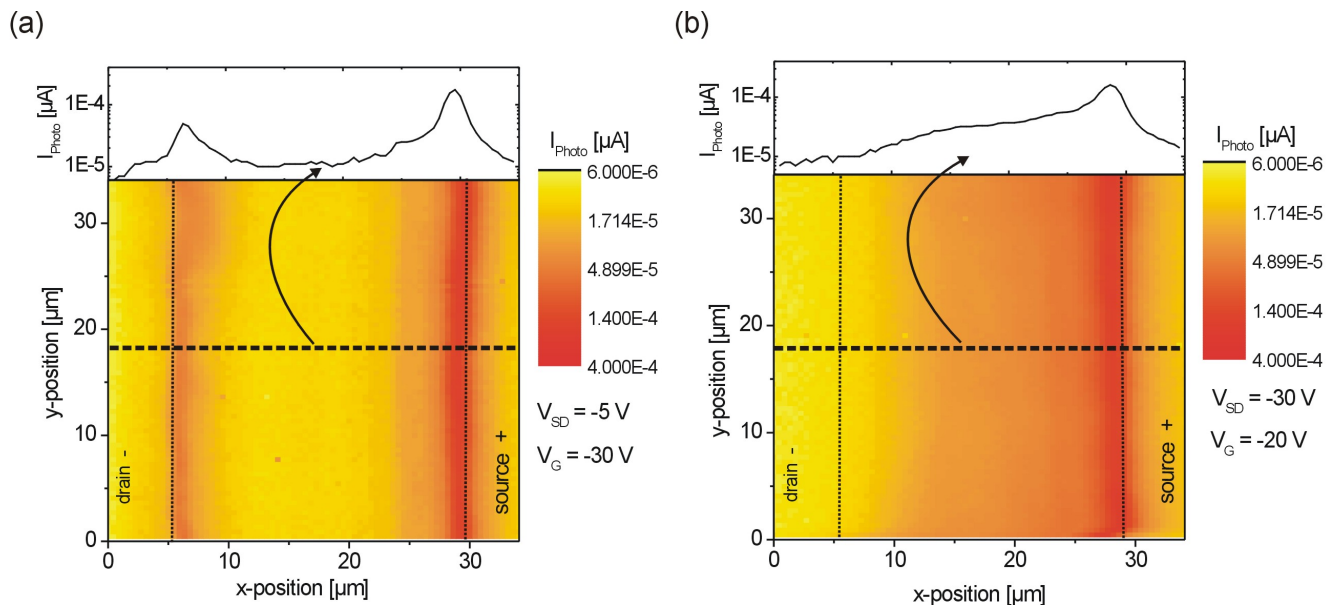


Figure 7.16: Photoresponse maps of a pentacene TFT in the linear and the saturation regime. In (a) the transistor was operated at the linear regime with $V_{\text{SD}} = -5\text{ V}$ and $V_{\text{G}} = -30\text{ V}$. Here, a photoresponse enhancement towards the source and the drain contact edge could be measured. In (b) the transistor was operated at the saturation regime with $V_{\text{SD}} = -30\text{ V}$ and $V_{\text{G}} = -20\text{ V}$. In this case, there was only an enhancement towards the source contact. On top of both maps, line cuts at the positions that are indicated in the maps are presented. The incident power of the illumination and the chopper frequency were $1\ \mu\text{W}$ and 5010 Hz , respectively. The photoresponse is plotted using a logarithmic scale.

turbed pentacene growth, that we observed adjacent to the contact edges (compare AFM micrograph in Figure 3.7). Furthermore, inside the transistor channel the photoresponse decreased with increasing distance to the source contact. At the contacts, the photoresponse decreased faster compared to the decrease within the channel, but it did not vanish completely.

The measurement was repeated at the same region of the transistor, but with the source and drain contacts interchanged (see Figure 7.15(c)). The dominant photoresponse increase moved to the other contact compared to Figure 7.15(b), i.e. the hole injecting contact for this configuration. The magnitude of the photoresponse at the source contact was about $I_{\text{Photo}} = 4\text{ nA}$ in both cases. We did not observe an increase of the photoresponse signal close to the drain contact edge.

This behavior changed qualitatively, when we operated the transistor in the linear regime, as it is shown in Figure 7.16(a). Here, photoresponse maps of a region of a pentacene TFT, that was operated at both, the linear regime and the saturation regime, are compared.

On the left, a photoresponse map at $V_{\text{SD}} = -5\text{ V}$ and $V_{\text{G}} = -30\text{ V}$ is presented, i.e.

the transistor was operated at the linear regime. On the right, the photoresponse map of the same region is plotted, but the transistor was operated at saturation using a bias combination of $V_{SD} = -30 V$ and $V_G = -20 V$. In both maps, the photoresponse signal is presented using a logarithmic scale. Cuts from source to drain, that are shown above each scan, belong to the same y -position and are indicated at the allocated maps. When the transistor was operated at the linear regime, an enhancement of photoresponse could be observed not only towards source but also towards drain, though the magnitude of the increase remained larger at the source contact edge. In contrast, the photoresponse was only enhanced towards source, when the transistor was working in saturation. The difference between the photoresponse at saturation and at linear conditions can be seen most clearly in the line cuts. When the transistor was operated at the linear regime at a low source-drain voltage of $V_{SD} = -5 V$, most of the photoresponse appeared close to the contact edges, while within the channel gap the contribution was generally low with a little tendency to higher values towards source. In contrast, when the transistor was running under saturation conditions, not even a slight increase could be observed towards the drain contact edge. In saturation, the strongest response was measured at the source contact edge as in the linear regime, but there was generally a higher contribution within the channel gap with a more distinct decrease towards the drain contact compared to the photoresponse under linear regime conditions. It is noticeable, that under both, saturation and linear conditions, the photoresponse did not vanish completely above the contacts, which was beyond the channel gap.

In order to further investigate the dependencies of the photoresponse on the position of illumination and on the applied voltages, the transistor was scanned from source to drain. For each illumination position, a complete gate voltage sweep was performed, while the source-drain voltage was kept constant. A photoresponse map of such a measurement is presented in Figure 7.17(a), where the photoresponse signal is plotted in dependence on the x -position of illumination and on the applied gate voltage at a constant source-drain voltage of $V_{SD} = -20 V$.

Several features can be observed in this map. First, a strong enhancement of the signal was measured towards the source contact for negative gate voltages. Second, an additional enhancement can be seen towards drain, but only for negative gate voltages that exceed about $-15 V$. For positive gate voltages, there is no enhancement at any scanned position, neither close to drain nor close to source. When the gate voltage was swept from positive values to negative values for a constant source-drain voltage, the transistor was switched from the off-state to the on-state. First, it was operated at the linear regime for low negative gate voltages, before it was operated at saturation for higher negative gate voltages. An enhancement at source was observed for the transistor being in the on-state, while the increase adjacent to drain only occurred in the linear regime. This is also confirmed in Figure 7.17(b), where several gate voltage sweeps of the photoresponse are presented for an illumination at different constant positions. The photoresponse signal close to source increased for negative gate voltages below $5 V$. Close to drain, the photoresponse curve showed qualitatively the same behavior, but the onset of the signal was shifted by about $15 V$ to more negative gate voltage values. The photoresponse in the midgap of the transis-

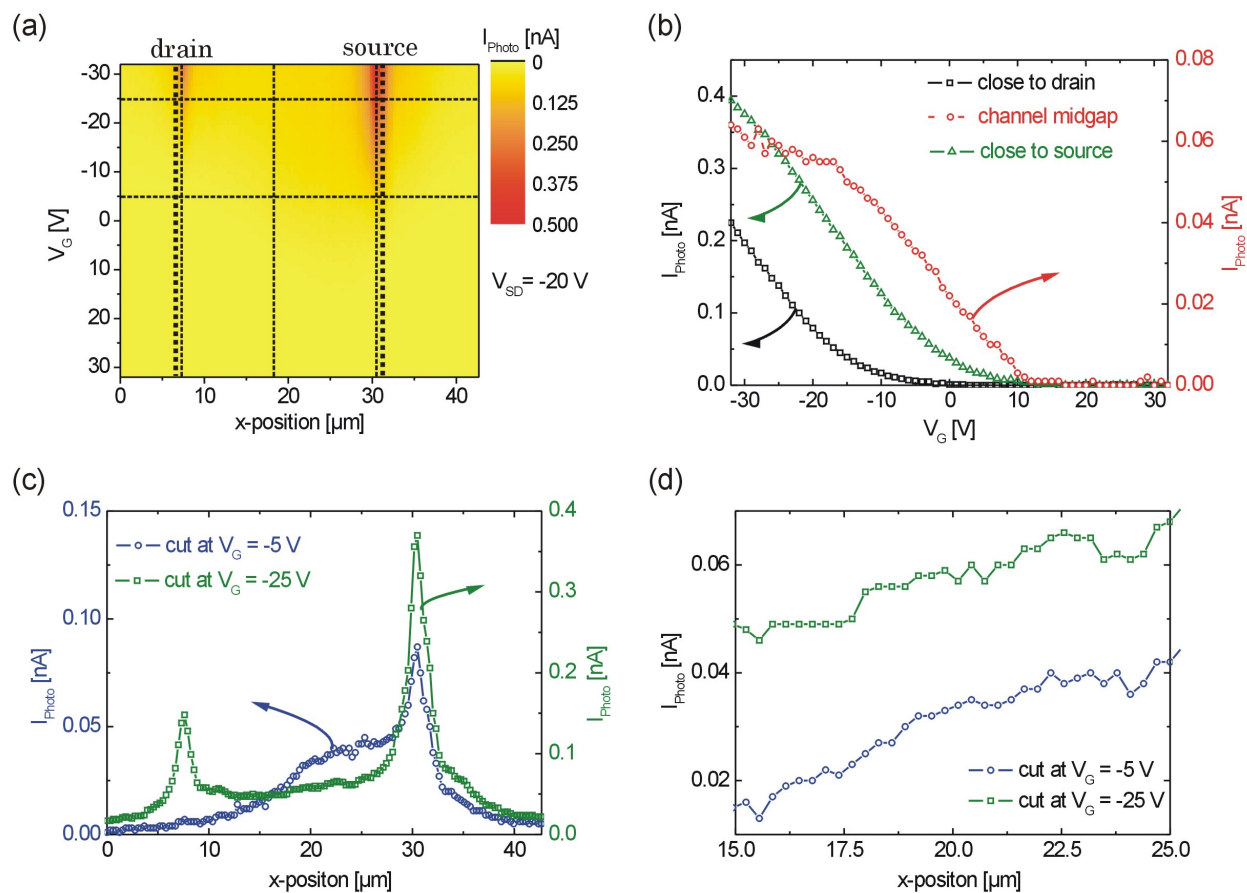


Figure 7.17: Photoresponse of a pentacene TFT in dependence on the position of illumination and on the gate voltage. In (a) a photoresponse map is presented in dependence on the x-position of the illumination by the HeNe-laser and on the applied gate voltage for a constant source-drain voltage of $V_{SD} = -20 \text{ V}$. In (b) the gate voltage dependence of the photoresponse for illumination position close to source, at the channel midgap, and close to drain are plotted. In (c) cuts of the photoresponse from source to drain for constant gate voltages of $V_G = -5 \text{ V}$ and $V_G = -25 \text{ V}$ are shown. In (d) a zoom into the middle of the channel from the data in (c) is shown.

tor channel showed qualitatively the same behavior as at source and drain, but the signal was much smaller (about a factor of ten for high gate voltages). It should be noted here, that these curves look very similar to the transconductance curves, which is the source-drain current plotted against the gate voltage, as presented in section 5.2.2 (see Figure 5.3). In Figure 7.17(c), two spatial cuts of the photoresponse from source to drain for constant gate voltages are presented, one at $V_G = -5 V$ and one at $V_G = -25 V$. Here, the transistor operated at the linear and saturation regime, respectively. Please note, that the y-axis has been scaled. The observation, that was already shown in Figure 7.16 can be confirmed. In the linear regime, an increase of the signal at both contact edges was observed, while in saturation only an enhancement towards source occurred. Within the channel, an increase of photoresponse was measured towards source. In order to show this in particular, the same cuts are presented for positions close to the midgap of the channel and with one common y-axis. It is apparent, that the photoresponse increased towards source with a very similar slope for both gate voltages.

So far, only measurements at constant chopper frequencies have been presented. Since we observed different time scales at a global illumination (see Figure 7.14), we have also investigated the spatially resolved photoresponse in dependence on different chopper frequencies. We measured the photoresponse signal for different frequencies while sweeping from source to drain at constant voltages. In Figure 7.18, these measurements are presented for chopper frequencies between $2 Hz$ and $5010 Hz$. We did not choose multiples of $50 Hz$ in order to avoid resonance with the power supply voltage of our devices. Within the signal range between $20 Hz$ and $110 Hz$, we could not avoid resonance phenomena at all, therefore frequencies in this range are omitted.

The measurements at different frequencies revealed two different contributions to the photoresponse signal. First, a slow component throughout the whole device could be detected. The time scale of this component was about $10 ms$, i.e. the signal increased rapidly below a frequency of $100 Hz$. Within the channel, this component increased towards source. This increase was less pronounced, if the transistor was operated at the saturation regime with $V_{SD} = -5 V$ and $V_G = -30 V$ (see Figure 7.18(a)) than for a voltage combination of $V_{SD} = -30 V$ and $V_G = -20 V$ (see Figure 7.18(b)), which belongs to the saturation regime of the TFT. This confirms the observations shown in Figure 7.16 and Figure 7.17. Outside of the transistor channel, which corresponds to positions directly above the source and drain contacts, the slow component decreased but did not vanish completely. This can be seen most clearly for very slow frequencies. For a frequency of $2 Hz$, the photoresponse decreased by only about 20% with respect to the value within the channel. Second, a much faster component of the photoresponse was observed, but only adjacent to the source contact edge, if the TFT was measured under saturation conditions. An additional, though much smaller, contribution to the fast response could be measured adjacent to the drain contact edge, if the transistor was operated at the linear regime. The peaks of the fast photoresponse component were centered at the edges of the contacts and the signal decreased with a very similar slope towards the transistor channel and towards the contacts. Assuming a Gaussian shape, the width of the peaks could be determined to be about $2 \mu m$.

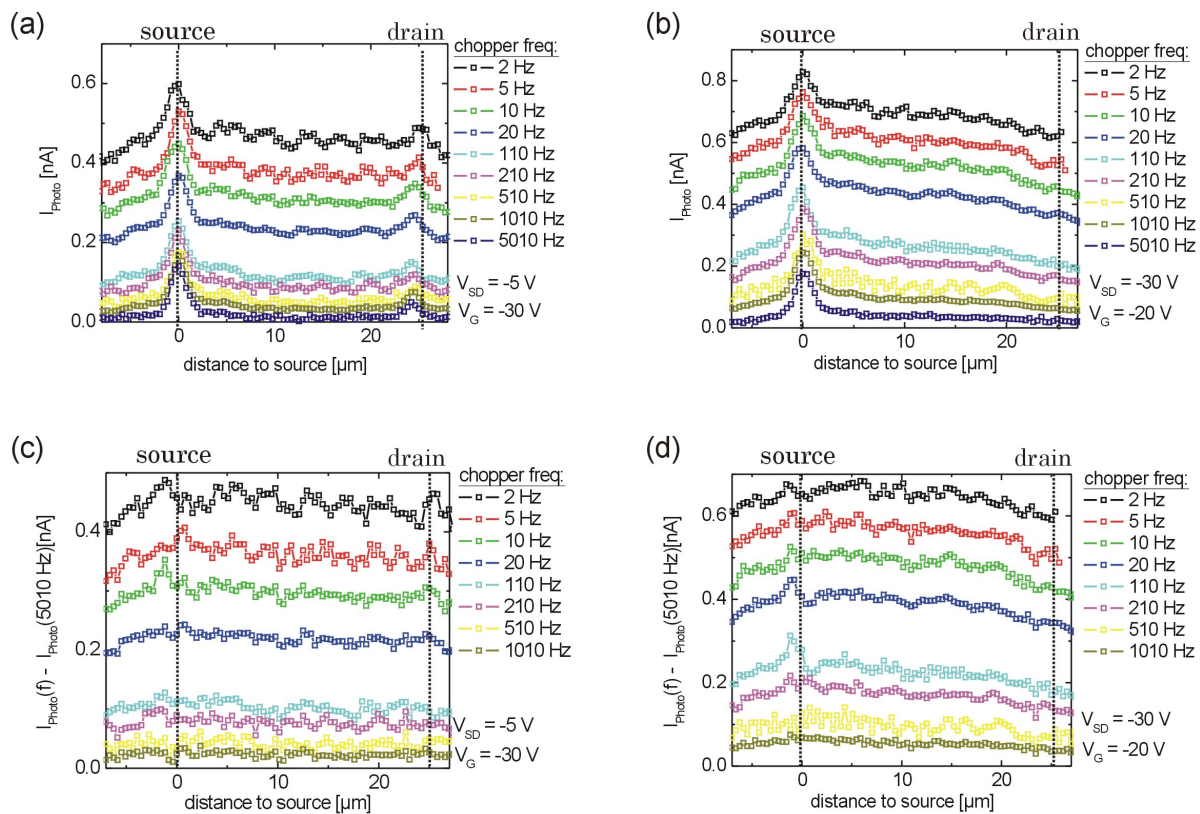


Figure 7.18: Photoresponse of a pentacene TFT for different chopper frequencies scanned from source to drain. In (a) the photoresponse is plotted against the x-position of illumination for several chopper frequencies between 2 Hz and 5010 Hz , while the transistor was operated at the linear regime with $V_{SD} = -5\text{ V}$ and $V_G = -30\text{ V}$. In (b) the measurements were performed with the transistor operating in saturation at voltages of $V_{SD} = -30\text{ V}$ and $V_G = -20\text{ V}$. In (c) the difference between the photoresponse for several chopper frequencies and the signal at the highest frequency of 5010 Hz , that is shown in (a), is plotted. In (d) this difference for the measurements at (b) is presented. The power of the incident light was $1\text{ }\mu\text{W}$ for all presented measurements. Dashed lines indicate the edge of the source and drain contacts.

In Figure 7.18(c) and 7.18(d), the photoresponse signal at the highest chopper frequency at 5010 Hz has been subtracted from the remaining photoresponse signals of Figures 7.18(a) and 7.18(b), respectively. These illustrations demonstrate, that the enhancement adjacent to the contact edges is only due to the fast photoresponse component, while the slow component is not significantly altered there. Otherwise, this difference signal would not be constant adjacent to the contact edges.

In the end of the PhD-thesis, we enhanced our time resolution to up to 200 kHz . We used a laser diode with a wavelength of 635 nm as illumination source (see Figure 7.3), that could be modulated electronically. Even at a frequency of 200 kHz , we did not observe a reduction of the fast photoresponse component at the contact edges.

7.5.3 Discussion of spatially resolved photoresponse measurements

Overview of experimental results

A model for the photoresponse mechanism must agree with the experimental observations that have been presented above. The main results of our experiments are itemized in the following:

- there were photoresponse components with two different time scales
- the characteristic time scale of the slow photoresponse component was about 10 ms
- the characteristic time scale of the fast photoresponse component was less than 5 μs
- the slow photoresponse contribution was detected throughout the whole device, even above the contacts outside of the transistor channel, and increased towards the source contact edge
- the fast photoresponse contribution was detected adjacent to the source contact edge and drain contact edge when the TFT was operated at the linear regime, but only adjacent to the source contact edge when the transistor was in the saturation regime
- both photoresponse components increased similar to the source-drain current with increasing negative gate voltage

Schematic diagrams of these observations are presented in Figure 7.19.

In the following, a model is developed to explain the observed phenomena.

Slow photoresponse component-hole detrapping mechanism

Pentacene shows p-conducting behavior, as shown in chapter 5. This means that under dark conditions, charge carriers that contribute to the source-drain current are holes. Using suited contacts for electron injection and other dielectrics, it was demonstrated that pentacene can also show n-conduction behavior, though the reported mobility for electrons was

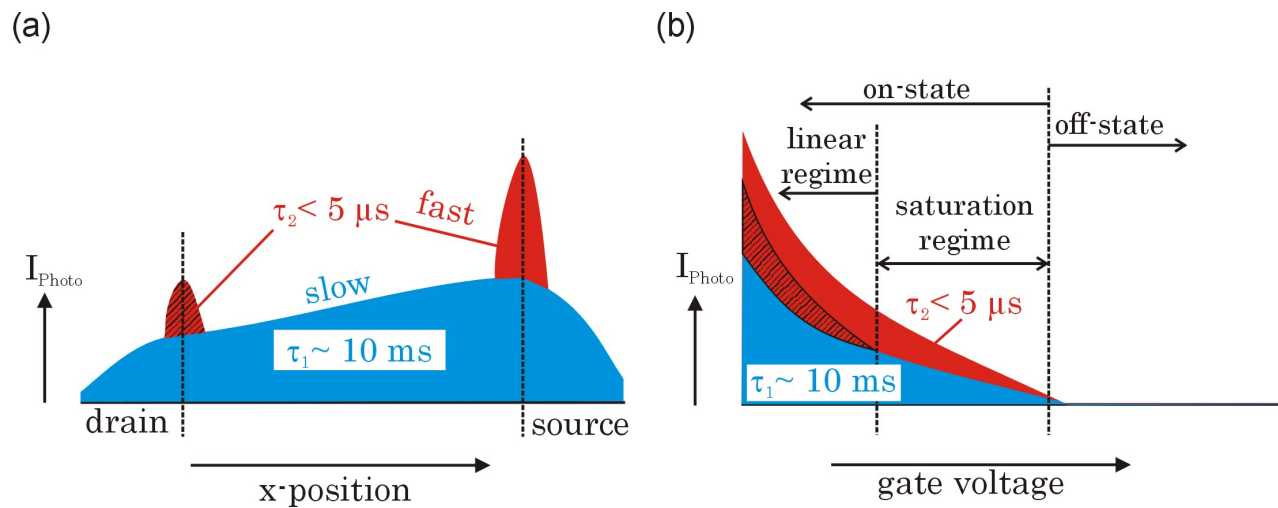


Figure 7.19: Schematic survey of the photoresponse phenomena. In (a) the photoresponse contributions are sketched in dependence on the x -position of illumination. In (b) the photoresponse is sketched in dependence on the gate voltage. The blue areas represent the slow photoresponse component with a time scale of roughly 10 ms . The red areas represent the fast photoresponse components with a time scale of less than $5 \mu\text{s}$, with the clear area corresponding to the photoresponse measured close to source and the shaded area corresponding to the photoresponse measured close to drain, which was only detected when the TFT was operated at the linear regime.

usually much lower [88,98]. Nevertheless, it can not be excluded in general, that electrons are mobile in our devices as well. Therefore, one may hypothesize that the measured photoresponse signal was due to photocurrent. In the case of photocurrent, the excitons, that are created by the incident light, are separated into free charge carriers. Subsequently, the electrons and holes drift to the source and drain contacts, respectively. This results in an increase of the source-drain current, which would cause a photoresponse signal. However, photoresponse, which is triggered by this mechanism, should occur when the transistor is operated in both, the on- and the off-state. The gate voltage, which changes the amount of accumulation of field effect induced holes, should not influence the photocurrent in general. Only comparatively small variations, which can be due to nonideal transport behavior effects such as field dependent mobilities, could be expected. In contrast, our experiments demonstrated, that the photoresponse showed a very strong dependence on the applied gate voltage. When the TFT was operated in the off-state, no photoresponse was observed (compare Figure 7.17). Therefore, photocurrent can be excluded to dominate our photoresponse signal.

The mechanism, that triggered the slow photoresponse component, must agree with an increasing response towards negative gate voltages. The dependence of the photoresponse and the source-drain current on the applied gate voltage at an illumination spot in the midgap are compared in Figure 7.20. It is apparent, that the photoresponse signal behaved qualitatively similar to the source-drain current but with two differences. First, the onset of the photoresponse signal is at a more positive gate voltage compared to the onset of the source-drain current. Second, the photoresponse shows a more distinct saturation behavior for increasing negative gate voltages.

The source-drain current rises due to an increase of accumulated holes towards more negative gate voltages, which is caused by the upward bending of the valence band, as it was explained in section 2.2. However, the transport properties of pentacene are also highly influenced by trap states above the valence band (see also Figure 3.5). The influence of these trap state on our transistors was already explained and discussed in section 5.3. The trap states consume free holes leading to a reduction of the source-drain current. In the case of deep trap states, this leads to a shift of the threshold voltage, while shallow trap states are responsible for hysteresis. The energies of the trap states are fixed with respect to the valence band edge. Therefore, the amount of traps, that is filled with holes, depends on the gate voltage as it is the case for the amount of free holes within the valence band. This is sketched in Figure 7.21.

If the gate voltage is positive, the valence band is bent downward. Consequently, the trap state energy levels for holes are also lowered and no additional holes get trapped. However, if the gate voltage is negative, the valence band is bent upward. In this case, the hole trap levels are lifted above the Fermi energy, which leads to additional hole trapping. This already occurs at a gate voltage which is not sufficient for accumulation of free holes, since the trap states are above the states for free holes in the valence band. For higher negative gate voltages, more trap states get filled and free holes are accumulated as the valence band crosses the Fermi energy. In summary, the amount of trapped holes shows a very similar gate voltage dependence as the amount of accumulated free holes, that carry the

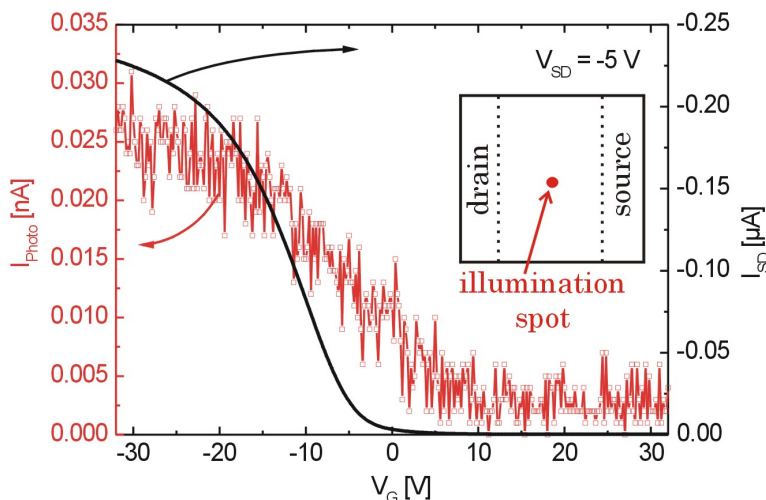


Figure 7.20: Gate voltage dependence of slow photoresponse component. The photoresponse signal (red) and the source-drain current (black) are plotted against the gate voltage for a constant source-drain voltage of $V_{SD} = -5$ V at an illumination spot in the midgap of the transistor channel and an incident laser power of $1 \mu\text{W}$.

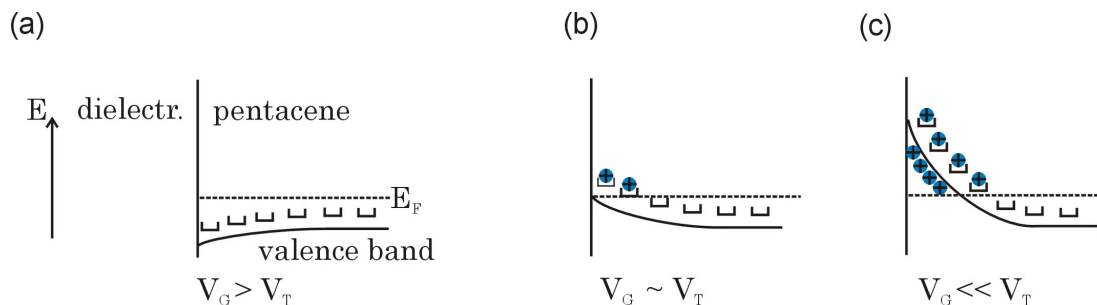


Figure 7.21: Schematic of the dependence of hole trap filling and mobile hole accumulation on the gate voltage. In (a) the gate voltage is positive and no hole traps are filled. In (b) the gate voltage is negative. A few trap states are filled by holes, but no free holes are accumulated, since the gate voltage induced valence band bending is only sufficient to lift some trap states above the Fermi energy, but not valence band states. In (c) the gate voltage is sufficiently negative to create free holes in addition to an increased amount of trapped holes.

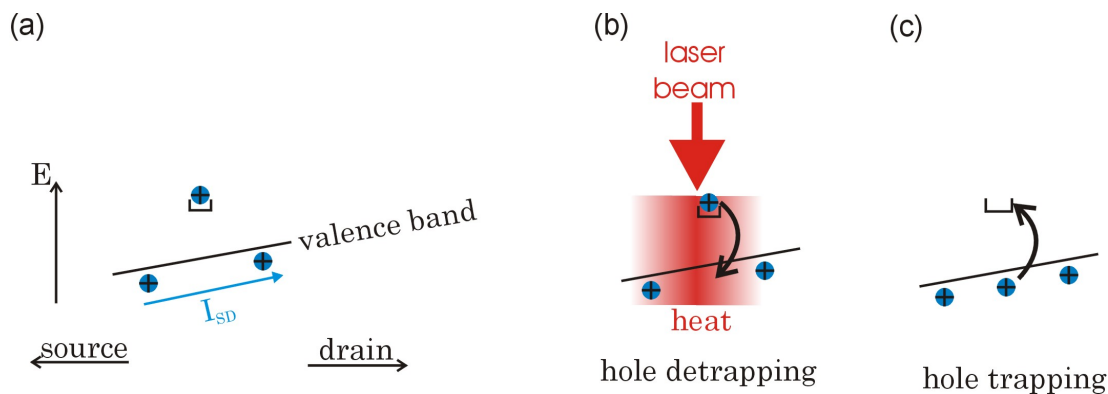


Figure 7.22: Schematic of the mechanism of the slow photoresponse component. In (a) the equilibrium situation is sketched with free holes flowing from source to drain in the valence band and a hole being trapped under dark conditions. In (b) the hole gets detrapped due to heating of the sample, which is caused by the incident laser light. In (c) the light is switched off, which results in retrapping of a hole by the previously emptied trap.

source-drain current.

The observed gate voltage dependence of the photoresponse can be explained with a laser induced detrapping mechanism, that is depicted in Figure 7.22. Under dark conditions, the transistor is in an equilibrium condition between mobile holes flowing from source to drain in the valence band and immobile holes, which are located in traps at energy levels above the Fermi energy. Trapped holes, which are located sufficiently high above the valence band edge, cannot be released. In the case of room temperature, this corresponds to about $k_B T = 25 \text{ meV}$, with k_B and T being the Boltzmann constant and the temperature, respectively. When a laser is focused at the sample, light gets absorbed and heats the sample. This heating provides energy, that may release traps in the pentacene film. Additional free charges are created in the transistor channel and the ratio between immobile charges and free charges reduces. Consequently, the source-drain current is increased and a photoresponse can be detected. It is important to notice, that the light does not necessarily need to be absorbed within the pentacene film as heat, that is produced in the substrate, can be transferred into the pentacene film as well. When the light is switched off, the transistor cools down and the trap states can be refilled. Thus, the density of free holes and therefore the source-drain current get reduced to the original value and the transistor operates back in equilibrium condition.

This bolometric effect agrees with the observed gate voltage dependence, since the photoresponse signal is proportional to the amount of trapped holes. As explained above (see Figure 7.21), the density of trapped holes has a similar gate voltage dependence as the density of free holes, therefore it is not surprising, that the photoresponse and the source-drain current showed similar gate voltage dependencies, as shown in Figure 7.20. This mechanism also explains, why the onset of the photoresponse signal was at a more positive gate voltage than the onset of the source-drain current, since the trap states are located above the valence band edge. Thus, these state were already lifted above the Fermi

level at gate voltages, which were not negative enough to accumulate free holes, since the valence band had not crossed the Fermi level yet (compare Figure 7.21(b)). The saturation behavior of the photoresponse at high negative gate voltages was due to a limited amount of traps that could be additionally filled by holes with increasing negative gate voltage. As it was shown by our in-situ measurements, the Debye length of our transistor corresponded to about three monolayers (see section 6.3.2). Hence, the reservoir of traps, that can be filled by band bending caused by the gate voltage, is limited. The photoresponse can not be increased by the gate voltage any more as soon as all traps at a certain location of the channel are filled.

The slow photoresponse component increased from source to drain, as shown in Figure 7.17. This can be explained with the gate voltage dependence as well. As it was described in section 2.3.1, the band bending at a certain position within the transistor channel does not only depend on the applied gate voltage, but also on the distance to the source contact. This is due to the source-drain voltage, which causes a potential gradient across the channel. This means for a negative source-drain voltage, that the potential difference between the gate electrode and a specific spot within the transistor channel, which will be called effective local gate voltage in the following, decreases towards drain, as it was depicted in Figure 2.12. Consequently, for a given set of applied voltages, the upward band bending as well as the amount of trapped holes increased towards source. Therefore, the photoresponse increased when the illumination spot was moved from drain to source. In order to investigate the dependence on the source-drain voltage and on the position of illumination more closely, plots of the photoresponse cuts from drain to source for various applied source-drain voltages are presented in Figure 7.23.

Here, the trend of the photoresponse signal in the middle of the transistor channel is discussed. The slope of the photoresponse increase towards source was small for low source-drain voltages, i.e. in the linear regime for $V_{SD} = -1\text{ V}$ – $V_{SD} = -10\text{ V}$ compared to larger source-drain voltages corresponding to the saturation regime at $V_{SD} = -20\text{ V}$, $V_{SD} = -30\text{ V}$. This is not surprising, since the gradient of the potential within the transistor channel increases with increasing source-drain voltages, especially in the saturation regime, which corresponds to gate voltages beyond $V_G = -15\text{ V}$ (cf. Figure 2.12).

Beyond bolometric effects, the gate voltage dependence and the spatial dependence of the photoresponse could be related to an electronic process within the pentacene layer. As it was explained in section 7.3, Frenkel excitons can be created in pentacene by absorption of light in the film. The low photoluminescence yield, that we observed, was interpreted by a fast fission process of one singlet exciton into two triplet excitons. These triplet excitons diffuse within the pentacene layer and recombine. In this recombination process, energy is released and an adjacent hole trap could be emptied. This process was already proposed in 1962 by Helfrich et. al. [4]. The lifetime of triplet excitons is usually in the range of microseconds. Therefore, the photoresponse, which is caused by such a process, should also have a characteristic time scale of microseconds and can not explain the much longer time scale of about 10 ms , as observed (compare Figure 7.18). In contrast, these long time scales are typical for bolometric effects and were already reported for completely different systems, such as carbon nanotubes [99]. Recombination of triplet excitons, that have been

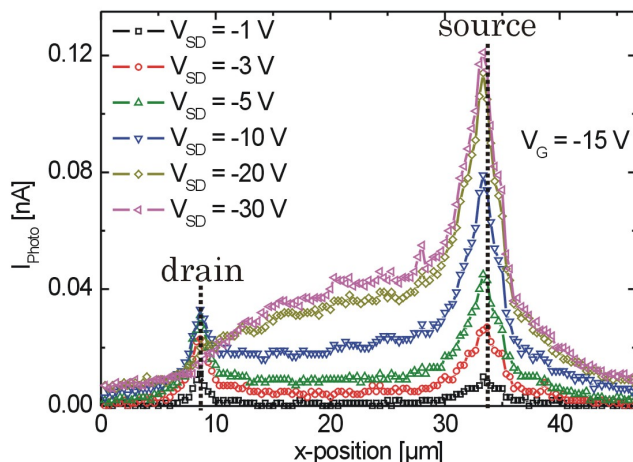


Figure 7.23: Spatial dependence of the photoresponse for various source-drain voltages. The photoresponse is plotted against the position of illumination from drain to source. The illumination power of the HeNe-laser was $1 \mu W$. The transistor was operated at a gate voltage of $V_G = -15 V$. Curves are shown for various source-drain voltages of $V_{SD} = -1 V$, $V_{SD} = -3 V$, $V_{SD} = -5 V$, $V_{SD} = -10 V$, $V_{SD} = -20 V$, and $V_{SD} = -30 V$.

created in the film, has probably a very similar heating effect compared to absorption elsewhere in our samples.

Now, we discuss how this interpretation relates to the Davydov splitting, i.e. the polarization dependent absorption of the S_0 excitation. Photoresponse maps for illumination with perpendicular polarization are shown in Figure 7.24. This sample, which was prepared by C. Westermeier, was a top contact device (compare Figure 2.11) and showed pronounced photoresponse in the middle of the channel. At a first glance, one could assume, that the variations of the photoresponse signal is due to a varying absorption of the pentacene grains, as it was demonstrated in Figure 7.8. However, areas of increased photoresponse were identical for an incident light polarization of 0° and 90° . This is in contrast to the reflection maps, where grains with increased absorption for a polarization 0° showed particular low absorption for a polarization of 90° and vice versa. This is not surprising, since most of the light is absorbed in the substrate, and the total reflection is only altered a little bit by the varying absorption of the pentacene film (see Figure 7.8(d)). Therefore, the absorbed energy in the sample can be assumed to be rather uniform. Whether light is absorbed in the silicon substrate or in the pentacene film is not crucial, since the generated heat can be transferred efficiently over small distances. Consequently, we think that the significant spatial variations of the photoresponse did not primarily originate from varying absorption within the pentacene film but were due to different trap densities. Areas with large trap densities can release more traps than regions with less traps. In turn, the photoresponse signal maps the trap densities of the pentacene film.

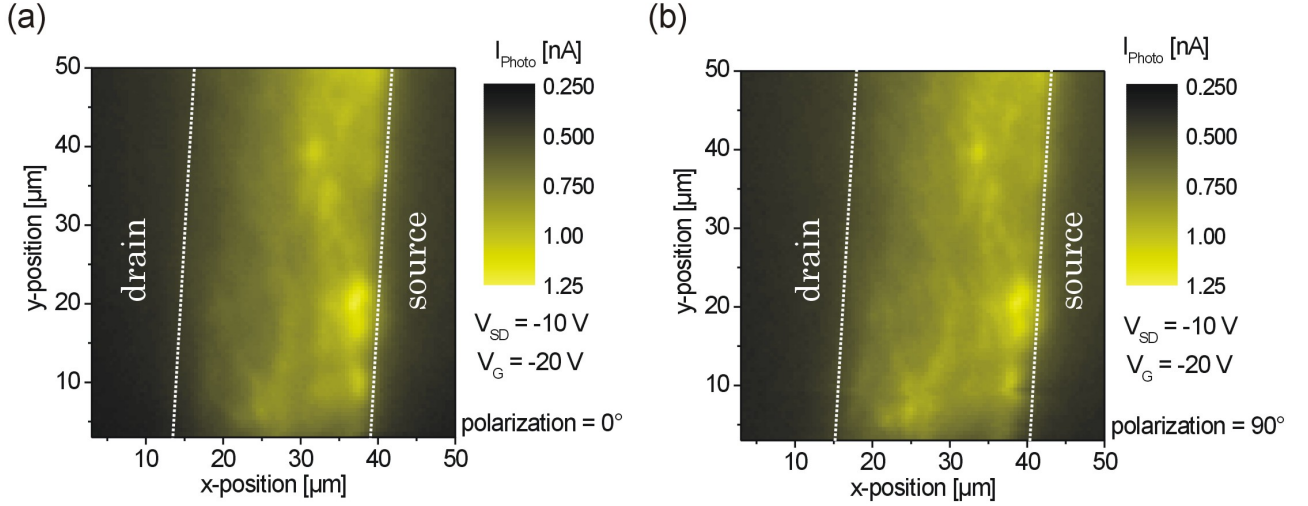


Figure 7.24: Photoresponse maps for different polarizations of the incident HeNe-laser light. In (a) the photoresponse map is shown for a linear polarization of 0° , while in (b) the photoresponse of the same area is plotted for an incident light polarization of 90° . The incident laser power was $1 \mu W$ and the applied voltages were $V_{SD} = -10 V$ and $V_G = -20 V$ in both cases. Here, the pentacene transistor was a top contact device. Adapted from [79].

Another clear indication, that heating triggered the photoresponse, can be seen in Figure 7.18. The photoresponse did not vanish, even if the illumination was above the contact quite far away from the contact edge. In Figure 7.18(a), for a frequency of $2 Hz$, the slow photoresponse component decreased from about $0.5 nA$ to $0.4 nA$, when the illumination was moved from the source contact edge to about $5 \mu m$ away from the edge above the source contact. Even in the case of top contact devices, similar behavior could be observed by C. Westermeier [79].

The amount of detrapped holes will be estimated in the following. The light induced increase of the average area density of free holes ΔN_h is the difference of the free hole density between illuminated and dark conditions. Using equation (5.2) for the free hole density, I_{SD}/V_{SD} and $(I_{SD} + I_{Photo})/V_{SD}$ for the resistance under dark $R(\text{dark})$ and under illuminated $R(\text{illum.})$ conditions, respectively, we obtain

$$\Delta N_h(\text{detrapped}) = N_h(\text{illum.}) - N_h(\text{dark}) = \frac{L}{e\mu WR(\text{illum.})} - \frac{L}{e\mu WR(\text{dark})} = \frac{LI_{Photo}}{e\mu WV_{SD}}. \quad (7.3)$$

Here, it was assumed, that the mobility was the same for illuminated and dark conditions, as the slope of the transconductance curves were very similar even if a large area of the transistor channel was illuminated (see Figure 7.13). In Figure 7.18(a), the slow photoresponse component was about $5 \cdot 10^{-10} A$ at $V_G = -30 V$ and $V_{SD} = -5 V$ for the lowest chopper frequency of $2 Hz$. The linear regime is most suited for such an estimation, because

the hole density is quite constant throughout the whole TFT channel. With a mobility of about $10^{-3} \text{cm}^2/(\text{Vs})$, a channel length and width of $25 \mu\text{m}$ and $1000 \mu\text{m}$, respectively, an additional average hole density of $\Delta N_h = 1.6 \cdot 10^{10} \text{cm}^{-2}$ is obtained throughout the whole device. However, the illuminated spot was only about $1 \mu\text{m}^2$, which was much less than the whole transistor channel area of $W \cdot L = 2.5 \cdot 10^4 \mu\text{m}^2$. If we assume, that every trap in the illuminated area released one hole contributing to the source-drain current, then a density of traps of $4 \cdot 10^{14} \text{cm}^{-2}$ would be obtained. This seems to be too high compared to the density of pentacene molecules, which is $4.4 \cdot 10^{14}$ molecules/monolayer. Taking the small Debye length of about three monolayers into account, this means, that nearly every pentacene molecule would act as a hole trap, which seems to be unrealistic. In contrast, if we assume that the trap density is about $10^{11} \text{cm}^{-2} - 10^{12} \text{cm}^{-2}$, as obtained from the hysteresis and the threshold voltage shift, then the filled traps, that released holes, would have covered a region of about $10^3 \mu\text{m}^2$, which is about 5% of the whole transistor area. This is in agreement with the bolometric interpretation of trap release and the slow spatial decrease of the photoresponse above the contacts.

Some experiments for the future could proof the bolometric mechanism of the photoresponse within the channel. It could be observed, if the photoresponse depends on the thickness of the pentacene film, as this varies the absorption within the semiconductor. If the photoresponse is rather independent of the thickness, this is further indication of the proposed heating mechanism. As transistors show sample to sample variations, this could be done most precisely, if a thickness gradient could be evaporated and the thickness dependent measurements could be performed at one single TFT. A similar proof could be done, if a long wavelength of the incident light is used, so that pentacene is transparent (compare Figure 7.7). Thus, the whole energy of the light is deposited in the substrate, but the photoresponse should not vanish. In contrast, a decrease of the photoresponse would be expected, if a transparent substrate such as glass was used.

Fast photoresponse component - triplet assisted hole detrapping

The fast photoresponse component, observed adjacent to the contacts, can not be explained by a bolometric effect, as timescales below $5 \mu\text{s}$ are far too fast for this mechanism. Timescales in the nanosecond or microsecond regime are more typical for electronic processes, occurring within the pentacene film in our case. This fast mechanism was only observed at the contact edges. This suggests that the fast photoresponse component was due to the high electric fields, which exist at metal-semiconductor interfaces, as it was explained in section 2.1. Experimentally, these high electric fields at the contacts of an organic transistor were observed by Buergi et. al. [54], who have conducted Kelvin probe force microscopy measurements at poly(3-hexylthiophene) transistors. Measured potential profiles for various source-drain and gate voltages are shown in Figure 7.25.

These measurements reveal that voltage drops of at least 1V are typical at the contacts. Using $\epsilon_s = 3$ and $N_a = 3 \cdot 10^{17} \text{cm}^{-3}$, which has been reported for pentacene [?], this results in an electric field of about 10^6V/cm , as it can be seen in Figure 2.3 for an ideal metal-semiconductor junction. Additionally, one has to take into account, that pentacene does

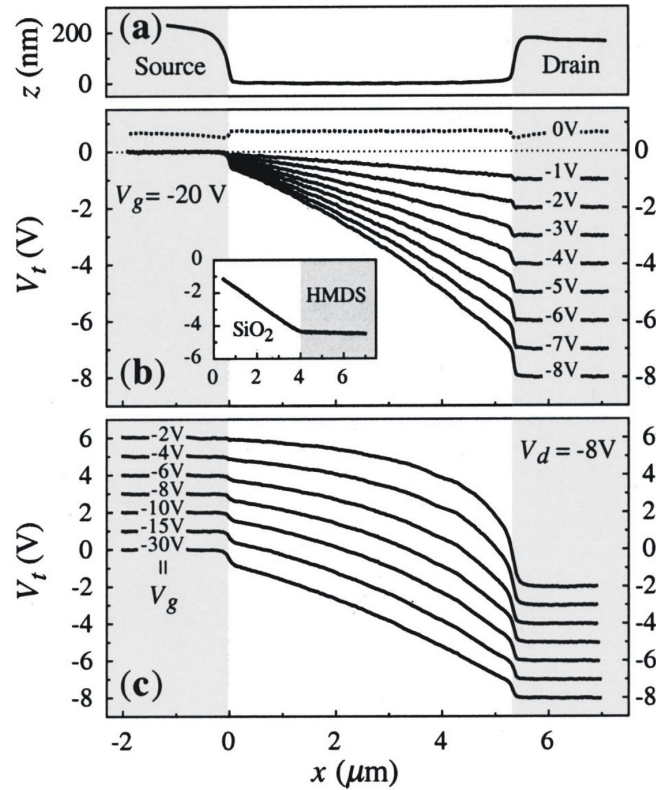


Figure 7.25: Potential profiles measured by Kelvin probe force microscopy. In (a) a topographic profile of the poly(3-hexylthiophene) transistor is shown. In (b) the potential profiles are depicted for a constant gate voltage of $V_G = -20$ V and different source-drain voltages between $V_{SD} = -1$ V and $V_{SD} = -8$ V. In (c) potential profiles for a constant source-drain voltage of $V_{SD} = -8$ V and different gate voltages between $V_G = -2$ V and $V_G = -30$ V are presented. Potential drops of about 1 V at the contacts were observed. Adapted from [54].

not grow nicely on gold (see section 3.4), probably leading to even further enhanced electric fields at the contact edges. We think, that these high electric fields are sufficient to separate an exciton, that has been created by the incident light, into an electron and a hole. The electron is not very mobile in pentacene and gets subsequently trapped, or in other words a hole is released from a trap by the electron, similar to the slow photoresponse mechanism. This hole is mobile, hence an excess charge is created, the source-drain current is increased, and photoresponse can be detected. As soon as the hole trap gets refilled, the photoresponse signal vanishes. This mechanism can only occur, if sufficient holes are trapped, which is gate dependent as it was explained in the case of the slow photoresponse mechanism. If no hole traps can be detrapped, the electrons can not be trapped and recombine directly with a mobile hole. Hence, the amount of free holes does not change and the source-drain current is not altered. Consequently, it is not surprising, that the gate-dependence of the slow and the fast component of the photoresponse were very similar. There might be an additional effect of the detrapping at the contact edges, that was proposed by Tsen et. al. [100]. They regarded the trapped electrons as p-dopants that increased the hole concentration. Due to equation (2.10), an increase of the doping concentration leads to a decrease of the depletion width (also see Figure 2.3). This finally results in a decrease of the contact resistance. This effect can also contribute to the photoresponse signal at the contact, but it probably does not explain the gate voltage dependence. Finally, photocurrent can also be excluded for the fast photoresponse component, since this would result in a photovoltage, as it is the case for photodiodes. We did not observe this, as we did not resolve photoresponse for $V_{SD} = 0 V$.

So far, the mechanism described above can explain the fast photoresponse at source and drain, observed in the linear regime. In saturation, this contribution vanished at the drain electrode (see Figure 7.16). We think, that this is a pinch-off phenomena. When the transistor is operated at saturation, holes are only accumulated between the source contact and the pinch-off point, as it was explained in section 2.3.2 (see also Figure 2.12). Beyond the pinch-off point, there is no accumulation channel as the effective local gate voltage does not bend the valence band across the Fermi level. The hole traps are also not filled, if the gate voltage is further increased (compare Figure 7.21(a)). Under these conditions, trapping does not work, as it was already explained above for the slow photoresponse component.

The discussion above suggests that a fast photoresponse is detected, if an exciton arrives at the metal-semiconductor junction. The width of the metal-semiconductor junction, where the electric field is highly enhanced, is confined to usually less than $100 nm$, as shown in Figure 2.3. In Figure 7.26, it can be seen that the fast photoresponse component could be fitted by a Gauss function with a width of typically $\sigma = 2 \mu m$.

In contrast, the width of the luminescence signal was about $0.5 \mu m$, which could be measured by the CCD-camera and is depicted as inset of Figure 7.26. As it was explained in section 7.4.2, luminescence is caused by the recombination of singlet excitons. These excitons have a very short lifetime of $70 fs$ in pentacene. Therefore, their diffusion length is less than a nanometer and can not be resolved by our experiments. Hence, the luminescence signal is not broadened and the spot of the CCD-camera can be interpreted to be

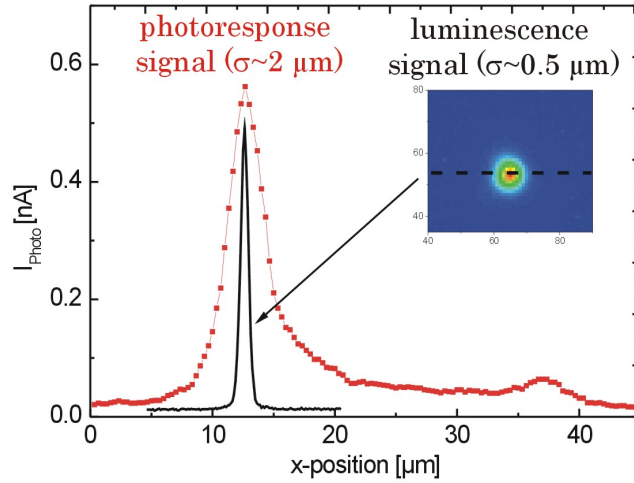


Figure 7.26: Comparison of the width of the laser spot, detected by the CCD-camera, with the photoresponse signal. The fast photoresponse component can be fitted by a Gauss function with a width of $2 \mu\text{m}$, while the spot of illumination could be fitted by a Gauss function with a width of about $0.5 \mu\text{m}$

of the same size as our illumination spot. It was also argued, that the low luminescence yield is due to a very high intersystem crossing rate from singlet excitons to triplet excitons in pentacene, since one singlet exciton has twice the energy of a triplet exciton and the transition into doubly excited triplet states forming a singlet state is not spin forbidden (also see [92,94]). Compared to singlet excitons, triplet excitons have much larger lifetimes, as it was explained in section 3.2.2 (also compare Figure 3.3). The results of the pump and probe measurements at our pentacene films by the group of S. Lochbrunner, that were already introduced in section 7.4.2, could be modeled with a triplet exciton diffusion constant of $D_T = 13.5 \cdot 10^{-4} \text{ cm}^2/\text{s}$ [101]. Using equation (3.9), the lifetime of the triplet excitons τ_T can be calculated by

$$\tau_T = \frac{\sigma^2}{D_T} \quad (7.4)$$

which results in $\tau_T = 3 \cdot 10^{-5} \text{ s} = 30 \mu\text{s}$. This agrees very well with the value of 10^{-5} s , that Godlewski et. al. have used as fitting parameter for their photoenhancement current measurements in pentacene films [102]. Therefore, we think, that the broadening of the peak is due to triplet exciton diffusion and the fast photoresponse component is due to a triplet exciton assisted hole detrapping mechanism.

In the future, it can be verified if the broadening of the fast photoresponse is due to diffusion by temperature dependent measurements, as due to the Einstein relation (equation (3.7)), the diffusion constant is proportional to the temperature times the mobility. The

fast photoresponse component is expected to be further broadened, if the temperature is increased. However, in pentacene, the mobility is usually temperature dependent as well, therefore it has to be determined for every temperature using transconductance measurements.

In conclusion, the photoresponse consists of two contributions with different timescales. Throughout the whole device, a slow response with a characteristic time scale of about 10 ms was detected. This timescale agrees with a bolometric mechanism. Heat, that is created in the silicon or in the pentacene, is transferred into the transistor channel, where trapped holes are subsequently released. This leads to an increase of the mobile holes leading to an increase of the source-drain current. A much faster response with a characteristic time scale of $5\ \mu\text{s}$ was detected at the contact edges. This time scale agrees with an electronic process. It is triggered by the high electric field at the metal-semiconductor junctions leading to a separation of the excitons and holes. The electrons detrapp holes and increase the amount of mobile holes. Similar to the slow photoresponse, this leads to an increase of the source-drain current. The observed broadening of the signal was explained by the high intersystem crossing rate from singlet excitons into triplet excitons, which have a long lifetime and hence a long diffusion length.

Chapter 8

Conclusion

Within the scope of this thesis, the transport and optoelectronic properties of pentacene TFTs were investigated. To disentangle various processes that influence the electronic and optical behavior of these devices, we measured spatially resolved. Two measurement setups were designed and implemented for these purposes. First, we established an in-situ measurement setup, which allowed for the determination of the transport parameters of pentacene transistors during evaporation with a thickness resolution of 1 Å. Second, a laser scanning microscope in combination with a brightfield microscope was developed. This optical setup enabled us to measure the reflection, the photoluminescence and the photoresponse, which is the light induced change of the transistor current, in dependence on the position of the illumination spot with a spatial resolution in the submicron regime. We prepared unipolar bottom-contact pentacene TFTs and achieved hole mobilities of about $10^{-3} - 10^{-1} \text{ cm}^2 / (V s)$. Using bare silicon dioxide as dielectric, the transistors showed a very high hysteresis behavior, which could be considerably reduced by depositing a polymer buffer layer on top. The hysteresis and changes of the threshold voltage revealed, that hole traps are present in large numbers. Area trap densities of about $10^{11} \text{ cm}^{-2} - 10^{12} \text{ cm}^{-2}$ could be estimated, which compares with free carrier concentrations of 10^{12} cm^{-2} .

Detailed information of the traps was gained by the in-situ measurements. We determined the mobility, the hysteresis and the threshold voltage during pentacene evaporation. The onset of current flow in our transistor was very stable at a nominal pentacene thickness of about 0.7 monolayer. This submonolayer transport can be explained by percolation theory and could be confirmed by AFM micrographs. The mobility evolution during deposition showed strong sample to sample variations, which suggests that this parameter is influenced by extrinsic factors such as imperfect contacts. In contrast, the hysteresis and the evolution of the threshold voltage were much more reproducible, indicating that these parameters are more suited for an investigation of the intrinsic properties of pentacene thin films. Both signals showed saturation at a thickness of about three monolayers, which was interpreted to be the Debye length of the semiconducting pentacene film. Especially the evolution of the hysteresis could not be explained by established models including interface trap states located at the semiconductor-dielectric interface, or by volume trap states within the bulk of the pentacene. Therefore, we propose that trap states are located

on the surface of the pentacene layer, which are grown out of the transistor channel after the deposition of three monolayers. The high trap state density can be explained by the polaron model, as the polarization environment on the surface is altered due to the broken symmetry of the environment, or by growth defects on the surface.

Our lasing scanning microscope setup enabled us to map polarization dependent absorption of single pentacene grains using the reflection signal of linear polarized light. The structure of the pentacene thin film phase implies that a Davydov doublet exists including a second excited singlet state S_1 with a nearly perpendicular transmission dipole moment. This could be demonstrated by a second light source with a wavelength, that matches the transmission into this second excitation.

The Photoluminescence (PL) signal was independent of the applied voltages and increased linearly with the incident laser power. This indicates that it is caused by a monomolecular process. The very low PL efficiency of about 10^{-7} originates from a high intersystem crossing rate from singlet excitons into triplet excitons in pentacene. This was confirmed by pump and probe measurements, that were performed at our samples in a collaboration with S. Lochbrunner. These measurements revealed an ultrafast process of 70 fs , that quenches the fluorescence. The low photoluminescence allowed for the measurement of Raman signals. Various Raman peaks could be allocated to different vibration modes of the pentacene molecule in the crystal by comparing their wave numbers with literature values.

The dependency of the photoresponse (PR) on the applied voltages and on the position of the illuminated spot was studied. The PR signal increased with the gate voltage and vanished when the transistor was operated at the off-state. Photocurrent based on extraction of both, electrons and holes, could be ruled out. The photoresponse consists of two different components. First, a slow contribution with a time scale of about 10 ms was measured throughout the whole channel. This slow response is indicative of a bolometric effect. A model was developed, that explained this photoresponse component by an increase of the free hole density within the transistor channel due to detrapping of holes. Detrapping is triggered by heat due to light absorption in the laser focus and subsequent heat transport into the pentacene layer. Second, a fast contribution with a time scale of less than $5\text{ }\mu\text{s}$ was detected for an illumination adjacent to the contact edges. This fast time scale is typical for electronic processes. Therefore, we propose that this contribution is caused by exciton fission which is enabled by the high electric field existing at the metal-semiconductor interface. Since the gate voltage dependence is similar to the slow photoresponse component, we think that the exciton fission finally also leads to hole detrapping in the transistor channel. The width of the fast photoresponse component is about $2\text{ }\mu\text{m}$ and thus much larger than the illumination spot, that is only $0.5\text{ }\mu\text{m}$ wide. This can be explained by exciton diffusion. The lifetime of the excitons was estimated to be $30\text{ }\mu\text{s}$. Such a long lifetime can only stem from longliving triplet excitons, which can be generated due to the high intersystem crossing rate, which is also responsible for the low photoluminescence yield. Finally, the fast component vanishes at the drain contact, when the TFT is operated at saturation conditions. This was interpreted to be a pinch off phenomenon, as the transistor channel is not accumulated beyond the pinch off point. Therefore, no trapped holes are available

for the detrapping mechanism.

In the future, it could be verified, that the slow photoresponse is a bolometric effect by using alternative substrates or by changing the wavelength of the incident light. Using transparent substrates such as indium tin oxide (ITO) covered glass should reduce absorption. Therefore, the heating should be suppressed, which leads to a smaller slow photoresponse signal. In contrast, the bolometric effect and thus the photoresponse could be enhanced if infrared light, that is highly absorbed in the silicon substrate, is taken for illumination. Finally, pulsed lasers could be used to resolve the time scale of the fast photoresponse component. Temperature dependent measurements could contribute to a deeper understanding of the triplet diffusion and recombination processes during charge transport.

The in-situ measurement setup could be used to investigate transistors which contain different semiconducting layers. Within his diploma thesis, S. Noever succeeded in fabricating ambipolar transistors by evaporating a pentacene layer as p-conductor on top of a C60 layer as n-conductor [103]. The development of the transport parameters during evaporation can provide interesting information on the properties of the interface of organic p-n junctions. It might be possible to determine the extension of the depletion region of these junctions, which allow to determine the charge carrier densities of the organic compounds. Blend systems of p-conducting and n-conducting organic semiconductors could be realized by simultaneous co-evaporation. Using different evaporation rates allows to adjust the ratio between the organic semiconductors. The influence of this ratio on the transport parameters such as the mobility and the threshold voltage can be investigated. Additional x-ray and AFM studies could help to understand the correlations between structural and electrical properties of these blend systems.

Blend systems in general could be investigated by the laser scanning microscope setup, too. In contrast to vertical structures like diodes, the lateral structure of the TFT allows for a spatially resolved investigation of heterojunctions. The geometry of the transistor is particularly advantageous since its charge carrier concentrations can be adjusted by the gate voltage. This field effect doping avoids structural changes as it usually happens by conventional doping using impurity atoms and thus avoids undesired influences on the intrinsic properties of the organic compounds.

Finally, pentacene is of special interest for solar cells, since the high intersystem crossing rate provides a large amount of triplet excitons. The long diffusion length of the triplet excitons enables a high yield of charge separation at organic interfaces.

Acknowledgment

The Deutsche Forschungsgemeinschaft DFG (Ni 632/2-1) primarily financed this PhD-thesis. The work was also supported by Nanosystems Initiative Munich (NIM) and the Center for Nanoscience (CeNS).

The sample preparation and characterization were partly performed using the facilities in the cleanroom of LS Kotthaus of the Ludwig-Maximilians-Universität.

The pump and probe measurements of our pentacene thin films were conducted by Henning Marcianak in the group of Stefan Lochbrunner at LS Zinth of the Ludwig-Maximilians-Universität.

The drift-diffusion simulations were performed by Christoph Erlen in the group of Paolo Lugli at the Institute for Nanoelectronics of the TU München.

Bibliography

- [1] D. D. Eley. Phthalocyanines as semiconductors. *Nature*, 162(4125):819, 1948.
- [2] H. Akamatu and H. Inokuchi. On the electrical conductivity of violanthrone, iso-violanthrone, and pyranthrone. *J. Chem. Phys.*, 18(6):810, 1950.
- [3] D. D. Eley, G. D. Parfitt, M. J. Perry, and D. H. Taysum. The semiconductivity of organic substances .1. *Transactions of the Faraday Society*, 49(1):79, 1953.
- [4] P. Mark and W. Helfrich. Space-charge-limited currents in organic crystals. *J. Appl. Phys.*, 33(1):205, 1962.
- [5] H. Kallmann and M. Pope. Bulk conductivity in organic crystals. *Nature*, 186(4718):31, 1960.
- [6] W. Helfrich and P. Mark. Eine bestimmung der effektiven zustandsdichte des bandes fur uberschussige defektelektronen in anthrazen. *Zeitschrift Fur Physik*, 171(3):527, 1963.
- [7] M. Pope, P. Magnante, and H. P. Kallmann. Electroluminescence in organic crystals. *J. Chem. Phys.*, 38(8):2042, 1963.
- [8] W. Helfrich and Schneide.Wg. Recombination radiation in anthracene crystals. *Phys. Rev. Lett.*, 14(7):229, 1965.
- [9] C. W. Tang. 2-layer organic photovoltaic cell. *Applied Physics Letters*, 48(2):183, 1986.
- [10] C. W. Tang and S. A. Vanslyke. Organic electroluminescent diodes. *Applied Physics Letters*, 51(12):913, 1987.
- [11] H. Koezuka, A. Tsumura, and T. Ando. Field-effect transistor with polythiophene thin-film. *Synth. Met.*, 18(1-3):699, 1987.
- [12] H. Klauk. Organic thin-film transistors. *Chem. Soc. Rev.*, 39(7):2643, 2010.
- [13] S. M. Sze. *Physics of Semiconductor*. John Wiley Sons Inc., New York, 1981.

- [14] G. Hadziioannou and P. F. van Hutten. *Semiconducting Polymers*. Wiley-VCH Verlag GmbH, Weinheim, 2000.
- [15] D. R. Lide. *CRC Handbook of Chemistry and Physics, 89th edition*. CRC Press, Boca Raton, 2008.
- [16] A. R. Brown, C. P. Jarrett, D. M. deLeeuw, and M. Matters. Field-effect transistors made from solution-processed organic semiconductors. *Synth. Met.*, 88(1):37, 1997.
- [17] G. Horowitz. Organic field-effect transistors. *Adv. Mater.*, 10(5):365, 1998.
- [18] C. E. Swenberg M. Pope. *Electronic Processes in Organic Crystals and Polymers, 2nd Edition*. Oxford University Press, Oxford, 1999.
- [19] H. C. Wolf M. Schwoerer. *Organische Molekulare Festkörper*. Wiley-VCH Verlag GmbH Co. KGaA, Weinheim, 2005.
- [20] V. Coropceanu, J. Cornil, D. A. da Silva, Y. Olivier, R. Silbey, and J. L. Bredas. Charge transport in organic semiconductors. *Chem. Rev.*, 107(5):926, 2007.
- [21] K. Hannewald, V. M. Stojanovic, J. M. T. Schellekens, P. A. Bobbert, G. Kresse, and J. Hafner. Theory of polaron bandwidth narrowing in organic molecular crystals. *Phys. Rev. B*, 69(7):075211, 2004.
- [22] W. Warta, R. Stehle, and N. Karl. Ultrapure, high mobility organic photoconductors. *Appl. Phys. A-Mater. Sci. Process.*, 36(3):163, 1985.
- [23] C. D. Dimitrakopoulos and P. R. L. Malenfant. Organic thin film transistors for large area electronics. *Adv. Mater.*, 14(2):99, 2002.
- [24] Y. M. Sun, Y. Q. Liu, and D. B. Zhu. Advances in organic field-effect transistors. *J. Mater. Chem.*, 15(1):53, 2005.
- [25] Y. Y. Lin, D. J. , S. F. Nelson, and T. N. Jackson. Stacked pentacene layer organic thin-film transistors with improved characteristics. *IEEE Electron Device Lett.*, 18(12):606, 1997.
- [26] D. V. Lang, X. Chi, T. Siegrist, A. M. Sergent, and A. P. Ramirez. Amorphouslike density of gap states in single-crystal pentacene. *Phys. Rev. Lett.*, 93(8):086802, 2004.
- [27] M. Grobosch, R. Schuster, T. Pichler, M. Knupfer, and H. Berger. Analysis of the anisotropy of excitons in pentacene single crystals using reflectivity measurements and electron energy-loss spectroscopy. *Phys. Rev. B*, 74(15):155202, 2006.
- [28] V. Podzorov, V. M. Pudalov, and M. E. Gershenson. Field-effect transistors on rubrene single crystals with parylene gate insulator. *Applied Physics Letters*, 82(11):1739, 2003.

- [29] B. Stadlober, U. Haas, H. Maresch, and A. Haase. Growth model of pentacene on inorganic and organic dielectrics based on scaling and rate-equation theory. *Phys. Rev. B*, 74(16):165302, 2006.
- [30] J. A. Venables, G. D. T. Spiller, and M. Hanbucken. Nucleation and growth of thin-films. *Rep. Prog. Phys.*, 47(4):399, 1984.
- [31] R. Ruiz, B. Nickel, N. Koch, L. C. Feldman, R. F. Haglund, A. Kahn, and G. Scoles. Pentacene ultrathin film formation on reduced and oxidized si surfaces. *Phys. Rev. B*, 67(12):125406, 2003.
- [32] S. Schiefer, M. Huth, A. Dobrinevski, and B. Nickel. Determination of the crystal structure of substrate-induced pentacene polymorphs in fiber structured thin films. *J. Am. Chem. Soc.*, 129(34):10316, 2007.
- [33] D. Kafer, L. Ruppel, and G. Witte. Growth of pentacene on clean and modified gold surfaces. *Phys. Rev. B*, 75(8):085309, 2007.
- [34] G. Beernink, T. Strunskus, G. Witte, and C. Woll. Importance of dewetting in organic molecular-beam deposition: Pentacene on gold. *Applied Physics Letters*, 85(3):398, 2004.
- [35] J. E. Northrup, M. L. Tiago, and S. G. Louie. Surface energetics and growth of pentacene. *Phys. Rev. B*, 66(12):121404, 2002.
- [36] D. Knipp, R. A. Street, A. Volkell, and J. Ho. Pentacene thin film transistors on inorganic dielectrics: Morphology, structural properties, and electronic transport. *J. Appl. Phys.*, 93(1):347, 2003.
- [37] M. Shtein, J. Mapel, J. B. Benziger, and S. R. Forrest. Effects of film morphology and gate dielectric surface preparation on the electrical characteristics of organic-vapor-phase-deposited pentacene thin-film transistors. *Applied Physics Letters*, 81(2):268, 2002.
- [38] H. Ichikawa, A. Koma, K. Saiki, and T. Shimada. Interaction between surface migrating pentacene molecules and chemically modified surfaces of silicon oxides studied by pulsed molecular beam scattering. *Surf. Sci.*, 600(17):L236, 2006.
- [39] S. C. Lim, S. H. Kim, J. H. Lee, M. K. Kim, D. J. Kim, and T. Zyung. Surface-treatment effects on organic thin-film transistors. *Synth. Met.*, 148(1):75, 2005.
- [40] D. J. Gundlach, L. Zhou, J. A. Nichols, T. N. Jackson, P. V. Necliudov, and M. S. Shur. An experimental study of contact effects in organic thin film transistors. *J. Appl. Phys.*, 100(2):024509, 2006.
- [41] P. V. Necliudov, M. S. Shur, D. J. Gundlach, and T. N. Jackson. Contact resistance extraction in pentacene thin film transistors. *Solid-State Electronics*, 47(2):259, 2003.

- [42] B. Nickel, M. Fiebig, S. Schiefer, M. Goellner, M. Huth, C. Erlen, and P. Lugli. Pentacene devices: Molecular structure, charge transport and photo response. *Phys. Status Solidi A-Appl. Mat.*, 205(3):526, 2008.
- [43] G. Horowitz, M. E. Hajlaoui, and R. Hajlaoui. Temperature and gate voltage dependence of hole mobility in polycrystalline oligothiophene thin film transistors. *J. Appl. Phys.*, 87(9):4456, 2000.
- [44] B. Nickel, R. Barabash, R. Ruiz, N. Koch, A. Kahn, L. C. Feldman, R. F. Haglund, and G. Scoles. Dislocation arrangements in pentacene thin films. *Phys. Rev. B*, 70(12):125401, 2004.
- [45] G. Gu and M. G. Kane. Moisture induced electron traps and hysteresis in pentacene-based organic thin-film transistors. *Applied Physics Letters*, 92(5):053305, 2008.
- [46] P. G. Schroeder, C. B. France, J. B. Park, and B. A. Parkinson. Energy level alignment and two-dimensional structure of pentacene on au(111) surfaces. *J. Appl. Phys.*, 91(5):3010, 2002.
- [47] D. Kafer, G. Witte, P. Cyganik, A. Terfort, and C. Woll. A comprehensive study of self-assembled monolayers of anthracenethiol on gold: Solvent effects, structure, and stability. *J. Am. Chem. Soc.*, 128(5):1723, 2006.
- [48] H. Klauk, G. Schmid, W. Radlik, W. Weber, L. S. Zhou, C. D. Sheraw, J. A. Nichols, and T. N. Jackson. Contact resistance in organic thin film transistors. *Solid-State Electronics*, 47(2):297, 2003.
- [49] T. Maeda, H. Kato, and H. Kawakami. Organic field-effect transistors with reduced contact resistance. *Applied Physics Letters*, 89(12):123508, 2006.
- [50] J. Takeya, C. Goldmann, S. Haas, K. P. Pernstich, B. Ketterer, and B. Batlogg. Field-induced charge transport at the surface of pentacene single crystals: A method to study charge dynamics of two-dimensional electron systems in organic crystals. *J. Appl. Phys.*, 94(9):5800, 2003.
- [51] I. Yagi, K. Tsukagoshi, and Y. Aoyagi. Direct observation of contact and channel resistance in pentacene four-terminal thin-film transistor patterned by laser ablation method. *Applied Physics Letters*, 84(5):813, 2004.
- [52] K. P. Puntambekar, P. V. Pesavento, and C. D. Frisbie. Surface potential profiling and contact resistance measurements on operating pentacene thin-film transistors by kelvin probe force microscopy. *Applied Physics Letters*, 83(26):5539, 2003.
- [53] A. Petrovic, E. Pavlica, G. Bratina, A. Carpentiero, and M. Tormen. Contact resistance in organic thin film transistors. *Synth. Met.*, 159(12):1210, 2009.

- [54] L. Burgi, H. Sirringhaus, and R. H. Friend. Noncontact potentiometry of polymer field-effect transistors. *Applied Physics Letters*, 80(16):2913, 2002.
- [55] C. Erlen, P. Lugli, M. Fiebig, S. Schiefer, and B. Nickel. Transient tcad simulation of three-stage organic ring oscillator. *J. Comput. Electron.*, 5:345, 2006.
- [56] M. A. Alam, A. Dodabalapur, and M. R. Pinto. A two-dimensional simulation of organic transistors. *IEEE Trans. Electron Devices*, 44(8):1332, 1997.
- [57] A. Bolognesi, M. Berliocchi, M. Manenti, A. Di Carlo, P. Lugli, K. Lmimouni, and C. Dufour. Effects of grain boundaries, field-dependent mobility, and interface trap states on the electrical characteristics of pentacene tft. *IEEE Trans. Electron Devices*, 51(12):1997, 2004.
- [58] P. F. Baude, D. A. Ender, M. A. Haase, T. W. Kelley, D. V. Muyres, and S. D. Theiss. Pentacene-based radio-frequency identification circuitry. *Applied Physics Letters*, 82(22):3964, 2003.
- [59] Daniel Beckmeier. In-situ study of electronical properties of pentacene transistors during growth. Diploma thesis, Ludwig-Maximilians-Universität München, Germany, 2008.
- [60] M. Fiebig, D. Beckmeier, and B. Nickel. Thickness-dependent in situ studies of trap states in pentacene thin film transistors. *Applied Physics Letters*, 96(8):083304, 2010.
- [61] Y. S. Lee, J. H. Park, and J. S. Choi. Electrical characteristics of pentacene-based schottky diodes. *Opt. Mater.*, 21(1-3):433, 2003.
- [62] A. Dodabalapur, L. Torsi, and H. E. Katz. Organic transistors - 2-dimensional transport and improved electrical characteristics. *Science*, 268(5208):270, 1995.
- [63] F. Dinelli, M. Murgia, P. Levy, M. Cavallini, F. Biscarini, and D. M. de Leeuw. Spatially correlated charge transport in organic thin film transistors. *Phys. Rev. Lett.*, 92(11):116802, 2004.
- [64] R. Schroeder, L. A. Majewski, and M. Grell. A study of the threshold voltage in pentacene organic field-effect transistors. *Applied Physics Letters*, 83(15):3201, 2003.
- [65] Y. W. Wang and H. L. Cheng. Thickness-dependent threshold voltage in polycrystalline pentacene-based thin-film transistors. *Solid-State Electronics*, 53(10):1107, 2009.
- [66] R. Ruiz, A. Papadimitratos, A. C. Mayer, and G. G. Malliaras. Thickness dependence of mobility in pentacene thin-film transistors. *Adv. Mater.*, 17(14):1795, 2005.
- [67] M. Kiguchi, M. Nakayama, K. Fujiwara, K. Ueno, T. Shimada, and K. Saiki. Accumulation and depletion layer thicknesses in organic field effect transistors. *Jpn. J. Appl. Phys. Part 2 - Lett.*, 42(12A):L1408, 2003.

- [68] T. Muck, V. Wagner, U. Bass, M. Leufgen, J. Geurts, and L. W. Molenkamp. In situ electrical characterization of dh4t field-effect transistors. *Synth. Met.*, 146(3):317, 2004.
- [69] B. N. Park, S. Seo, and P. G. Evans. Channel formation in single-monolayer pentacene thin film transistors. *J. Phys. D-Appl. Phys.*, 40(11):3506, 2007.
- [70] J. Quintanilla, S. Torquato, and R. M. Ziff. Efficient measurement of the percolation threshold for fully penetrable discs. *J. Phys. A-Math. Gen.*, 33(42):L399, 2000.
- [71] S. Sreenivasan, D. R. Baker, G. Paul, and H. E. Stanley. The approximate invariance of the average number of connections for the continuum percolation of squares at criticality. *Physica A*, 320:34, 2003.
- [72] K. P. Pernstich, S. Haas, D. Oberhoff, C. Goldmann, D. J. Gundlach, B. Batlogg, A. N. Rashid, and G. Schitter. Threshold voltage shift in organic field effect transistors by dipole monolayers on the gate insulator. *J. Appl. Phys.*, 96(11):6431, 2004.
- [73] G. Gu, M. G. Kane, J. E. Doty, and A. H. Firester. Electron traps and hysteresis in pentacene-based organic thin-film transistors. *Appl. Phys. Lett.*, 87(24):243512, 2005.
- [74] C. Ucurum, H. Goebel, F. A. Yildirim, W. Bauhofer, and W. Krautschneider. Hole trap related hysteresis in pentacene field-effect transistors. *J. Appl. Phys.*, 104(8):084501, 2008.
- [75] U. Zschieschang, R. T. Weitz, K. Kern, and H. Klauk. Bias stress effect in low-voltage organic thin-film transistors. *Appl. Phys. A-Mater. Sci. Process.*, 95(1):139, 2009.
- [76] J. H. Kang, D. da Silva, J. L. Bredas, and X. Y. Zhu. Shallow trap states in pentacene thin films from molecular sliding. *Applied Physics Letters*, 86(15):152115, 2005.
- [77] M. Nakamura, H. Ohguri, N. Goto, H. Tomii, M. S. Xu, T. Miyamoto, R. Matsubara, N. Ohashi, M. Sakai, and K. Kudo. Extrinsic limiting factors of carrier transport in organic field-effect transistors. *Appl. Phys. A-Mater. Sci. Process.*, 95(1):73, 2009.
- [78] Martin Göllner. Optical and electronic Properties of Pentacene Thin Film Transistors. Diploma thesis, Ludwig-Maximilians-Universität München, Germany, 2007.
- [79] Christian Westermeier. Orts- und zeitaufgelöste Photostrommessungen an organischen Dünnschichttransistoren. Diploma thesis, Ludwig-Maximilians-Universität München, Germany, 2010.
- [80] M. Fiebig, C. Erlen, M. Göllner, P. Lugli, and B. Nickel. Spatially resolved photoreponse measurements on pentacene thin-film transistors. *Appl. Phys. A, Mater. Sci. Process.*, 95(1):113, 2009.

- [81] C. Meyer, O. Sqalli, H. Lorenz, and K. Karrai. Slip-stick step-scanner for scanning probe microscopy. *Rev. Sci. Instrum.*, 76(6):063706, 2005.
- [82] L. Sebastian, G. Weiser, and H. Bassler. Charge-transfer transitions in solid tetracene and pentacene studied by electro-absorption. *Chem. Phys.*, 61(1-2):125, 1981.
- [83] M. Dressel, B. Gompf, D. Faltermeier, A. K. Tripathi, J. Pflaum, and M. Schubert. Kramers-kronig-consistent optical functions of anisotropic crystals: generalized spectroscopic ellipsometry on pentacene. *Opt. Express*, 16(24):19770, 2008.
- [84] D. Faltermeier, B. Gompf, M. Dressel, A. K. Tripathi, and J. Pflaum. Optical properties of pentacene thin films and single crystals. *Phys. Rev. B*, 74(12):125416, 2006.
- [85] R. H. Friend, R. W. Gymer, A. B. Holmes, J. H. Burroughes, R. N. Marks, C. Taliani, D. D. C. Bradley, D. A. Dos Santos, J. L. Bredas, M. Logdlund, and W. R. Salaneck. Electroluminescence in conjugated polymers. *Nature*, 397(6715):121, 1999.
- [86] J. C. Carter, I. Grizzi, S. K. Heeks, D. J. Lacey, S. G. Latham, P. G. May, O. R. delosPanos, K. Pichler, C. R. Towns, and H. F. Wittmann. Operating stability of light-emitting polymer diodes based on poly(p-phenylene vinylene). *Applied Physics Letters*, 71(1):34, 1997.
- [87] S. P. Park, S. S. Kim, J. H. Kim, C. N. Whang, and S. Im. Optical and luminescence characteristics of thermally evaporated pentacene films on si. *Applied Physics Letters*, 80(16):2872, 2002.
- [88] M. Schidleja, C. Melzer, and H. von Seggern. Electroluminescence from a pentacene based ambipolar organic field-effect transistor. *Applied Physics Letters*, 94(12):123307, 2009.
- [89] R. He, N. G. Tassi, G. B. Blanchet, and A. Pinczuk. Fundamental optical recombination in pentacene clusters and ultrathin films. *Applied Physics Letters*, 87(10):103107, 2005.
- [90] T. Aoki-Matsumoto, K. Furuta, T. Yamada, H. Moriya, K. Mizuno, and A. H. Matsui. Excitonic photoluminescence in pentacene single crystal. *Int. J. Mod. Phys. B*, 15(28-30):3753, 2001.
- [91] R. He, X. Chi, A. Pinczuk, D. V. Lang, and A. P. Ramirez. Extrinsic optical recombination in pentacene single crystals: Evidence of gap states. *Applied Physics Letters*, 87(21):211117, 2005.
- [92] H. Marciniak, M. Fiebig, M. Huth, S. Schiefer, B. Nickel, F. Selmaier, and S. Lochbrunner. Ultrafast exciton relaxation in microcrystalline pentacene films. *Phys. Rev. Lett.*, 99(17):176402, 2007.

- [93] T. Wilhelm, J. Piel, and E. Riedle. Sub-20-fs pulses tunable across the visible from a blue-pumped single-pass noncollinear parametric converter. *Opt. Lett.*, 22(19):1494, 1997.
- [94] C. Jundt, G. Klein, B. Sipp, J. Lemoigne, M. Joucla, and A. A. Villaeys. Exciton dynamics in pentacene thin-films studied by pump-probe spectroscopy. *Chemical Physics Letters*, 241(1-2):84, 1995.
- [95] T. S. Kuhlman, J. Kongsted, K. V. Mikkelsen, K. B. Moller, and T. I. Solling. Interpretation of the ultrafast photoinduced processes in pentacene thin films. *J. Am. Chem. Soc.*, 132(10):3431.
- [96] L. Colangeli, V. Mennella, G. A. Baratta, E. Bussoletti, and G. Strazzulla. Raman and infrared-spectra of polycyclic aromatic hydrocarbon molecules of possible astrophysical interest. *Astrophys. J.*, 396(1):369, 1992.
- [97] R. He, I. Dujovne, L. W. Chen, Q. Miao, C. F. Hirjibehedin, A. Pinczuk, C. Nuckolls, C. Kloc, and A. Ron. Resonant raman scattering in nanoscale pentacene films. *Applied Physics Letters*, 84(6):987, 2004.
- [98] T. B. Singh, T. Meghdadi, S. Gunes, N. Marjanovic, G. Horowitz, P. Lang, S. Bauer, and N. S. Sariciftci. High-performance ambipolar pentacene organic field-effect transistors on poly(vinyl alcohol) organic gate dielectric. *Adv. Mater.*, 17(19):2315, 2005.
- [99] B. Zebli, H. A. Vieyra, I. Carmeli, A. Hartschuh, J. P. Kotthaus, and A. W. Holleitner. Optoelectronic sensitization of carbon nanotubes by cdte nanocrystals. *Phys. Rev. B*, 79(20):205402, 2009.
- [100] A. W. Tsen, F. Cicoira, G. G. Malliaras, and J. Park. Photoelectrical imaging and characterization of point contacts in pentacene thin-film transistors. *Applied Physics Letters*, 97(2):023308, 2010.
- [101] H. Marciniak, I. Pugliesi, B. Nickel, and S. Lochbrunner. Ultrafast singlet and triplet dynamics in microcrystalline pentacene films. *Phys. Rev. B*, 79(23):235318, 2009.
- [102] J. Godlewski, G. Jarosz, and R. Signerski. Photoenhanced current in thin organic layers. *Appl. Surf. Sci.*, 175:344, 2001.
- [103] Simon Noever. In situ characterization of ambipolar organic field effect transistors. Diploma thesis, Ludwig-Maximilians-Universität München, Germany, 2010.

List of Publications

- *Transient TCAD simulations of three-stage organic ring oscillator*
C. Erlen, P. Lugli, M. Fiebig, S. Schiefer, and B. Nickel
J. Comput. Electron. **5**, 345 (2006)
- *Ultrafast exciton relaxation in microcrystalline pentacene films*
H. Marciniak, M. Fiebig, M. Huth, S. Schiefer, B. Nickel, F. Selmeier, and S. Lochbrunner
Phys. Rev. Lett. **99**, no. 17, 176402 (2007)
- *Pentacene devices: Molecular structure, charge transport and photo response*
B. Nickel, M. Fiebig, S. Schiefer, M. Göllner, M. Huth, C. Erlen, and P. Lugli
Phys. Status Solidi A-Appl. Mat. **205**, no. 3, 526 (2008)
- *Spatially resolved photoresponse measurements on pentacene thin-film transistors*
M. Fiebig, C. Erlen, M. Göllner, P. Lugli, and B. Nickel
Appl. Phys. A, Mater. Sci. Process. **95**, no. 1, 113 (2009)
- *Thickness-dependent in situ studies of trap states in pentacene thin film transistors*
M. Fiebig, D. Beckmeier, and B. Nickel
Applied Physics Letters **96**, no. 8, 083304 (2010)

Danksagung

An dieser Stelle möchte ich der erfreulichen Aufgabe nachkommen, allen zu danken, die zu dieser Doktorarbeit beigetragen haben und mich während dieser Zeit unterstützten. Ich bedanke mich besonders bei

Jörg Kotthaus und Joachim Rädler für die Möglichkeit, an ihren Lehrstühlen in ausgesprochen angenehmer Atmosphäre zu arbeiten.

Bert Nickel für eine sehr gute und geduldige Betreuung. Deine Gelassenheit und Dein Optimismus, der sogar mich anzustecken drohte, hat sehr geholfen. Unser gemeinsames Erarbeiten eines profunderen Verständnisses von Transporteigenschaften in der organischen Welt hat mir stets Freude bereitet.

Martin Göllner, Daniel Beckmeier und Christian Westermeier für die sehr gute Zusammenarbeit. Euer Engagement hat sehr zum Gelingen dieser Arbeit beigetragen. Es freut mich, dass Euch alle eine eigene Promotion nicht schreckte.

der gesamten Arbeitsgruppe Nickel für die freundliche und konstruktive Arbeitsatmosphäre. Speziell Martin Huth, Martin Göllner und Simon Noever bin ich sehr für die Wartung der Aufdampfanlagen verbunden.

Alexander Paul, Stefan Schöffberger, Phillip Altpeter, Reinhold Rath, Stephan Manus, Bert Lorenz, Susi Kempfer und Gerlinde Schwake für ihre ausgezeichnete Arbeit, die für hervorragende Arbeitsbedingungen an den beiden Lehrstühlen Kotthaus und Rädler sorgen.

Martina Jüttner und Margarete Meixner für ihre organisatorische Unterstützung. Auch der stetig fließende Kaffeefluß sei an dieser Stelle erwähnt.

meinen Bürokollegen, allen Mensagängern und Kaffeetrinkern für die zerstreuten, nicht-physikalischen Diskussionen.

meinen Eltern, die mir ein Studium ermöglichten und mich in meinen Entscheidungen stets unterstützten.

Lebenslauf

Matthias Fiebig

geboren am 29.01.1978 in München

Schulbildung

9/1984 - 7/1988 Besuch der Grundschule in Unterföhring

9/1988 - 7/1989 Besuch der Hauptschule in Unterföhring

9/1989 - 7/1998 Besuch des Wilhelm-Hausenstein-Gymnasiums in München

Wehrdienst

7/1998 - 4/1999 Drohnenbatterie 200, München

Hochschulbildung

10/1999 - 11/2004 Physik-Studium an der Ludwig-Maximilians Universität München

12/2004 - 11/2005 Diplomarbeit am Lehrstuhl für Experimentalphysik
der LMU München bei Prof. Dr. J. Kotthaus

2/2006 - 5/2010 Promotion am Lehrstuhl für Experimentalphysik der LMU München
bei PD Dr. B. Nickel